UNIVERSITA' DEGLI STUDI DELL'AQUILA

Dipartimento di Scienze fisiche e Chimiche

Dottorato in Scienze Fisiche e Chimiche

XXXVI ciclo

Experimental and computational study of soft matter: structural and reactivity characterization of ionic liquids and deep eutectic solvents

SSD: CHIM/02

Dottorando:

SIMONE DI MUZIO

Relatori
prof. Fabio Ramondo
dr. Annalisa Paolone

Coordinatore del corso e tutor
prof. Massimiliano Aschi

A.A. 2022/2023

Perché dovremmo studiare questo problema se
non ci divertiamo a risolverlo?
prof. Nicola Cabibbo

Abstract

The search of novel alternative to traditional solvents has interested the scientific community for many years. During the last years many systems were proposed: among these noteworthy are Ionic Liquids (ILs) and Deep Eutectic Solvents (DES). The idea behind these novel liquids is to enhance and improve the eco-compatibility of traditional solvents by using these materials as viable, more environmentally friendly substitutes for conventional solvents or molecular liquids. The peculiar physical and chemical properties exhibited by these solvents (as low melting point, low volatility, large thermal and electrochemical window stability) are originated by the extraordinary coordination occurring in the liquid phase: hydrogen bonding, for instances, plays a crucial role on the stabilization of liquid phase in both ILs and DESs. In this thesis, with the aim of understanding the innovative properties exhibited by DESs and ILs, we investigated by a combined experimental and computational approach, the structure of many DESs. We performed thermal analysis (DSC and TGA) and vibrational spectroscopy (FIR, MIR and, when necessary, Raman spectroscopies). The bulk phase, for some systems, was also studied by Wide-angle X-Ray scattering (WAXS). To better understand the interactions and conduct an accurate interpretation of the experimental data, all systems were modelled by computational approaches, using DFT and classical MD simulations. We also investigated on the interactions of ILs onto graphene surface. The chemiadsorption was deeply investigated by computational approach: DFT calculation and MD simulation provided a good description of the interaction between cation and anion and between ILs and N-doped graphene surface. The studied ionic liquids presented an high capability to reacts with CO_2, making them a promising candidate as a CO_2 scrubber. With the aim of characterize the thermodynamic of the chemiadsorption reaction we investigated by DFT on the reaction mechanisms, characterizing each critical point, both for bulk and adsorbed ionic liquids.

Contents

Chapter 1

Introdution

1.1 Soft matter

Soft matter is a useful definition used for materials that are neither simple liquids nor the crystalline solids investigated in other branches of solid state physics. Colloids, surfactants, liquid crystals, certain biomaterials, polymers, and ionic liquid-based materials are examples of soft materials[1, 2]. These materials have, in general, a weaker ordering compared to hard materials. In soft materials, the absence of three-dimensional atomic long-range order found in crystalline solids leads to a lower level of ordering. Nonetheless, soft materials consistently exhibit a degree of local organization. The peculiar short range structural order between components is primarily caused by the intermolecular interactions. The forces between the components can be rationalized as a balance of attractive and repulsive interactions, essentially according to the Lennard-Jones potential[3]. A highly practical model, which encapsulates a significant portion of liquid physics, asserts that the repulsive potential becomes effectively infinite once the molecules overlap. However, it also accounts for a long-range attraction at greater separations This idealization is known as a hard-sphere potential with long-ranged interactions. In soft matter research, a critical focus lies on understanding the role of attractive forces in governing the organization of constituent elements. These interactions significantly influence the overall structural properties of the mate-

rials. The work done in this thesis centers on a comprehensive analysis of deep eutectic solvents (DESs) and ionic liquids (ILs), aiming to characterize their structural properties and chemical reactivity. The objective is to elucidate the molecular processes leading to the formation of these liquid phases. From a chemical perspective, interactions in both DESs and ILs are characterized as secondary, involving non-covalent organization of molecules. These encompass hydrogen bonding, van der Waals forces, ionic interactions, and hydrophobic repulsions[4, 5, 6, 7, 8, 9, 10]. Notwithstanding the structural differences between ionic liquids and deep eutectic solvents, both materials share many chemical-physical properties. The primary objective of this thesis is to conduct a thorough fundamental investigation into the mechanisms governing the formation of these classes of alternative solvents. The idea is to create a link between their structural characteristics and their chemical-physical properties, with the ultimate goal of tuning them: this is critical for practical and experimental application of these liquids. The underlying concept of both system classes is to create a valid alternative to the traditional solvents, improving their solvent capabilities and enhancing their eco-friendliness. Both DES and IL exhibit numerous similarities in terms of physicochemical properties, such as low volatility, low melting point[4], and good electrical conductivity[11, 12, 13]. Before presenting the results of the characterization of the structure and reactivity of the studied systems, a brief overview of the main characteristics of ionic liquids and deep eutectic solvents will be provided in the following paragraphs.

1.1.1 Ionic Liquids (ILs)

Ionic liquids (ILs) constitute a class of solvents entirely composed of ionic compounds that exist in a liquid state at or near room temperature: to be defined as an ionic liquid, the salt must melt below 100°C[9]. ILs are typically classified beased on their chemical structure and categorized into protic ionic liquids (PILs) and aprotic ionic liquids (AILs). In PILs, proton transfer is responsible for the formation of the ionic liquids. However, it was demonstrated that for some ILs, the proton transfer process is not complete and quantitative. In 2007, Kanzaki and coworkers [14] measured by experimentally approaches the autoprotolysis constant of ethylammonium nitrate

(EAN). The experimental measurement showed that EAN possesses a small atoprotolysis constant, sign that the proton transfer process is not complete. The ionic interactions, that involve the electrostatic attraction between oppositely charged ions inside a crystal lattice or salt does involve the largest possible number of ionic pairs. In this way, the spatial organization of ionic components is more disordered than that observed in crystalline ionic solids. Traditional salts exhibit a well-defined spatial organization and a strong stabilization is provided by the lattice energy, which depends on the density of charge of each ionic species. Thus we need tosupply energy greater than the lattice one to melt the ionic compound. Notwithstanding ILs consist of ions, their melting points is lower than traditional ionic salts as result of a lower energy interaction between ionic components. ILs consist in fact of large and asymmetric organic cations and anions. The electrostatic potential of the ionic species is noticeably reduced for delocalization of electric charge on the large ions.[15]. The asymmetry contributes further to decrease the lattice energy and, consequently, decrease melting point. Notwithstanding their reduced lattice energy, a large number of secondary interactions, in addition to ionic interactions, are active in such systems. Among them, hydrogen bonding is found when the mixed components are hydrogen bond acceptors and donors. The presence of hydrogen bonding is responsible of important chemical and physical properties, including low volatility, thermal stability, good electrical and thermal conductivity, wide electrochemical windows, as well as catalytic and solvent capabilities[16, 17, 9]. Due to low environmental impact, ionic liquids find application in numerous eco-friendly application, ranging from electrochemical contexts, where they serve as alternative electrolytes [18], to catalytic applications. Of particular interest is their ability, as highlighted in recent years, to act as adsorbent systems for CO_2, one of the primary greenhouse gases in the atmosphere[19, 20]. The distinctive characteristics these systems manifest when engaging with carbonaceous materials, including graphene and its derivatives, are exceptionally captivating. A wide number of ILs was combined with carbon materials, as nanotubes[21, 22], fullerenes[23] and graphene[24] to develop electrochemical devices as batteries, solar cells and supercapacitors[25]. We have thus undertaken an investigation by computational methods on the capacity of an amino acid-based

ionic liquid to capture CO_2 by chemisorption analysing the reaction and its mechanism both in bulk and when liquid is adsorbed onto graphene surface.

1.1.2 Deep Eutectic Solvents

In the last years the attention has increasingly shifted towards the development of novel classes of solvents as alternatives to traditional ionic liquids. Ionic liquids, as previously mentioned, have remarkable physicochemical characteristics that make them attractive candidates for a wide range of scientific and technological applications, but their synthesis is a quite difficult process. Furthermore, their purification and the elimination of water, often obtained as byproduct of their synthetic reactions, could be not straightforward. For these reason the so-called deep eutectic solvents (DESs) are good candidates to address the problems aforementioned. The term deep eutectic solvents refers to a novel class of solvents made up of binary mixtures composed by non-toxic or with low degree of toxicity chemicals with low environmental effect. In some recent publications[26] the toxicity and green behaviour of DESs were evaluated by toxicological study. The study revealed that some DESs (Deep Eutectic Solvents) exhibited a completely different toxicity compared to the starting materials. In fact, some of these systems proved to be ecotoxic, even though their precursors showed no level of toxicity. The toxicity of each systems, should, therefore, evaluated on a case-by-case basis. The formation of stable liquid phase is driven by the formation of secondary interactions between the components, particularly through hydrogen bonding[5, 6, 7, 8]. In comparison to ILs, the synthesis is very simple because no chemical reactions are required. In fact, the DESs are in general prepared by mixing the precursors in the proper molar ratio, paying attention to atmospheric water contamination and, if feasible, operating under anhydrous conditions or in a protected environment. Deep eutectic solvents can be classified based on their structure. In the literature the generic formula Cat^+Y^-zY is reported to provide a general formulation of these systems. In the formula Cat^+ is the cation, Y^- the anion and Y the hydrogen bond donor. Traditionally DESs are classifiable as reported[7]:

- Type I: metal halides and quaternary ammonium salts

- Type II: metal halides hydrates and quaternary ammonium salts
- Type III: quaternary ammonium salts and hydrogen bond donors
- Type IV: metal halides hydrates and hydrogen bond donors

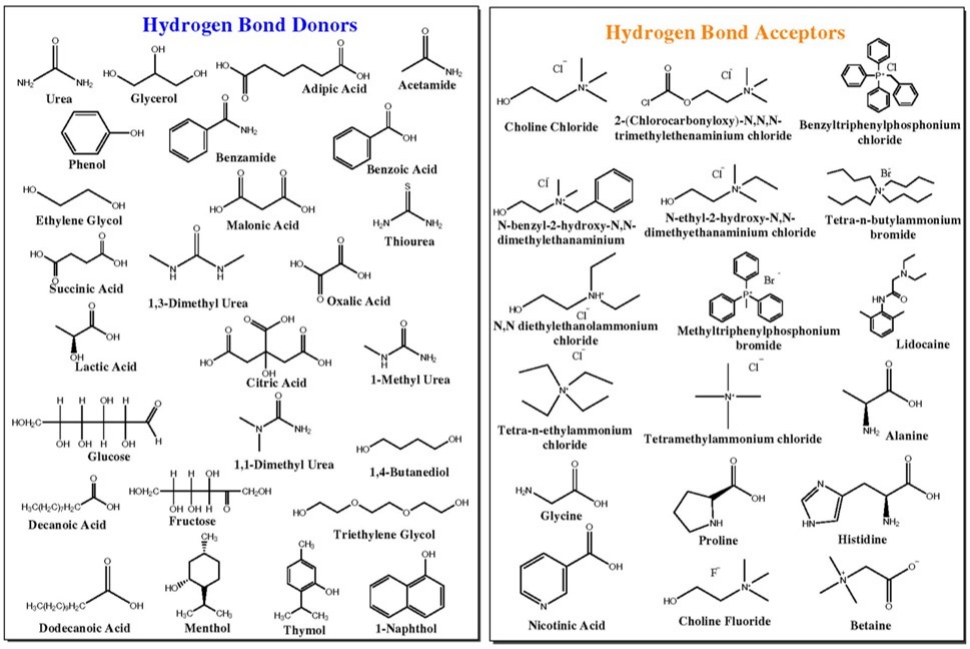

(a) DES Hydrogen Bond Donors (b) DES Hydrogen Bond Acceptors

Figure 1.1: Common components involved in the formulation of typeIII DESs. Figure from ref.[4]

The four types of DESs here described are ionic, as their formulation includes a metallic or organic salt, in an anhydrous or hydrated form. A considerable number of systems was proposed in recent years with the aim of conducting fundamental research on their mechanisms and suggesting numerous applications. In recent years, particular attention has been given to a new class of DES, defined as the fifth type, formed by the combination of non-ionic species. Unlike the other classes, almost always composed of at least one ionic species, these fifth-type DESs are characterized by strong hydrogen bonding interactions between uncharged species[27]. Despite the loss of ionic contributions, they still exhibit noticeably low melting point. In this case, it is evident that hydrogen bonding plays a significant role in lowering the eutectic point of the mixture[28, 27].

1.1.2.1 Thermodynamic behaviour of Deep Eutectic Solvents

A eutectic composition melts at a specific temperature, which is the absolute lowest of all possible values obtained by mixing components A and B in any combination. Moreover the eutectic composition melts in a single phase: to the right or left of this point, the solidification process occurs with the accumulation of one of the two components, depending on the region observed in the graph (see figure 1.2). Deep eutectic solvents, on the other hand, display an additional characteristic: the term "deep," in fact, indicates an additional depression of the melting point beyond what is expected for the same mixture in the case of ideal behavior. This implies that the solution deviates negatively from ideality. The deviation is particularly evident for the TypeV DESs[28] where we observe a substantial lowering of the melting point. The most well-known example of Type V DES was proposed in 2021 by Coutinho and coworkers[28]. They investigated a mixture composed by thymol and menthol: the melting point was measured at 60°C, below the value expected for an ideal mixture. Many physicochemical properties of these systems, such as thermal stability and viscosity, for example, are strongly influenced by deviations from ideal behavior. Therefore, it is particularly important to study the solid-liquid phase diagram (SLE) under ideal conditions to appreciate deviations from ideality . To achieve this, various methods can be employed, including computational simulations (COSMO-RS) and classical thermodynamics approaches. It

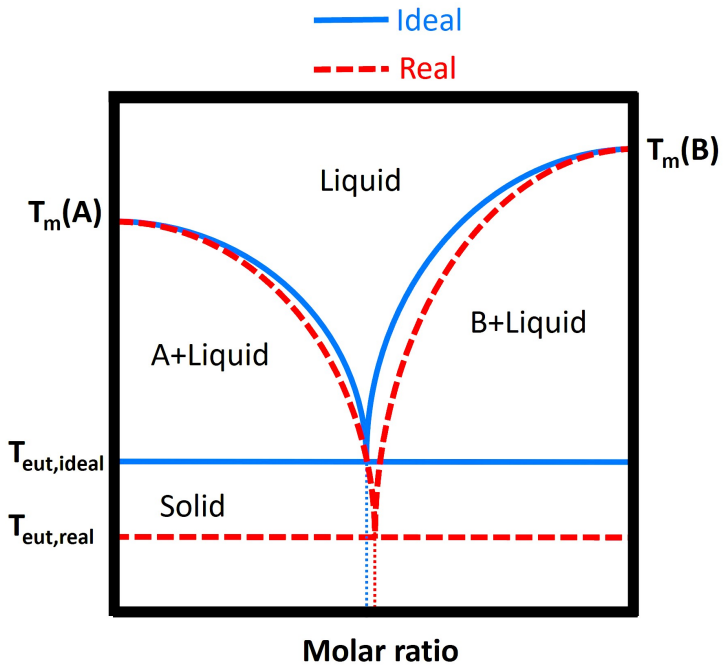

Figure 1.2: Generic phase diagram of an ideal (blue) and real (dashed red) bynary mixture

was demonstrated that such deviations depend on the strength of the intermolecular interactions that occur in the liquid phase. The choice of the hydrogen bond donor and acceptor strongly influences the non-ideality of the mixtures, as well as the formation of additional intermolecular interactions, such as halogen bonding and van der Waals interactions, can further contribute to enhance deviations from ideality. The complexity [27] of such mixtures forces us to carefully characterize their structure focusing on a meticulous analysis of the intermolecular interactions involved in the mixing. As reported in several previous works, the liquid phase is usually investigated by experimental techniques: infrared and Raman spectroscopy are currently applied to study the interactions between components[29, 30] whereas X-Ray and neutron diffraction [31] gives information on the spatial distribution of the components in the bulk. Thanks to the recent advanced computational resources, even the most complex and resource-demanding simulations can be performed in a significantly reduced time frame. A reliable modelization of the liquid can

be obtained by combining the accurate description of the short-range intermolecular interactions obtained from quantum mechanical methods [32, 33, 31], along with the description of long-range effect, that drive the distribution of the components, obtained form classical molecular dynamics.

1.1.3 Aim of the work

As described above, ionic liquids and deep eutectic solvents enclose a great number of compounds and applications, in continuous expansions. The knowledge of their physical and chemical properties, essential for rationalizing their tunability and potential applications, is still quite limited. In this thesis, we explore some properties of ionic liquids through combined approaches that involve the comparison of theoretical and experimental results. The thermal behaviour, structural and spectroscopic aspects of some DES have been investigated using various experimental techniques and computer simulations, with a background to the principles given in Chapters 2 and 3. Chapter 4 provides a detailed description of the results obtained from the structural and thermal characterization of systems classifiable as deep eutectic solvents. The main purpose of this chapter is to shed light on the nature of the intermolecular interactions between the components, in order to determine in detail the mechanisms that lead to the formation of the liquid phase. To achieve this, numerous systems were proposed. We initially investigated the role of hydrogen bonding in systems classified as Type III DES, by changing both the acceptor and the donor. The results obtained motivated us to characterize a system classifiable as Type V DES, aiming to elucidate similarities and differences with the previously mentioned systems. The phase diagrams and thermal stability were obtained through differential scanning calorimetry (DSC) and thermogravimetry (TGA). The spectroscopic characterization was conducted by infrared and Raman spectroscopies. In the case of acetate-based systems, an additional analysis was conducted in the far-infrared (FIR) region, with the aim to measure the hydrogen bond vibrational modes and follow how the distribution of different conformers changes with temperature. The FIR measurements were performed at AILES beamline of SOLEIL synchtron facility in Paris. The Raman spectra were obtained in collaboration with prof. Paola Benassi at Department of Physical and

Chemical Sciences of University of L'Aquila. Additionally, some of the proposed systems were characterized through X-ray scattering in collaboration with Prof. Olga Russina at the Department of Chemistry, Sapienza University of Rome. All systems were then modeled using molecular dynamics simulations and DFT calculations. In Chapter 5 we presented a computational study on an aminoacid based ionic liquid and its capacity to scrubble CO_2 by chemisorption. We studied the adsorption of the liquid on a pyridinic graphene surface. The nature of the interaction with the surface was investigated through molecular dynamics simulations and DFT calculations, focusing on the electron density and its changes due to adsorption. The total intermolecular interactions was factorized into electrostatic, exchange, induction and dispersion components. The liquid here presented exhibits good affinity for CO_2, and thus, we conducted a mechanistic study of the CO_2 fixation reaction by quantum mechanical methods in both the bulk and the adsorbed liquid.

Chapter 2

Computational methods

The progressive development of computer sciences in recent years provided more efficient and faster computational resources, capable of performing heavy and complex calculations. Computational problems that were prohibitively expensive until a few decades ago because they were very time-consuming and required extensive hardware resources can now be done in just a few hours on friendly sources such as personal computers or portable laptops. Computational chemistry can provide different information and the choice of the appropriate simulation method is driven from the complexity and size of the systems and from the accuracy required of the investigated property. Among several computational techniques now available, we can broadly distinguish two main branches: the methods based on quantum mechanics, known as QM, and those less expensive based on classical mechanics (MM). These two approaches differ not only in the computational costs but also in their accuracy levels: QM methods, starting from an electronic description of the system, very often provide accurate molecular geometries, reliable thermodynamic properties and meaningful spectroscopic properties, such as infrared, Raman, UV and NMR spectra[34]. Starting point of the QM methods are the wave function, the formulation of the appropriate Hamilton operator and the search for the eigenfunction of the Schrödinger equation. Since this problem may be exactly solved only for very few cases, over the years several solution methods were developed by introducing different degrees of approximation. A brief description of

these methods will be given in the following paragraphs. Despite the high efficiency of modern computational resources, quantum methods are often still too challenging for simulating large molecular aggregates. An alternative and less expensive approach for very large molecular systems are the MM methods. Intra and intermolecular interactions are described by a molecular potential, called "force field," that is parameterized on the basis of experimental measurements (NMR, IR, or other) or results of quantum chemical calculations. Many force fields are available and are chosen according to specific needs. The dynamics of the investigated molecular system can be described by both QM and MM methods to predict the time evolution of some properties by molecular dynamics simulations (MD).

2.1 Quantum calculations

The calculation of the electronic structure necessarily relies on the quantum formulation of the molecular problem. Quantum mechanics claim the system state is totally described by the associated wavefunction Ψ and solvable by the Schrödinger equation, which can be expressed using the Dirac formulation as described in eq. 2.1

$$\hat{H}\,|\Psi\rangle = E\,|\Psi\rangle \tag{2.1}$$

where E is the eigenvalue of Hamiltonian operator and represents the total energy of the studied system: the $|\Psi\rangle$ is the eigenvector of $\hat{H}$. In other words, the wavefunction can be expressed as a complex vector in a Hilbert space. By considering the classical definition of the Hamiltonian function given in equation 2.2,

$$\mathcal{H}(\dot{q}, q, t) = T(\dot{q}, q, t) + U(\dot{q}, q, t), \tag{2.2}$$

we can deduce the physical interpretation of the Hamiltonian operator, $\hat{H}$, as the operator that describes the total energy of the system written as:

$$\hat{H} = \hat{T} + \hat{U} \tag{2.3}$$

where $\hat{T}$ and $\hat{U}$ are respectively the kinetic and the potential energy operators. In this description we will not consider the temporal dependence of the Schrödinger equation. For more details see the specialized textbook [35]. Physico-chemical systems are indeed more complex than hydrogen atoms, and their QM solutions typically require the introduction of numerous approximations. In the case of a single molecule, we start from the Hamiltonian operator that describes electrons and nuclei written as the sum of the kinetic energy of electrons $\hat{T}_{el}(\vec{r})$ and nuclei, $\hat{T}_{nuc}(\vec{R})$ and the potential energy operator, $\hat{V}(\vec{r},\vec{R})$, where $\vec{R}$ and $\vec{r}$ are respectively the nuclear and electronic coordinates. Glossing over the analytic details we can write the Scrhödinger equation for a multielectronic object as:

$$\hat{H}(\vec{r},\vec{R})\,|\Psi(\vec{r},\vec{R})\rangle = E\,|\Psi(\vec{r},\vec{R})\rangle \tag{2.4}$$

The electrostatic non relativistic potential operator includes the coulombic interactions between electrons (electron-electron), electron-nuclei and nuclei-nuclei. By the analytical form of the Hamiltonian operator, we can observe that terms including both nuclear and electronic coordinates are absent, except for the electron-nucleus attraction term. Therefore, the Hamiltonian can be formally divided into two distinct contributions: one relative only to the nuclear component and the other that describes the electrons moving into a field where the nuclei, much heavier, can be essentially considered stationary. This implies that we can reasonably neglect the dynamic coupling between electrons and nuclei. If the Hamiltonian is separable, we can rewrite the equation 2.4 as two independent equations, one for the electronic component and one for the nuclear part: this useful approximation is commonly known as Born-Oppenheimer approximation and is widely used in computational physics and chemistry.

$$\hat{H}_{nuc}(\vec{R})\,|\Theta_{nuc}(\vec{R})\rangle = E\,|\Theta_{nuc}(\vec{R})\rangle \tag{2.5}$$

and

$$\hat{H}_{el}(\vec{r})\,|\Phi_{el}(\vec{r})\rangle = E\,|\Phi_{el}(\vec{r})\rangle \tag{2.6}$$

The total wavefunction $\Psi_{tot}(\vec{R},\vec{r})$, can be written as 2.7 as well as the total hamiltonian, $\hat{H}_{tot}(\vec{R},\vec{r})$ as 2.8

$$|\Psi_{tot}(\vec{R},\vec{r})\rangle = |\Theta_{nuc}(\vec{R})\rangle \cdot |\Phi_{el}(\vec{r})\rangle \tag{2.7}$$

$$\hat{H}_{tot}(\vec{R},\vec{r}) = \hat{H}_{nuc}(\vec{R}) + \hat{H}_{el}(\vec{r}) \tag{2.8}$$

The quantum chemical problems consists predominantly in the solution of electronic components of the Scrhödinger equation: many methods were proposed in the last years. In general we can differentiated these methods into two big classes:

- *ab initio* methods: the idea is to solve "directly" the Schröndinger equation of the system, although introducing the necessary approximations. Depending on the type and the degree of the approximation used different modelling methods can be identified
- Density Functional Theory: the electronic formulation of a many-body system is performed using a functional directly related to the density matrices. In general these methods can be more faster than *ab initio* ones, altough their accuracy can be lower.

In this thesis we will provide a brief overview of the fundamental principles of density functional theory. However, for a detailed explanation of *ab initio* methods, we recommend referring to specialized texts [36].

2.1.1 Density Functional Theory

The *ab initio* methods are based on the idea that the properties of a physical system can be obtained by the approximate solution of the Schrödinger equation. In the second half of the last century many efforts have be done to discover an alternative approaches to *ab initio* calculation: although these methods are able to provide excellent predictions in terms of molecular geometry, energies, thermodynamics and spectroscopy, they are often noticeably computational expensive for large molecules or solid state. For these reasons the introduction of the Density Functional Theory (DFT) in the computational chemistry revolutionized the electronic calculations. The main idea behind DFT methods consists in the description of the electronic properties of atoms and

molecules through the electron density $\rho(r)$ and its energy functional E[$\rho(r)$]. A conceptual parallelism between the wavefunction Ψ and the electronic density $\rho(r)$ appear evident. The strong theoretical efforts was correlate the electronic density $\rho(r)$ with the total energy of the systems: in other words we can rewrite the Scrhödinger equation adapted to the formulation through density functional. Many models was proposed[37]. Historically the first one was formulated by Thomas and Fermi in 1927, which proposed an approximated functional for the electronic energy based on a system of non-interacting electrons with uniform density (Thomas-Fermi density, TFD). The electron density was described using the TFD and the energy was computed by means of its minimization, exploiting the variational principle. The variational principle is one of the most useful mathematical techniques which is utilized in quantum mechanics consisting on a search of approximated eigenstate of a ground state or some excited states. The method consists of choosing a trial-wavefunction and finding the lowest expectation value of the energy. The variational methods can be formalised as follow:

$$\epsilon[\Psi] = \frac{\langle\Psi|\,\hat{H}\,|\Psi\rangle}{\langle\Psi|\Psi\rangle} \tag{2.9}$$

and the variational method affirms:

- $\epsilon \geq \mathrm{E}_0$ with E_0 the lowest energy eigenstate of the hamiltonian
- $\epsilon = E_0$ if Ψ is equal to the exact wavefunction of the system.

For a more detailed description see the specialist text [35]. The Thomas-Fermi approach involves two general problems. The first one is theoretical, in that the variational method is used without any theoretical base. The second one is the bad description of the molecular systems: The Thomas-Fermi (TF) approach yields accurate results for describing isolated atoms and solid-state systems whereas, on the contrary, TF predicts that atoms always repel each other and molecules tend to strongly dissociate. For these reasons the TF approach remained shelved for several years. The interest was aroused when Hohenberg Khon successfully developed a solid theoretical framework for DFT. In particular they pinpointed two fundamental theorems.

First theorem: The electronic density $\rho(r)$ completely and unequivocally describes the properties of a polyelectronic systems, in a similar manner to what occurs in quantum mechanics with the wave functions.

If in quantum mechanics theory Ψ_0 represents the ground state of a generic system, then there must exist a function of $\rho(r)$ that allows to calculate the expectation value for each physical observable, as generalized in the equation 2.10:

$$\rho(r) = \langle \Psi(\rho) | \hat{O} | \Psi(\rho) \rangle = O[\rho(r)] \tag{2.10}$$

The equation 2.10 in other words demonstrate the relation between Ψ and $\rho(r)$ and can be imagined as the link between the wavefunction-based formulation and the density functional-based formulation of quantum mechanics. One of the greatest strengths of DFT theory is its ability to reduce the dimensionality of the system, because the density function $\rho(r)$ is defined in three dimension (x,y,z), unlike the wavefunction. Furthermore, the generic O[$\rho(r)$] functional does not directly depend on the system but is defined as universal. It is clearly that its functional form is not always known, but its existence is certain. A compelling example can be observed considering the mono-electronic operator for which the the functional can be written as:

$$\hat{O}[\rho] = \int \hat{O}(r)\rho(r)dr \tag{2.11}$$

The generic functional $\hat{O}[\rho]$ just described must exists for each operator acting on $|\Psi\rangle$ and therefore also for the Hamiltonian operator. Taking in account the brief introduction at the quantum mechanics reported in the previous paragraph, we can write:

$$E[\rho] = \langle \Psi | \hat{H} | \Psi \rangle = \langle \Psi | \hat{T} + \hat{V} + \hat{W} | \Psi \rangle = \langle \Psi | \hat{T} + \hat{W} | \Psi \rangle + V[\rho] \tag{2.12}$$

Observing the equation 2.12 it can affirm that the $E[\rho]$ has the form of:

$$E[\rho] = F_{HK}[\rho] + V[\rho] \tag{2.13}$$

where F_{HK} is the universal functional, also known as bielectronic term and $V[\rho]$ is the functional of the systems.

Second theorem: The minimization of the density functional can be performed using the variational theorem.

This theorem is rigorously valid only in the case of F_{HK} is exact: regrettably this is not the case in practical applications. However it is important to acknowledge that the variational theorem, in the context of the conventional wavefunction formulation, is always valid, but the search of the minimum energy is frequently a challenging and intricate procedure.

2.1.1.1 Khon-Sham approach

Notwithstanding the theoretical progress introduced with the Hohenberg-Khon approach, the high number of approximation has made the DFT scarcely used. The interest revived in 1965 when Khon and Sham introduced two important considerations:

- the electronic density can be formulated through orbitals
- the problem can be simplified considering a system composed by non-interacting particles

As a direct consequence of these two assumptions we can rewrite the Hamiltonian omitting the W term of the equation 2.12 that considers the interactions between the particles, leading to the Hamiltonian of the following form:

$$\hat{H}_s = \hat{T} + \hat{V}_s \tag{2.14}$$

Assumed the validity of the Hohenberg-Khon theorems and the existence of a functional that describes the energy, we can rewrite the $E[\rho]$ as:

$$E_s[\rho] = T_s[\rho] + \int v_s(r)\rho(r)dr \tag{2.15}$$

In equation 2.15 the term T_s is the universal functional of non-interacting systems. As previously mentioned, the exact functional of the universal functional is not known, but it is possible to recur at approximated forms. The solution of the equation 2.15 for a molecular system consists in a Slater determinant of N spin-orbit functions and the density function corresponding at this

determinant is:

$$\rho(r) = \sum_{i=1}^{N} |\phi(r)|^2 \tag{2.16}$$

The Khon-Sham equation arises starting by the consideration that T_S is a good description of the kinetic energy. The energy functional has the form of:

$$E[\rho] = F_{HK} + V[\rho] \tag{2.17}$$

At this point the universal functional F_{HK} can be expressed, reintroducing the W contribute as:

$$E[\rho] = T_s[\rho] + J[\rho] + V[\rho] + V[\rho] + E_{xc}[\rho] \tag{2.18}$$

where E_{xc} is commonly defined as correlation-exchange functional and has the form of:

$$E_{xc}[\rho] = W[\rho] - J[\rho] + T[\rho] - T_s[\rho] \tag{2.19}$$

This term contains non-classical terms of correlation-exchange energy and it is important to emphasize that the term $T - T_s$ cannot be calculated because the exact value of T_s is not known. The original idea when this approach was developed was to minimize this difference as negligible as possible. The resulting pseudo-Schödinger equation arising from these theory can be now written as:

$$\left[-\frac{1}{2}\nabla^2 + V_{KS} \right] |\phi_i\rangle = \epsilon_i \, |\phi\rangle_i \tag{2.20}$$

where the quantum states described by the ket are konwn as Khon-Sham orbitals and the term between the square brackets are known as Khon-Sham hamiltonian. The groundwork laid by the approach proposed by Khon and Sham has made DFT a powerful computational tool with lower computational costs compared to traditional *ab initio* methods. This makes DFT a suitable tool for studying more extended systems. Another interesting aspect lies in the fact that the correlation-exchange term can be further developed and tailored to specific computational requirements. The different ways to express the E_{xc} lead to different approximation degrees:

- *Local Density approximation (LDA)*: the E_{xc} depends only by the local density and often the description of chemical systems results inaccurate. An example of this approximation is the Slater exchange functional.

- *Generalized Gradient Approximations (CGA):* they depends simultaneously by the density value and by its gradient. Many arbitrary parametres are added to improve the accordance between experimental and theoretical results. Among these we can identify the Becke exchange functionals [38] and the Lee, Yang and Parr correlation functionals [39], which give rise to the group of functionals commonly referred to as BLYP.

- *Meta-generalized gradient approximation (MGGA):* the functional also depends on the second-order derivative of the density. This approach allows a bigger flexibility in the description of interactions and molecular properties. An example can be the TPSS functional (Tao-Perdew-Staroverov-Scuseria) [40]

- *Hybrid functionals:* they are a new class of functionals introduced in the last years. A fraction of exchange correction defined at the Hartree-Fock level is added to the Khon-Sham functional. The most used hybrid functional is B3LYP[41], containing three Becke parameter of correlation and Lee, Yang and Parr parameter for the exchange terms.

2.1.2 Molecular properties obtainable by DFT calculations

In the previous paragraph some theoretical basis of DFT methods was explained with the aim to supply a general background on this computational technique. Thanks to their high computational scalability and good reliability in predicting molecular properties, most researchers adopt DFT methods to determine reaction energies, equilibrium geometries and molecular spectra.

2.1.2.1 Geometry optimization

The molecular geometry can obtained by minimization of the potential energy calculated by some of the QM methods previously described. Various algorithm are available to this purpose and one of the most common, applied both in molecular mechanics and quantum mechanics methods, is known as *steepest descendent* algorithm. Starting from a reasonable initial nuclear configuration, the potential energy surface (PES) is computed by solving the electronic component of the

Schrödinger equation: its the analytical form depends therefore on the specific method chosen to describe the electronic component. In general we can distinguish two general approach:

- **Global methods**: deterministic methods that explore the PES allowing the geometries to overcome potential energy barriers; the new geometric configurations in each cycle are obtained from the output of the previous one
- **Stochastic methods**: methods that modify the molecular geometries varying the structure with random and casual increments. One of the most known stochastic methods is Montecarlo method.

More in general the minimization algorithm are classified based on the basis of the order of the derivatives of PES calculated with respect to the geometrical coordinates.

- **Zero order**: in methods such as the simplex method, the derivatives are not calculated directly, but the optimal solution is sought by evaluating and comparing the objective function values at different points in the parameter space.
- **First order**: the search of the minimum is driven by the calculation of the first order derivative. One example can be found in the steepest descendent method.
- **Second order**: Newton-Rapshon method, which computes the first and second order derivatives.

The value of the first or second derivatives of PES with respect to each nuclear coordinate drive the changing of all the coordinates in order to decrease the potential energy. The newly obtained geometry is used as input for the subsequent step, initiating an iterative procedure that stops when the convergence criteria (typically pre-set by the software but customizable by the user) are reached. The stationary point determined on PES can be:

- **the absolute minimum**: the equilibrium structure
- **a local minimum**: a stable structure alternative to the equilibrium one

- **a saddle point**: an unstable structure of the molecule (transition state if critical point is first order saddle point).

The nature of each critical point is characterized by the calculation of the second derivatives of the potential and by the analysis of the sign of the vibrational frequencies. A minimum structure shows all real frequencies while transition states should possess one and only one imaginary frequency.

2.1.2.2 Vibrational frequencies

The study of the molecular vibrations is a fundamental step in the structural determination. The internal motions of a molecule are analysed in terms of normal mode (NMA) by describing small oscillation around its equilibrium geometry. Starting from a potential energy function expressed in terms of 3N cartesian coordinates, with N equal to the number of nuclei, we can describe the molecular vibrations as a set of 3N coupled harmonic oscillators. The initial coordinates can be linearly combined to give a new set of coordinates (normal modes) that allow to describe the molecular vibrations as a set of independent harmonic oscillators. The vibrational frequencies are obtained by classic mechanics as solution of the equation of motion as follows. The matrix form of the vibrational kinetic energy is reported in equation 2.21

$$K = \frac{1}{2}\dot{x}^T M \dot{x} \tag{2.21}$$

where $\dot{x}$ is a 3N-dimensional vector of the velocities, M a square 3N-dimensional matrix whose diagonal matrix represent the nuclear masses and T represent the transpose matrix. Similarly, the potential energy can be expressed as reported in equation 2.22

$$V = E_0 + \frac{1}{2}x^T H x \tag{2.22}$$

where E_0 is the value of the potential energy at the minimum and H the hessian matrix, whose elements are the second derivatives of the potential energy (force constants) with respect to the 3N cartesian coordinates .

$$H_{ij} = \frac{\partial^2 E}{\partial x_i \partial x_j} \tag{2.23}$$

In order to lightening and simplifying the calculations the problem is currently rewritten introducing the mass weight coordinates $\sqrt{m_i x_i}$: with this reformulation the matrix M in the equation 2.22 disappears. The equation of motion for each coordinate is given by the following equation:

$$\ddot{x} = -\sum_{j=1}^{3N} H_{ij} x_j \tag{2.24}$$

considering that the hessian matrix now can be rewritten as $\frac{H_{ij}}{\sqrt{m_i m_j}}$. The nuclear oscillations near to the equilibrium positions can be expressed with an harmonic functions, as reported in the equation 2.25

$$x_i = A_i cos(\sqrt{\lambda} t) + \phi \tag{2.25}$$

and consequently the system of 3N equation is expressed with 2.26

$$\sum_{j=1}^{3N} A_j (H_{ij} - \delta_{ij}\lambda) = 0 \tag{2.26}$$

Solutions of the previous equation, written in matrix form, leads to the eigenvalue problem

$$det|H - \lambda_k I_{3N}| = 0 \tag{2.27}$$

with I equal to the $3N \times 3N$ identity matrix and the eigenvalue λ_k related to the vibrational frequencies by 2.28

$$\omega_k = \sqrt{\lambda_k} \tag{2.28}$$

The normal mode coordinates are the set of the eigenvectors q_k of eigenvalues problem 2.27.

2.2 Molecular Dynamics methods

Despite the remarkable accuracy, QM methods give a static description of the molecular system without including any dynamic effect. Furthermore, the high computational demand required from QM methods compel to reduce the size of the systems investigated, leading very often to a bad description of long-range effects, that play a crucial role in determining the properties of condensed phases. As alternative approach, liquids or disordered materials are simulated by classical

molecular dynamics. Quantum mechanics and classical mechanics should be therefore viewed as complementary rather than mutually exclusive approaches. A handful strategy is to describe the short range effects (intra and intermolecular interactions) by QM methods by studying small molecular clusters and to reproduce the long range effects by the studying the bulk and dynamic properties by MD simulations of boxes containing a few thousand of molecules. MD is based on classical physics and statistical mechanics. The theory underlying molecular dynamics simulation requires a lengthy and complex description. This section is intended to provide an introductory overview of the theoretical background and a brief explanation of the simulation methods used in this thesis. The energy of a physical system can be formulated by classic mechanics through the Langrangian formalism:

$$\mathcal{L}(\dot{q}, q, t) = T(\dot{q}, q, t) - U(\dot{q}, q, t) \tag{2.29}$$

or using the Hamiltonian function:

$$\mathcal{H}(\dot{q}, q, t) = T(\dot{q}, q, t) + U(\dot{q}, q, t) \tag{2.30}$$

where the U and T are respectively the potential and kinetic energetic contributions. These two expressions of the energy depend by the impulse ($\dot{q}$), the position (q) and the time (t). In MD calculations, the potential energy was often referred to as a force field (FF). Over the past year, numerous FFs have been developed with a focus on the physical properties required for specific applications. Efforts have been made to refine the functional forms of the FFs with the goal of better capturing the intricacies of molecular systems and their interactions. These developments were aimed at improving the predictive capabilities of MD simulations and enabling more accurate modeling of complex molecular behavior in various applications. Before describing the most used FF in soft matter studies, we can analyze in general a FF as follows:

$$U = U_{INTRA} + U_{INTER} \tag{2.31}$$

where U_{INTRA} is the potential energy term arising from intramolecular contributions (bonds, planar and solid angles) and U_{INTER} is the term arising from the intermolecular interactions

(Coulombic and Lennard-Jones potentials). The total potential can be written in the following formula:

$$U = U_{bond} + U_{ang} + U_{dihead} + U_{Coulomb} + U_{L-J} + U_{impr} \tag{2.32}$$

Each term given in the previous equation has an analytical form. U_{bond} refers to the bond energy and can be simply expressed by an harmonic potential. Considering the general i-j couple of atoms, we can write the bond potential as:

$$U_{bond}(r_{ij}) = \frac{1}{2}k_{ij}\left(r_{ij} - a_{ij}\right)^2 \tag{2.33}$$

where k_{ij} is the force constant and a_{ij} the equilibrium bond distances. Analogously we can define the potential related to the angular contribution as an harmonic potential, as follows:

$$U_{ang}(\theta_{ijk}) = \frac{1}{2}k_{ij}\left(\theta_{ijk} - a_{ijk}\right)^2 \tag{2.34}$$

where k_{ijk} and a_{ijk} are the force constants and the values of the equilibrium bond angles, respectively. The form of the third therm is different: we can indicate the potential related to the dihedral angles as reported in the following equation.

$$U_{dihead}(\phi_{ijkl}) = \frac{1}{2}p\left(1 + cos(n\phi + \phi_s)\right) \tag{2.35}$$

A dihedral angle can be defined as the solid angle formed by the connection of four atoms. p is a torsional barrier, ϕ the phase angle and n represents the periodicity of the function. Switching to the intermolecular terms, we can express the electrostatic interaction as a classical coulombic potential.

$$U_{coulomb}(q_i, q_j, r_{ij}) = \frac{q_i q_j}{\varepsilon_r r_{ij}} \tag{2.36}$$

where q_i and q_j are the charges of the two interacting particles, r_{ij} is the distance between the charges and ε_r is the dielectric constant.

The Lennard-Jones potential describe the attractive and repulsive interactions established between the particle. This empirical potential is strongly dependant by the distance.

$$U_{LJ}(r_{ij}) = 4\gamma_{ij}\left(\left(\frac{\sigma_{ij}}{r_{ij}}\right)^{12} - \left(\frac{\sigma_{ij}}{r_{ij}}\right)^{6}\right) \tag{2.37}$$

In the last expression γ_{ij} is the depth of the potential well, σ is the radius of the sphere used to approximate the atoms or molecules and r_{ij} is the interparticle distance. The van der Waals interaction are considered in this potential and are described by the six-order term. The twelve-order term describes the repulsive interaction, typically established at short distances. In ionic liquids and deep eutectic solvents (in general in the condensed phases) one of the most important interaction is hydrogen bonding. In several molecular systems hydrogen bond network is indeed the most important interaction that leads to the formation of the condensed phase. For this reason this term must be included in the force field and in the last years various FFs have been developed with this aim. An analytical form often used is the following:

$$U_{impr} = E_{HB}\left[5\left(\frac{R_{HB}}{R_{DA}}\right)^{12} - 6\left(\frac{R_{HB}}{R_{DA}}\right)^{6}\right] cos^{4}(\theta_{DHA}) \tag{2.38}$$

where θ_{DHA} is the hydrogen bond angle, R_{DA} is the distance between acceptor and donor atoms. E_{HB} and R_{HB} are the energy and distance of hydrogen bond, respectively. This last term of FF is a three body potential. From classical physics, the forces acting on an object could be obtained by the calculation of the first order derivatives of the potential energy. The force field are parametrized by quantum chemical calculation or, rarely, using experimental data.

2.2.1 Common Force Fields involved in soft matter investigation

As mentioned in the previous section, the research on the best force field has interested the scientific community in the last years. Some force fields included in the most common and used MD packages (GROMACS[42], for instance) have been developed for biomolecular applications. However they are usually used also in MD simulations of soft matter where the situation is slightly different. In these systems one of the biggest problems concerns the presence of non-standard residues in the force field. Maintaining the parallelism with biomolecules, we know that the proteins are predominantly made by aminoacids and the most common FFs in general include all aminoacids or other biological fragment composing the biological systems. For this reason we do not need to parameterize these fragments every time. Soft matter are instead composed by

innovative materials and often by new synthesized components that require specific parameterization procedures before to start MD simulations. The first step often concerns the values of the atomic charges that are obtained by *ab initio* methods and transferred to the FF. Sometimes, in order to improve the agreement between experimental results and theoretical models, especially when the comparison is done with X-ray results, the charges are scaled by a specific factors as illustrated in many studies [43, 44, 45]. Atomic charges are calculated by different methods, often on the basis of the restrained electrostatic potential (RESP)[46].

2.2.1.1 Fixed charges and polarizable FF

In most MD studies the charges remain fixed and constant during the simulation. The main advantages of this approach are an easy procedure of parameterization of the FF and a quite fast MD simulation. An important disadvantage is the fact that the electrostatic interactions are often overestimated with consequent excessive rigidity of the systems. The force field should be take into account that the molecules could undergo structural deformations during the simulation, modify the electronic distribution and consequently change the values of atomic charges. This polarization effect can be therefore an important factor in the description of the condensed phase and polarizable force fields have been introduced to take into account this dynamic polarization. Some examples can be found in AMOEBA (Atomic Multipole Optimized Energetics for Biomolecular Applications[47]) force field and the Drude polarizable force field[48]. Unlike fixed charge force fields, polarizable force fields allow the charges to vary in response to the local electric field. This provides a more accurate description of the electrostatic interactions and can capture phenomena such as induced dipoles and charge transfer. One advantage of polarizable force fields is their ability to accurately model systems with significant charge redistribution, such as ionic liquids, metal ions, and polar solvents. Unfortunately, polarizable force fields are computationally more demanding compared to fixed charge force fields due to the additional parameters required to describe atomic polarizability. In addition, the initial parameterization and validation can be a complex and demanding task.

For all these reasons we preferred to use fixed charges FFs for all the MD simulations described in this thesis. In particular we adopted some of the most applied FFs such as GAFF[49], GAFF2[50] and OPLS-AA[51]. In particular, the generalized atomic force field (GAFF) is based on Amber force fields for protein and nucleic acids and was developed with the aim to introduce the parameter for organic molecules and unconventional residues. This potential is particularly flexible and allows the calculation of a large ensemble of atoms (H,C,N,O,P,S, halogen and other heteroatoms). The good performances of this FF made GAFF a good candidate for studying ionic liquids or more in general liquid systems, as demonstrated by the high number of works published in the last years.

2.2.2 MD simulation of liquids

In the perspective of conducting an accurate simulation and obtaining reliable results, the molecular dynamics simulations were carried out following the scheme depicted in Figure 2.1. The initial configuration has been obtained by a random distribution of the components into a box with an appropriate software (i.e. Packmol[52]). The parametrization of the system started with the calculation of the atomic charges at QM levels using the Restrained electrostatic potential atomic partial charges algorithm[46]. The molecules were then parametrized with the typical parameters of the selected force field (angle, dihedrals, bond distances). Many thousands of energy minimization cycles are required to remove the geometric stress or molecular overlap due to random distribution. At this point the system is ready for the dynamic simulation: the box has never been coupled with any thermal bath and the temperature can be formally considered to be 0K. The first round of simulations, in general at temperature higher to the physical conditions (550K), can be exploited to pre-equilibrate the systems and to generate velocities and kinetic energies. We refer this procedure as NVT to indicate a system with number of particles (N), volume (V) and temperature (T) as constants. The high temperature allows to increase the fluidity of the liquids, improving the equilibration procedure. After this short NVT, the system can be simulated introducing the coupling with pressure (NPT ensemble), in order to calibrate the density (possibly

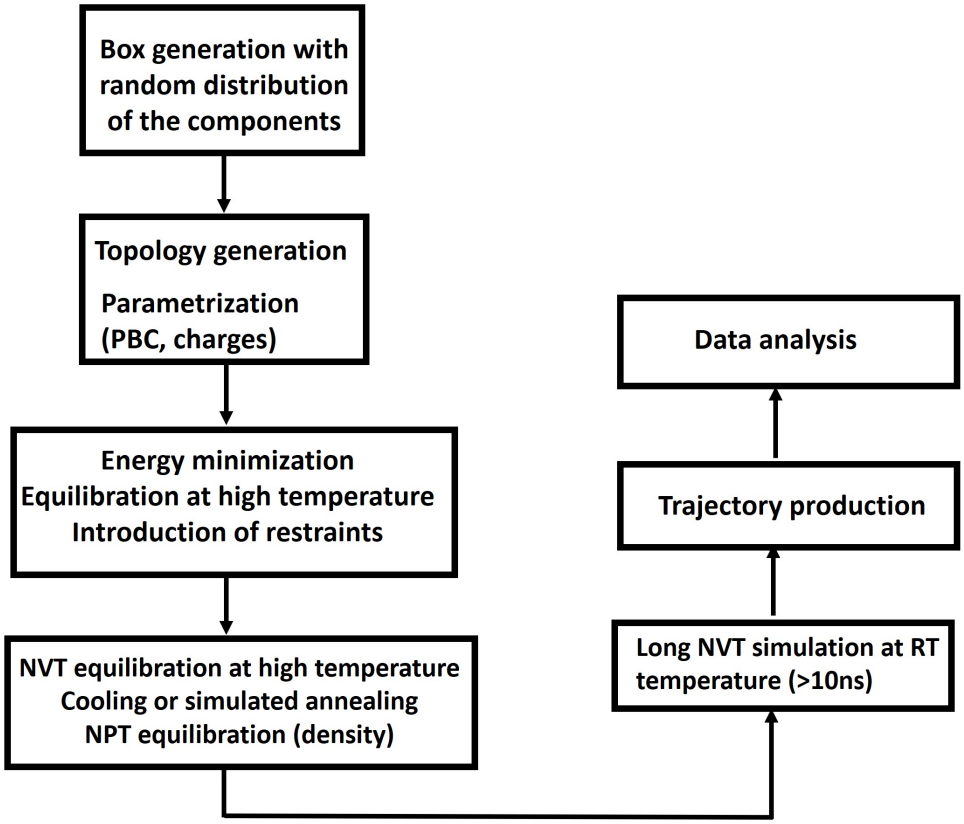

Figure 2.1: Proposed MD procedure

with the experimental value). The temperature can be decreased following two approaches:

- step by step: the temperature can be decreased step by step, choosing a program of temperature and performing several NVT (or NPT) simulations.
- by annealing (SA): the temperature is progressively and continuously varied. SA allows for a better equilibration; generally one or more cycles are required to achieve good SA performances.

When the correct temperature was achieved, the system was simulated for several nanoseconds and the trajectories were sampled: longer trajectories are always better approximations to the ergodic limit.

The ergodic hypothesis postulates that, over a sufficiently long time, a system will explore all possible states in the phase space with equal probability, providing a statistical average that is equivalent to a time average. The Liouville theorem affirms that in conservative systems the flow of probability densities in phase space remains constant over time. The constancy ensures that the trajectories explore all possible states. On these bases, we can consider the time average obtained by MD simulations compatible with the average in the microcanonical ensemble (NVE). However, to better reproduce the real systems is more convenient to perform simulations on other statistical ensemble, as NVT and NPT. In order to maintain volume or pressure constant during simulations various computational strategies are employed, enabling the simulation of barostats and thermostats. Among various implementations of barostats and thermostats proposed so far, in liquid simulations the most used ones are the Nosè-Hoover chain thermostat and Parrinello-Rahman.

The idea behind the Nosè-Hoover chain thermostat is to couple the system with an external thermal bath (reservoir), according to the statistical thermodynamic definition. The implementation introduces a fictitious degree of freedom with the aim to retro-regulate the kinetic energy. By dynamically adjusting the fictitious variables and heat bath coupling, these thermostats ensure that the system's temperature remains close to the specified target during the simulation time[53]. Similarly, the Parrinello-Rahaman barostat employs a feedback control mechanism: the barostat introduces a fictitious variation in the volume of the system and couples it to a pressure tensor. This enables the system to adjust its volume to maintain a desired pressure[54].

2.2.3 Structural properties obtained by means of MD simulations

The MD simulations carried out in these thesis were performed with the aim to determine the structural properties of the liquids. By observing the evolution of an observable in time, we can obtain its time-averaged value. For example, the temporal evolution of the nuclear positions during the molecular dynamics yields essential insights into the average geometrical properties of the system, as angles, dihedral angles and bond lengths. The high number of particles in motion

in the simulation box does not allow for a direct and visual analysis of molecular coordination through the screenshot of the simulation and force to recur to an analytical approach. The distribution functions are a good and useful approach to understand the intermolecular interactions and structural properties in the liquid bulk. The radial distribution functions (RDFs or g_{AB}(r)) are defined as reported in equation 2.39

$$g_{AB}(r) = \frac{\langle \rho_B(r) \rangle}{\langle \rho_B \rangle_{local}} = \frac{1}{\langle \rho_B \rangle_{local}} \frac{1}{N_A} \sum_{i \in A}^{N_A} \sum_{i \in B}^{N_B} \frac{\delta(r_{ij} - r)}{4\pi r^2} \tag{2.39}$$

where ρ_B is the particle density of B at a distance r around A, $\langle \rho_B \rangle$ is the normalized density over the total space around to A with r_{max} as the maximum distance. The radial distribution function g(r) describes how the density of matter varies as a function of the distance from a given reference point and quantifies the probability density of finding other particles at different distances r from the reference particle. It is evident that g(r) is zero at r=0 and tends to one at infinite distances, as demonstrated by the limits reported in the system 2.40

$$\begin{cases} \lim_{r \to 0} g(r) = 0 \\ \lim_{r \to \infty} g(r) = 1 \end{cases} \tag{2.40}$$

An important observable directly obtainable from g(r) is the coordination number, obtained through the 2.41

$$n = 4\pi \int_{r_1}^{r_2} r^2 \rho g_{AB}(r)\, dr \tag{2.41}$$

that can be obtained integrating the g(r) multiplied by the number density within the volume, imposing the extremes of the peak (r_1 and r_2) as limits of integration[55].

As we will discuss more extensively in the next chapter, liquids and more in general soft matter can be efficiently studied by means of X-ray diffraction or neutron scattering: these techniques, indeed, enable the investigation of the spatial arrangement of components in the bulk. The structural information is obtained through the experimental determination of the so-called structure function I(q) which is formally related to the total radial distribution function (in distance domain)

through a Fourier transform relationship. The analysis of the molecular dynamics trajectories facilitates the interpretation of the experimental I(q) functions, as it allows for the direct calculation of the radial distribution function. The analytical form of the I(q) is reported in the equation 2.42

$$I(q) = \sum_{i=1}^{N} x_i f_i^2(q) + \sum_{i \neq j}^{N} x_i x_j f_i(q) f_j(q) \frac{\sin(q r_{ij})}{q r_{ij}} \tag{2.42}$$

where the variable q is the scattering variable and is approximately related to the distance through the following relation $q = \frac{4\pi}{r}$. r_{ij} is the interatomic distance, f the atomic scattering factor and x_i the number concentration of i-th specie.

2.3 Computational approaches employed for investigating the proposed systems

Quantum chemical calculations

The computational investigations carried out in this doctoral thesis were primarily performed to characterize the structure of the deep eutectic solvents and ionic liquids investigated. The computational analyses conducted in this doctoral thesis were performed to characterize the structure of the proposed deep eutectic solvents and ionic liquids. The investigation involved the application of multiple computational models and the execution of DFT calculations at various theoretical levels, elucidating both geometries and interaction energies. According with the different dimension of the molecular clusters and the diverse nature of the different chemical nature of the components in the mixtures, various functionals were chosen for investigating the systems. All calculations were performed by means of Gaussian16[56] and Spartan20[57] packages. The equilibrium geometry, energy association, and theoretical vibrational spectra of choline chloride-imidazole, tetrabutylammonium bromide-imidazole, as well as Phenol-Cyclohexanol, were modeled using the Minnesota meta-hybrid Generalized Gradient Approximation (meta-GGA) functional M062X[58] employing the 6-311G** basis set. The vibrational spectra and equilibrium geometries of the mixtures composed by choline acetate and tetrabutylammonium acetate with ascorbic, citric, and

maleic acid were modeled at the B3LYP[41]/6-31+G** level of theory. The conformational search (in the case of ChAc-MA) was carried out at the molecular mechanics level using the routines available in the Spartan20 software. The obtained geometries were subsequently optimized at the B3LYP/6-31G** level of theory. The vibrational spectra were calculated only for the structure within a maximum range of 5 kJ/mol from the absolute minimum. The quantum chemical analysis of the interaction between ionic liquids and N-doped graphene sheet, as discussed in Chapter 5, was performed using the hybrid functionals ωB97X-D [59] with a 6-311++G** basis set. This functional incorporates long-range exchange effects along with a semi-classical London-dispersion correction The functional was selected to consider the improved efficacy in describing extended π-conjugated systems. We have decided to use different methods and levels of calculation, taking into account various systems, the different sizes of simulated molecular clusters, and their specific characteristics. All calculation were performed including an implicit solvent model (PCM) and evaluating the effect of the polarity: although some published paper[60, 61] demonstrated that a good ε_r for ILs and DESs can be expressed with ε_r values ranging from 10 to 20, we decided to asses the effect of the polarity by varying the dielectric constant between 15 and 40. The electronic interactions were characterized using various computational approaches. Atoms in molecules (AIM) were conducted by means of AIMALL software[62], charge transfer between graphene and IL was studied by Visualization Structural Analysis program[63] and evaluated from Bader charge [64] analysis. The reduced density gradient (RDG) was carried out by MultiWFN package [65]. The symmetry-adapted perturbation theory (SAPT [66, 67, 68]) was conducted at SAPT0/6-311++G** level using the Psi4 software [69].

Molecular Dynamics Simulation

Both DESs and ILs were also studied by means of classical molecular dynamics (all atom force field), performing the calculation using GROMACS2019.6 sofwtare[42] In this case a more uniform approach was chosen for all systems. All systems were parameterized with Generalized Amber Force Field (GAFF) force field[49, 50]: the partial atomic charges were computed using the Restrain

Electrostatic Potential (RESP [46]) algorithm at HF/6-31G* level of theory. The use of HF/6-31G* RESP charges, as reported in previous works, is a promising approach for the parametrization of ionic systems in the liquid phase and RESP charges exhibits a high compatibility with the GAFF force fields[70]. The input files (coordinates and topologies) were prepared using Antechamber and Leap available in Amber2018 tools[71]. Electrostatic interactions were computed using the Particle Mesh Ewald (PME) method under periodic boundary conditions and all bonds involving hydrogen atoms were constrained with Linear Constrain Solver (LINCS)[72]. Cutoff-radii for van der Waals was imposed to be 10Å. In figure 2.1 we reported a schematic representation of the MD protocol proposed for the simulation of liquids. The starting configurations were generated putting randomly the components in cubic boxes using Packmol[52]. All simulated boxes consisted of 1000-2000 molecules of liquid, respecting the desired molar compositions. The energy of the starting boxes was minimized through 10^5-10^7 iteration cycles. All simulations started with a preliminary shorts NVT simulations (1ns) at 550K, in order to increase the fluidity of the liquids, ensuring a better mobility of the components. The structural inhomogeneities were corrected by short NPT simulation (1-2 ns). All systems were cooled at 400K and their densities were calibrated by NPT simulations. Final trajectories were obtained by long NVT simulation at 400K (20-50 ns) and collected every 1000 steps. The trajectories were analyzed using TRAVIS software [73].

Chapter 3

Experimental Methods

3.1 Vibrational Spectroscopy

The theoretical background of molecular spectroscopy lies in the theory of the interaction between electromagnetic radiation and matter. The electromagnetic spectrum spans a continuous range of energy, and each energy value corresponds to a wave travelling at the speed of light. In simpler words, electromagnetic waves can be considered as a propagation in the space through an oscillation of the electric and magnetic fields. In general a wave is characterized by its wavelength, amplitude and frequency. The amplitude represents the maximum size of the wave, which corresponds to the intensity of the signals. The wavelength λ corresponds to the distances between two adjacent maxima (or minima) of the wave and the frequency ν is the number of the oscillation per unit of time, that is inversely proportional to λ. The energy of an electromagnetic wave is directly linked to its frequency and is expressed by the Planck relations:

$$E = h\nu \tag{3.1}$$

where h is the Planck constant and its value is $6.62 \cdot 10^{-34} J \cdot s$. Electromagnetic waves can also be described through wavenumber ($\bar{\nu}$), which represents the number of waves per unit of lengths,

as described in the equation 3.2:

$$\bar{\nu} = \frac{1}{\lambda} \tag{3.2}$$

$\bar{\nu}$ is in general expressed in cm^{-1}, especially in infrared and Raman spectroscopies. The portion of the electromagnetic spectrum relevant for vibrational spectroscopy corresponds to wavenumbers ranging from approximately 20 cm^{-1} to 8000 cm^{-1}. This encompasses the spectral regions commonly known as far IR, or FIR (20-700 cm^{-1}), mid-IR or MIR (700-4000 cm^{-1}) and near IR or NIR (up to $\sim$ 12500 cm^{-1}). From a physical standpoint the interaction of light with matter is a quantum mechanical phenomenon. The absorption of a photon by molecules involves discrete energy levels, leading to quantized energy states. Consequently, when irradiating a molecule in a given state (state 1) with a monochromatic beam, the radiation is absorbed, causing the system to transition to state 2. By placing a detector capable of capturing the radiation after the interaction with the molecule, we observe a reduction in light intensity. When employing a white beam, which consists of polychromatic radiation containing a range of wavelengths and energies, the molecular systems selectively adsorb radiation with frequencies predicted by equation 3.1. Other frequencies remain unaltered, leading to the generation of an absorption spectrum. The emission spectrum is obtained recording the inverse processes, collecting the radiation associated with the process of returning from the excited state 2 to the relaxed state 1. Considering electromagnetic radiation composed by photons exhibiting a spectrum of energy and frequency, the interactions with matter generates different types of transitions, including electronic, vibrational and rotational. These transitions represent the fundamental physical phenomena investigated by different spectroscopic techniques. Each technique is distinguished by the energy of the absorbed photon and, consequently, the type of transition it induces. In this thesis we will provide a brief theoretical overview of the fundamental principles and some technical aspects of infrared spectroscopy.

3.1.1 Infrared Spectroscopy

The fundamental phenomenon on which infrared spectroscopy is based, as briefly mentioned, is the molecular vibration. Considering a generic molecule, denoted as A-B, the absorption of an incident photon causes a deformation in the interatomic distance, thereby instigating a vibrational motion within the chemical bond. In the first instance this concept can be described trough a classical model, considering the chemical bond as a classical spring. In other words the problem can be formalized using the classical theory of the harmonic oscillator. The molecular system A-B in absence of perturbation effects is at the equilibrium distance r_{eq} and the compression or extension can be treated as due to an elastic force given by the Hooke's law:

$$f = -k(r - r_{eq}) \tag{3.3}$$

where k is the force constant and r the internuclear distance, respectively. The functional form of the harmonic potential is:

$$U = \frac{1}{2}k(r - r_{eq})^2 \tag{3.4}$$

An elastic bond, describable as a spring, vibrates at a proper frequency determined by the masses of the two particles (atoms, in the molecular case):

$$\omega = \frac{1}{2}\sqrt{\frac{k}{\mu}} \tag{3.5}$$

where μ is the reduced mass $\left(\mu = \frac{m_1 m_2}{m_1 + m_2}\right)$. However, when studying objects on the atomic scale, a more realistic description must be formulated by quantum mechanics. Skipping over the detailed solution of the Schrödinger equation of the quantum harmonic oscillator, (see the specialized textbook for a detailed description [74, 35]) the energy associated to a quantum oscillator can be written as reported in equation 3.6

$$E_n = \left(n + \frac{1}{2}\right)h\omega \tag{3.6}$$

where n correspond to the vibrational quantum number. It is evident that, contrary to the classical description, the energy at the fundamental level (n=0) is not equal to zero: this important feature

is known as zero-point energy, meaning that there is no system with zero vibrational energy, even when the system is in its ground state. The model can be refined given that the harmonic formulation of the potential poorly describes the systems under examination. In reality, especially for large vibrational levels, the potential is better described by an anharmonic form, providing a much more realistic description of the vibration of a molecule. One of the issues with the parabolic model is that it does not account for the possibility of chemical bond dissociation at high values of n. The most considered correction to the harmonic model is the Morse potential, an empirical function whose analytical form is reported in equation 3.7

$$U_{Morse} = D_{eq}[1 - e^{\alpha(r_{eq}-r)}]^2 \tag{3.7}$$

where α is a constant of a specific molecule and D_{eq}, the depth of potentiall well, is the dissociation energy. Introducing the Morse potential into the Schrödinger equation significantly complicates the solution, to the point that resorting to numerical methods or variational strategies becomes necessary.

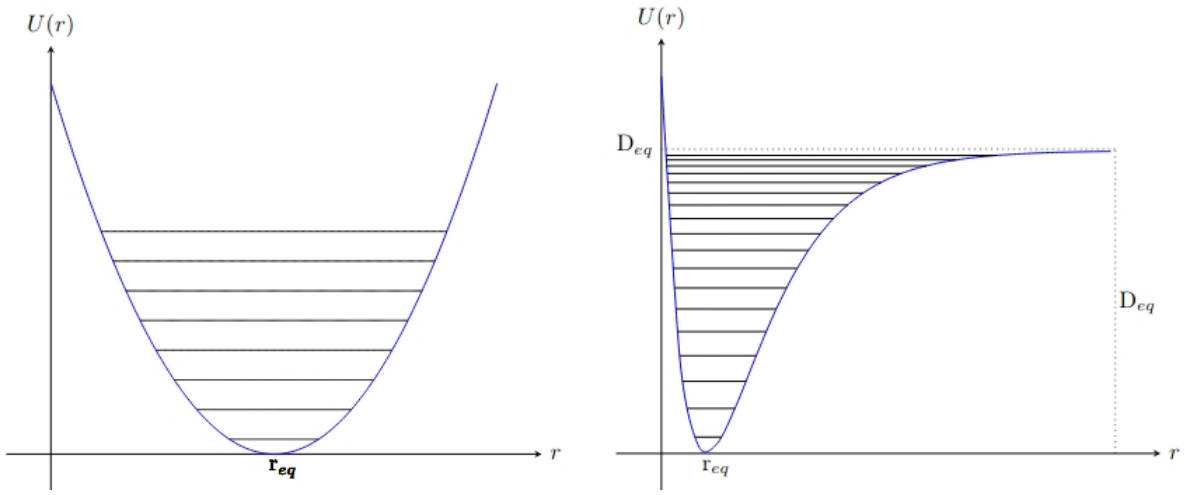

Figure 3.1: Comparison between the harmonic potential (left) and the Morse potential (right): the black lines correspond to the vibrational levels

As observable in figure 3.1, two evident differences emerge between the two potential forms.

The first concerns the form of the functional: the depth of the curve, denoted as D_{eq}, corresponds to the dissociation energy of the molecule. This implies that as the molecule vibrates at high frequencies (with a high vibrational number) it tends toward dissociation. The second important difference is visible observing the distances between the vibrational levels: in the case of the harmonic potential the level are equally spaced, while in the Morse potential they tend to converge (the energy difference is reduced) at high ν values. In other words for the low values of ν the harmonic and anharmonic potential are essentially equivalent. In both cases, the solution of the Schrödinger equation leads to formulate the first selection rule of the infrared spectroscopy. The selection rules in spectroscopy is a set of criteria that determines whether a particular transitions between two energy states is allowed or forbidden. These rules are based on conservation laws and symmetry considerations. For the simpler case (harmonic approximation) it can be written as:

$$\Delta\nu = \pm 1 \tag{3.8}$$

In the case of the anharmonic oscillator the selection rule formulated in equation 3.8 is partially modified, since we can also consider possible transitions involving non-adjacent vibrational levels ($0 \rightarrow 2$, $0 \rightarrow 3$, etc.). This statement is evident, as the vibrational levels are not perfectly equidistant and the molecules are able of absorbing photons at different energies.

$$\Delta\nu = \pm 1, \pm 2, \pm 3 \tag{3.9}$$

Skipping over the formal mathematical demonstration [75], the population of each level can be calculated by the Boltzmann distribution: this leads to predict the intensity of the bands associated to each transitions.

- Large intensity: $0 \rightarrow 1$, $\Delta\nu = \pm 1$
- Small intensity: $0 \rightarrow 2$, $\Delta\nu = \pm 2$
- Negligible intensity: $0 \rightarrow 3$, $\Delta\nu = \pm 3$

$\Delta\nu$ =1 originates the fundamental transitions while the others ($\Delta\nu$= 2, 3) are known as first and second overtones, respectively. The second selection rule of IR spectroscopy states that a transition is IR-active if and only if there is a change in the molecular dipole moment and can be rationalized as:

$$\Delta\mu \neq 0 \tag{3.10}$$

This selection rule derives from the quantum mechanically description of the molecular system:

$$\langle\Psi|\,\hat{\mu}\,|\Psi\rangle \neq 0 \tag{3.11}$$

where $\hat{\mu}$ is the dipole operator and Ψ the wavefunction associated to the molecular system.

The model so far described could be further refined introducing the terms associated to the rotational coupling. However, for a comprehensive understanding of the theory related to this effect, references should be made to specialized texts [75].

3.1.2 Molecular infrared spectroscopy

Vibrational molecular spectroscopy is a powerful tool for probing the structural properties of matter. In particular, infrared spectroscopy is widely used to investigate molecular structures at various level (intermolecular contacts, secondary interactions, in addition to its more traditional role in molecular recognition). Each functional group exhibits a distinct and well-known vibrational frequency, corresponding to a distinct peak with a specific shape in the IR spectrum. It is also widely known that the vibrational frequencies are influenced by the other substituent present in the molecule (intramolecular effects) or through coordination with other molecules (intermolecular effect): both effects manifests through the shift of spectral lines. The number of lines depends essentially on the molecular structure, the molecular symmetry and the presence of possible overtones and combination bands. For a molecule containing N-atoms, 3N geometrical coordinates are identifiable since the molecule can move in a 3N-dimension space. Considering the mechanical constrains generated by the presence of the intramolecular bonds, the number of

the degrees of freedom is reduced to 3N-6 for the non linear molecules and 3N-5 for the linear ones. The typical vibrational movement of the molecule consist in the stretching of the bonds and in the deformation of the angles (bending) and both can be symmetric or asymmetric.

3.1.3 Fourier Transform Infrared spectroscopy (FT-IR)

The modern procedure to perform infrared spectroscopy measurements is recurring to the Fourier Transform Infrared (FT-IR) spectrometers. In contrast to older grating spectrometers, the most important part of a FT-IR is the Michelson interferometer. In figure 3.2 a general scheme illustrating the operation principles of a Michelson interferometer is provided. The light coming from the source encounters the beamsplitter, where it is divided into two paths: a transmitted and a reflected part. The transmitted one impacts on a fixed mirror placed at a distance D from the beamsplitter and is back-reflected towards the beamsplitter. The reflected one reaches the mobile mirror and is back-reflected. The two beams are originated by the same source and are, therefore, coherent; when two beams recombine at the beamsplitter, interference occurs between the waves, which now present an optical path difference. The recombined beam is then sent to a detector that measures the intensity as a function of the displacement of the mobile mirror, creating an interferogram. The advantages of FT-IR spectroscopy over dispersive spectroscopy are numerous: among these, it is certainly worth emphasizing that operating in Fourier transform allows for a high spectral resolution and fast data acquisition, in addition to being more sensitive.

The signal is discretely sampled in N points. The spectra is obtained from the Fourier transform of the interferogram and is again discrete. The discrete Fourier transform gives rise to a N-point spectrum, where the first N/2 points compose the attended spectra and the other ones compose the specular image of the spectrum. This phenomenon is known as aliasing, which essentially consists of a peculiarity of the numerical processing of signals, stemming from the inherently discrete nature of the signal sampling and the Fourier transform used to generate the spectrum. The maximum frequency ν_{max} measurable with a FT-IR spectrometer is a consequence of the

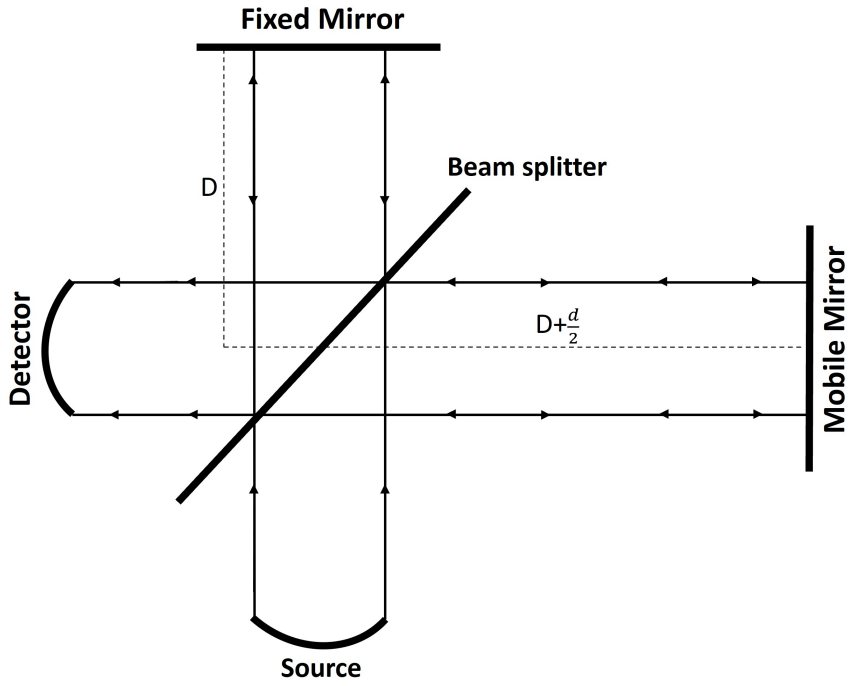

Figure 3.2: General scheme of the Michelson interferometer

aliasing and can be expressed with the following mathematical relationship:

$$\nu_{max} = \frac{1}{2\Delta x} \tag{3.12}$$

where Δx is the displacement of the mobile mirror. In the event of spectral components lying beyond the designated range, they undergo symmetrical reflection around ν_{max}. Hence it is important to employ light radiation exhibiting negligible components beyond the intended spectral range for measurement. This achievement is realized through the proper modulation of filters, beamsplitters and light-sources. As stated in equation 3.12, the maximum measurable frequency is contingent on the sampling range size, Δx, and is established by analyzing the interference fringes of a laser beam, usually a He-Ne laser, traveling along the same optical path used to monitor the movement of the mobile mirror, alongside the radiation emanating from the source. In the IR interferogram a data point is captured at every interference peak of the laser radiation,

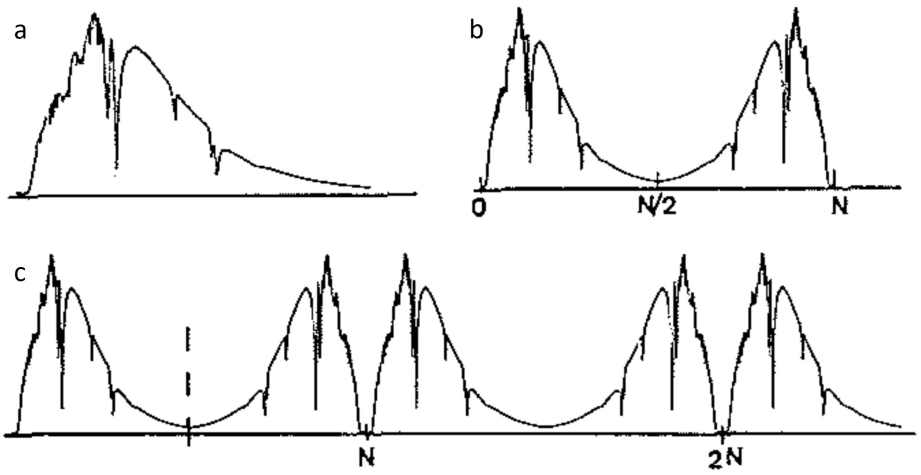

Figure 3.3: Effect of the discrete Fourier transform: (a) expected spectral shape; (b) spectrum and mirror image; (c) effect of aliasing

resulting in a sampling interval equal to twice of the laser wavelength. Since the wavelength of the He-Ne laser is equal to 632.8 nm ($6.328 \cdot 10^{-5}$ cm) the ν_{max} measurable is:

$$0 \leq \nu_{max} \leq \frac{1}{2\Delta x} = 7899 cm^{-1} \tag{3.13}$$

Another problem connected to the use of discrete Fourier transform can arise from the truncation of the interferogram: the signals are in fact measured in a wide range of optical paths. Furthermore, in the interferogram, there are additional maxima apart from the main maximum. To address these issues the signals are corrected multiplying the interferogram with apodization functions, which can have various analytical forms (rectangular, triangular, etc.)[76].

3.1.3.1 Optical material used in the IR measurements

As briefly mentioned in the precedent paragraphs an IR spectrometer comprises several optical components that must be transparent or reflective to infrared radiation: a crucial part of the instrument that requires transparency is the sample holder. Depending on the physical state of the sample, many experimental strategies can be adopted. The measurement performed in this

thesis were conducted mainly on liquid and solid systems. Liquid samples were measured putting a drop between two optical windows (thin liquid film between two optical windows) while, for the solid ones, dissolving the powder in transparent material (KBr and polyethylene). The material chosen primarily depends on the spectral region one aims to measure because the transparency range varies among different materials. In table 3.1 the principal optical materials applied in infrared spectroscopy are reported with their spectral region.The spectra acquired for this thesis were measured with optical diamond windows for liquid samples in both FIR and MIR spectral regions and with KBr and Polyethylene (PE) for solid ones, in MIR and FIR regions, respectively.

Table 3.1: Principal transparent materials commonly used in infrared spectroscopy

Material	**Wavenumber range (cm^{-1})**	**Spectral zone**
Potassium bromide (KBr)	250-47000	MIR-UV
Polyethylene (PE)	10-700	FIR
Diamond produced by CVD	5-45000	FIR-UV

3.1.4 Synchrotron radiation

The most commonly used light sources for infrared spectroscopy consist of Nernst filament incandescent lamps (composed of Zr, Y, and Th oxides), Globar bulbs (made of SiC), or quartz lamps. In addition to these sources, which have the advantage of being usable directly in the laboratories, one can opt for synchrotron light, which proves to be much more efficient in terms of light quality, power and beam collimation. The use of this light source presents various advantages:

- white spectrum, composed of electromagnetic waves between far infrared and hard X-Ray spectral regions
- high brilliance
- extremely high collimation in the direction of particle flight

- linear polarization in the plane of the orbit and elliptical polarization outside: the elliptical component can be used for dichroism experiments

A synchrotron is a large circular particle accelerator which comprises a combination of linear (LINAC) and circular accelerators (booster). In principle the particles used in these facilities comprises positron and electrons, although electrons are notably easier to operate. The role of the LINAC is to pre-accelerate the electrons into an energy range spanning from MeV to GeV. At this point they can enter into the circular accelerator (booster) which provides them the proper energy to circulate in the storage ring, where the synchrotron light is produced. Some of the measurements conducted for this doctoral thesis were performed at SOLEIL synchrotron in France (Paris). The radiation is emitted by electrons with energy of about 2.75 GeV, which travel in a storage ring of 354 m of circumference. The LINAC at the SOLEIL facility is 16 meters long and is capable of accelerating electrons to approximately 100 MeV while the booster takes them to 2.75 GeV. When introduced in the accumulation ring the trajectories of the relativistic electrons are controlled by magnets (bending magnets and undulators). The modern facilities, in fact, employ the undulators to control the trajectory of the electrons, guiding them along sinusoidal or spiral paths with the aim of increasing the distance covered by the electrons. At each curvature the electrons loss energy. In the storage ring radiofrequency cavities are incorporated to impart a controlled impulse to the electrons during each orbit. This is required to mitigate any undesired energy losses due primarily to collisions with residual gas atoms, resonance effects and repulsive interactions between the electrons (Toushek effect, known as intra-beam scattering). These electrons traveling along a circular orbit undergo continuous centripetal acceleration, which tends to deflect their trajectory. According to the theory of relativity, an accelerated charge emits electromagnetic radiations. As a result, these electrons, in losing energy, emit highly collimated light, the so-called synchrotron light. The emission of radiation can be explained using classical physics formalism, but considering that the electrons move at a speed close to that of light, it becomes necessary to introduce relativistic effects. Considering that the electrons have electric charge e

and linear momentum p, the radius of curvature ρ can be calculated through the Lorentz force:

$$\rho = \frac{p}{Be} \tag{3.14}$$

where B is the magnetic field of the undulator. The energy associated to a particle moving at the speed of the light is:

$$E^2 = p^2 + c^2 + m^2 + c^4 \approx p^2 c^2 \tag{3.15}$$

where c is the speed of the light and m the rest mass of electron. Through manipulation of the equation 3.14, it can be derived that the radius of curvature of a relativistic particle can be calculated as:

$$\rho = \frac{E}{cBe} \tag{3.16}$$

In contrast to a conventional light bulb, which emits radiation in all directions, synchrotron light is emitted within a very narrow solid angle: this is the reason why it is feasible to achieve a highly focused beam of light. This phenomenon strongly depends on a relativistic effect. Skipping over the formal mathematical derivation it is possible to assert that the radiation is emitted in a cone with angle equal to:

$$\chi = \frac{2}{\gamma} \tag{3.17}$$

where χ is the angle between the direction of acceleration and propagation and γ is the Lorentz factor representing the relativistic speed of the electron. The emitted power is maximum in the direction orthogonal to the acceleration and zero in the parallel one. The mathematical form is reported in equation 3.18.

$$\gamma = \frac{1}{\sqrt{1 - \frac{v^2}{c^2}}} \tag{3.18}$$

and is approximately equal to 100 μrad. It should be noted that these equations are applicable when a reference system is chosen to be fixed with the electron. The light generated in the storage ring can be diverted and sent to the experimental lines, the beamlines, where it is used as light source to conduct scientific experimental. It appears quite obvious that to avoid undesired scattering phenomena between the relativistic electrons and the other particles (gas) present in the

accumulation ring, this compartment is constantly maintained in ultra-high-vacuum conditions (P=10^{-10}-10^{-11}mbar).

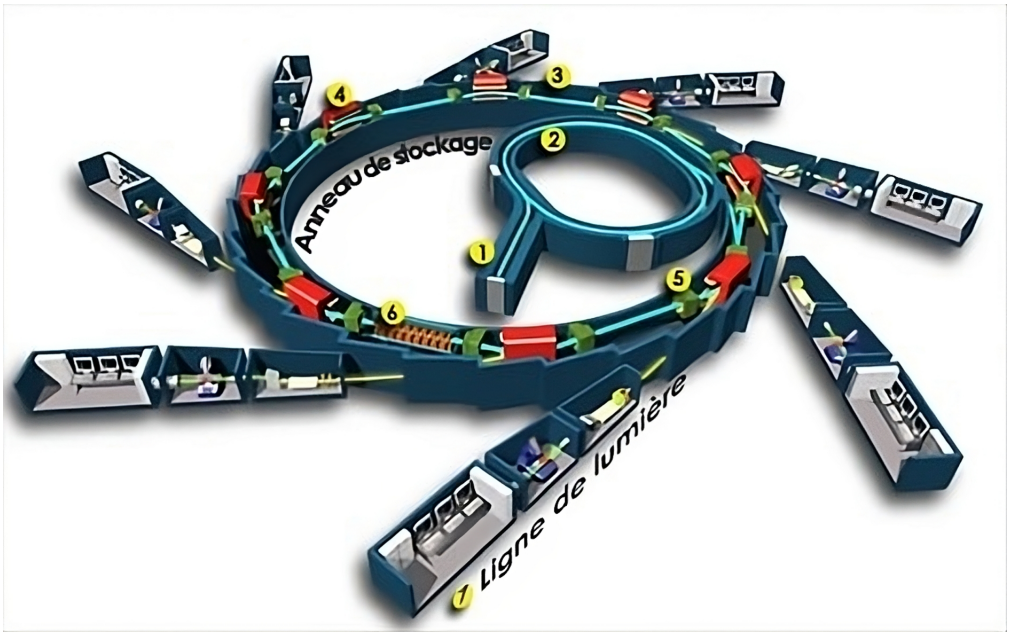

Figure 3.4: Scheme of SOLEIL synchrotron facility: 1) LINAC, 2) booster, 3) storage ring, 4,5,6) bending magnets and undulators, 7) beamlines

3.2 Thermal Analysis

Thermal analysis represents a powerful experimental approach employed to investigate how a material responds to temperatures variations. These methods holds particular significance across various scientific and technological branches. The most common techniques include differential scanning calorimetry (DSC) and thermogravimetry analysis (TGA).

3.2.1 Differential Scanning Calorimetry

Differential Scanning Calorimetry (DSC) is a thermal analysis method that measures the quantity of heat required to raise the temperature of a sample relative to a reference material, recorded as a function of temperature. The differential measurements are exceptionally valuable because the resulting thermogram can be analyzed with confidence that the observed thermal process are specific to the sample under examination, completely independent of the experimental conditions. This guarantees a high level of reproducibility in DSC experiments. Furthermore, unlike Differential Thermal Analysis (DTA), DSC enables the quantification of the thermal process (it is possible determine from the curves the amount of heat exchanged and deduce quantities such as enthalpy or specific heat of samples). The DSC curves reflects the energy variations of the studied materials, represented in characteristic signals in the DSC traces. It is possible to determine the temperature associated with various physical process such as melting, solidification, glass transitions, cold crystallization. Analysing the form of the peak is also possible to determine the degree of crystallinity and the level of purity of a specific material. An explanatory description of the operation of the instrument is reported in figure 3.5. From the scheme is possible to identify the two crucibles, one containing the sample and the other used as reference, usually empty. The furnace is equipped with several thermocouples that measure the temperature of samples and of reference, with the aim to regulate the heat flux, allowing a controlled heating or cooling of the sample and the reference. Furthermore there is a connection for the cooling system and an inlet for the purge gas (usually Ar, N_2 or another inert gas). Ideally a calorimeter can be imaging as an isolated thermodynamic system, with the sample and the surrounding environment exhibiting

variances of only few hundredths of a degree.

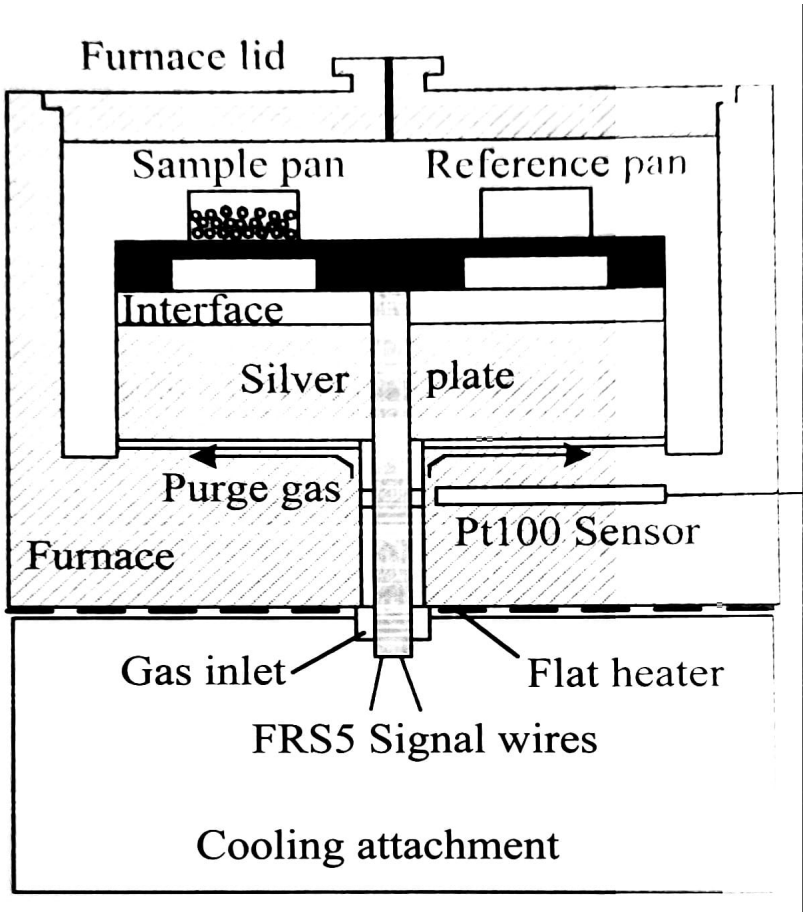

Figure 3.5: General scheme of a DSC furnace

From a thermodynamic standpoint the DSC trace can be explained taking into account the heat flow, $\frac{dQ}{dt}$, acting on sample and reference compartments, as reported in equation 3.19

$$\Delta\left(\frac{dQ}{dt}\right) = \left(\frac{dQ}{dt}\right)_S - \left(\frac{dQ}{dt}\right)_R = \left(\frac{dT}{dt}\right)\left[\left(\frac{dQ}{dT}\right)_S - \left(\frac{dQ}{dT}\right)_R\right] \tag{3.19}$$

where the subscripts S and R indicates respectively the sample and the reference. From equation 3.19 results evident that the term $\frac{dT}{dt}$ is a kinetic parameter linked to the scanning speed which can be indicated as $\beta = \frac{dT}{dt}$. According to classical thermodynamic the term $\frac{dQ}{dT}$ corresponds to the heat capacity, c_p. Taking into account these evidences, the equation 3.19 can be rewritten as:

$$\Delta\left(\frac{dQ}{dt}\right) = \beta\left(m_s c_{p,S} - m_r c_{p,R}\right) \tag{3.20}$$

where m_S and m_R are respectively the mass of sample and reference. The baseline of the thermogram is obtained considering the first term (terms with s subscripts) of the equation 3.20. When a process with variation of enthalpy occurs, a contribute reported in equation 3.21:

$$\left(\frac{dQ}{dt}\right) = \Delta H_p m_s \frac{d\alpha}{dt} = \beta\left(\Delta H_p m_s \frac{dQ}{dT}\right) \tag{3.21}$$

must be added to equation 3.20, where ΔH_p is the variation of enthalpy and α the degree of the advancements of the process. This provides the formal rationale for the sigmoidal shape of the thermal process curve, deviating from the baseline of the thermograms. Integrating the area under the peak allows for the determination of the enthalpy associated with the process. Based on the sign of the enthalpy, and consequently, the direction of the peak (upward or downward), it is possible to differentiate between endothermic and exothermic processes. The equations in this paragraph evidences the importance of the scan rate, as the dependence on β is evident. If the rate is too high, it can cause inaccurate estimations of transition temperatures or even produce curves that lacks transitions. Hence it is crucial to compare measured data from various samples using thermograms acquired with identical temperature rates and programs. In figure 3.6 the principal transitions observable in DSC experiments are reported, following the "exo up" convention, in which exothermic transitions are shown as peak pointing upwards. T_{trans}, T_c and T_m corresponds, respectively, to the temperature of solid-solid transitions, crystallization and

melting. T_g, on the other hand, is the glass transition temperature associated with a second-order phase transition, commonly observed when supercooling a viscous fluid.

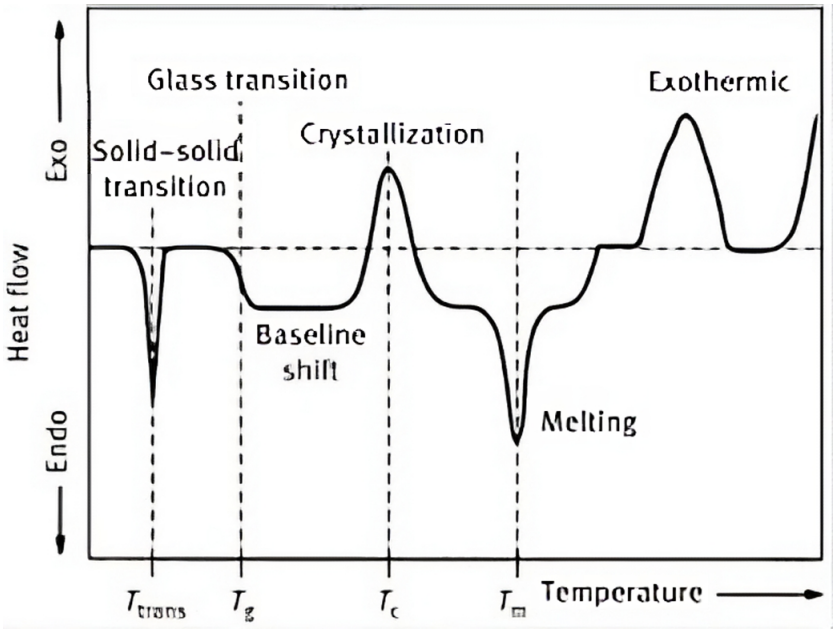

Figure 3.6: Principal transitions observed in DSC experiments

3.2.2 Thermogravimetry

Thermogravimetry (TGA) is a thermo-analytical technique used to investigate the thermal stability and the decomposition process of materials. TGA encompasses the concurrent measurement of variation in mass and temperature of a sample subjected to a controlled heating in an inert atmosphere. In many cases, in addition to mass and temperature, heat fluxes are concurrently measured. Similar to DSC, TGA is widely used in material sciences to thermally characterize the sample under examinations and they are often coupled. The core of a TGA instrument is composed by a furnace, two crucibles and an accurate balance. The furnace heats the sample placed in an inert crucible (the other is used as reference, with the aim to counterbalancing the mass on the balance rod and serving as a reference, as in DSC, for heat measurements). The balance records the

mass variation of the sample when heated according to a predefined temperature program. The instrument can also operate in isothermal condidition. Since many instrument can reach temperatures of about 1000-1550°C, the measurements are conducted under inert atmosphere, in order to avoid any oxidation process or reaction with atmospheric components. However, especially in the study of material oxidation, gases and mixtures can be introduced. Some instruments have the capability to operate under vacuum conditions. The experimental response of TGA consists of a thermogram with the variation of the mass (Δm) or its percentage on the y-axis and the temperature on the x-axis. In figure 3.7 the result of a generic TGA-DTA experiment: it is evident that all process involving phase changes of the system (glass transitions, solidification, melting) do not lead to a change in the mass of the sample (the TG curve is constant). The TG line starts to deviate when the thermal decomposition begins.

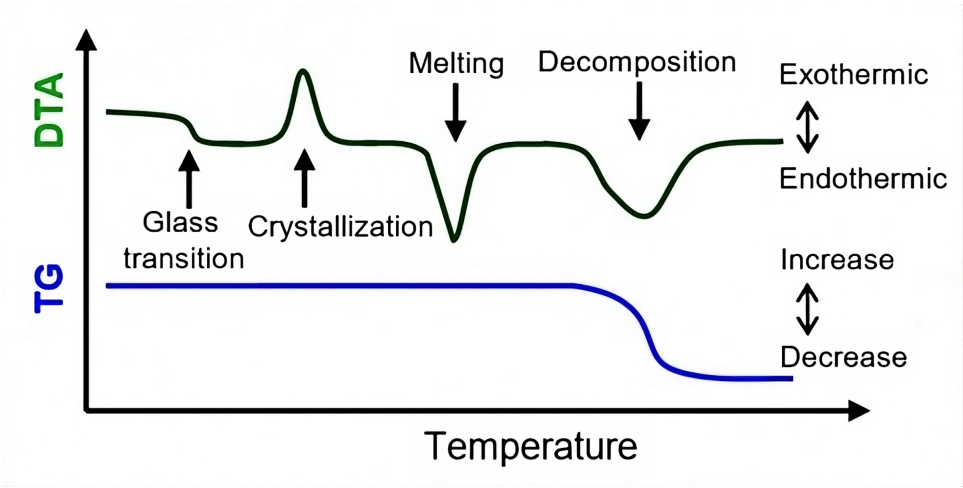

Figure 3.7: Comparison between DTA (black line) and TGA (blue line) curves

3.3 Experimental procedures applied in the study of the proposed systems

Sample preparation

The samples studied in this thesis were prepared using starting materials with a high degree of purity (≥98-99%). Each compound underwent vacuum drying for 8 hours before samples preparation. The mixtures were prepared by mixing the precursors according to the proper molar ratio through magnetic stirring for 4 hours at 70-80°C, achieving homogeneous liquid phases. The resulting mixtures were stored in dried glass vials. Prior to measurements, a vacuum treatment to remove traces of atmospheric moisture was performed; all samples were stored under inert atmosphere (Ar or N_2) and sealed with Parafilm.

Thermal Investigation

The thermal analysis was conducted both by means of differential scanning calorimetry (DSC) and thermogravimetry (TGA). DSC measurements were carried out using a DSC 3 Star System-Metter Toledo instrument equipped with a Huber TC100 Cryocooler. 10-20 mg of samples (mixtures or pure components) were put in a drilled aluminium crucible. The temperature rate was always 5°C/min, apart in the case of some phenol-mixtures, where it was necessary to use a rate of 0.6°C/min. The thermal stability was investigated by thermogravimetric analysis by means of a Setaram Setys Evolution 1200 TGA: measurements were conducted between room temperature and 850°C using rate of 10°C/min with an argon flux of 60 mL/min and initial masses of about 20 mg.

Vibrational spectroscopy

Infrared spectra were acquired both in the far (FIR) and medium (MIR) infrared regions. In the far infrared range, we used the IFS125 spectrometer (Bruker, Billerica, MA, USA) of the AILES beamline of Soleil Synchrotron with a Mylar beamsplitter and a bolometer as detector. In the MIR region we used an Agilent 660 spectrometer equipped with a DTGS detector, a KBr beamsplitter and a Specac Variable Temperature cell. For both configurations, the sample was placed in a vacuum tight cell for liquids equipped with diamond optical windows, in order to avoid contamination from air or moisture. The spectral resolution was fixed to 1 cm^{-1} for both spectrometers. The liquid samples were measured putting the liquid between two diamond optical windows. The solid materials was measured dissolving the powder in KBr (MIR) or polyethylene (FIR) in a ratio of about 1:100. Some samples were measured using a FT-IR Spectrum Two by Perkin Elmer spectrometer in Attenuated Total Reflection (ATR) mode. Raman spectra were measured using a LABRAM confocal-microscope spectrometer by HORIBA Jobin Yvon equipped with a He-Ne gas gas laser (λ = 632nm) operating at 10mW power with a 20X optical microscope.

Chapter 4

Structural characterization of Deep Eutectic Solvents

In this chapter we reported the principal results obtained in the characterization of deep eutectic solvents; we studied, by a combined experimental and theoretical approach, two ”type III” and one ”type V” examples of deep eutectic solvents.

4.1 Choline chloride-Imidazole and Tetrabutylammonium bromide-Imidazole

The structures of two deep eutectic solvents where imidazole, IM, (H-bond donor) is coupled with either choline cloride, ChCl, or tetrabutylammonium bromide, TBABr, (H-bond acceptors) were studied by infrared and Raman spectroscopy and X-ray diffraction. The microscopic distribution of the components in both liquids was investigated by DFT level (M062X/6-311G**) calculations and molecular dynamics simulations (GAFF FF).

DSC results

The phase diagram of both systems was previously studied by Hou and coworkers in 2008 [77]: they found the eutectic point at 7:3 molar ratio (7 parts of imidazole and 3 parts of quaternary ammonium salts, ChCl or TBABr). We measured the DSC curves of both eutectic mixtures and observed the melting transitions at 26°C and 56°C for TBABr-IM and ChCl-IM, respectively. The curve on heating of TBABr-IM shows a glass transitions at -50°C and a cold crystallization around 0°C, immediately followed by the melting.

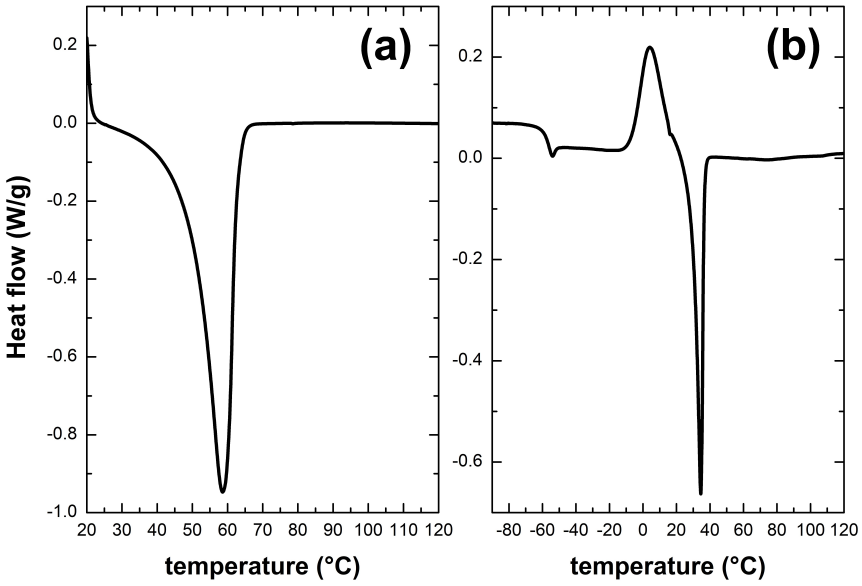

Figure 4.1: DSC curves of ChCl-IM (a) and TBABr-IM (b).

Quantum chemical modelling

The molecular arrangements of the components of both DESs were preliminary investigated by vibrational spectroscopies (MIR and Raman), measuring the spectra of pure components and their mixtures and simulating their vibrational spectra by DFT calculations. Imidazole has a crystal structure where the molecules are interconnected by endless chains through strong N$\cdots$HN hy-

drogen bonds[78], as observed in previous works[79, 80, 81]. With the aim to simulate a plausible structure of pure solid imidazole, we decided to optimize a cyclic trimer where each NH group is interconnected with hydrogen bonds to N atom of another molecule of IM. In ChCl and TBABr we expect anions strongly connected to cations, as already observed in many studies. The structures reported in figure 4.2 are therefore representative of the molecular arrangements in the pure components.

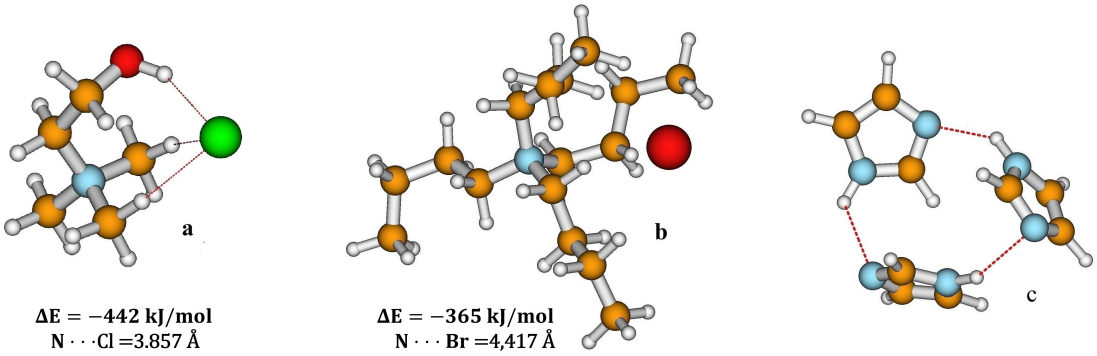

Figure 4.2: ChCl ion pair (a), TBABr ion pair (b) and imidazole trimer (c) optimized at the M062X/6-311G** level. ΔE is the interaction energy between cation and anion.

Our simplest representation of ChCl is an ion pair: the most stable structure shows the coordination of the chloride anion through OH$\cdots$Cl hydrogen bond and two CH$\cdots$Br interactions. This result agrees with the structure of ChCl determined at different levels of theory in previous studies [82, 83]. Ion coupling is substantially different for TBABr: the cation is larger, more flexible and has not OH groups and therefore interaction with the Br anion involves only electrostatic terms and specific CH$\cdots$Cl interactions of the alkyl chains. The binding energy (-365 kJ/mol) is lower than that of ChCl (-442 kJ/mol). Simple models to simulate the local interactions between different components in the mixture at 1:1 molar ratio are the complexes of Fig. 4.3. The optimized structures show a strong tendency of imidazole to interact with bromide or chloride ions, forming NH$\cdots$Br and NH$\cdots$Cl hydrogen bonds. The interaction energy between IM and the ion pairs was assessed by computing difference between the total energy of the complex and the

sum of the energies of imidazole and the corresponding ion pair with halide. The binding energy was corrected for the Basis Set Superposition Error (BSSE) by the Boys and Bernardi cointerpoise method [84], which consist in a correction applied in QM calculations to account for the over-counting of electron-electron interactions when separate basis sets are used for different parts of a molecular system, such as in the calculation of interactions energies between two or more fragments. The corrected binfing energies and the coordination geometry suggest that cations and anions continue to be coupled also in presence of imidazole. We therefore expect local structures in the mixtures where halide coordinates imidazole molecules and cations simultaneously. To be honest, these result appears quite straightforward when 1:1 complexes are considered.

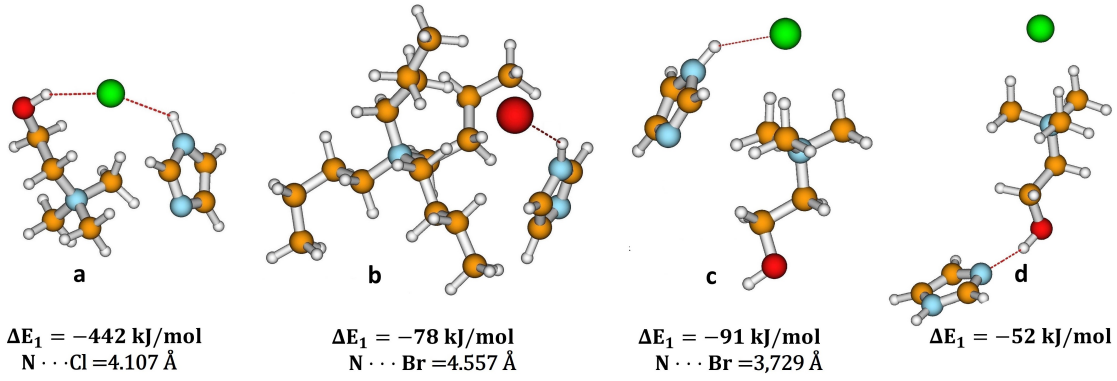

Figure 4.3: ChCl-imidazole complexes (a,c,d) and TBABr-complex (b) optimized at the M062X/6-311G** level. ΔE_1 is the interaction energy between imidazole and ion pair calculated as E(complex) -[E(imidazole)+E(ion pair)]

As a matter of fact both mixtures exhibit an eutectic composition at 7:3 molar ratio. For a more realistic modelization of our mixtures. a larger complex was furthermore examined comprising three ChCl ion couples and seven imidazole rings. The geometry and the vibrational frequencies were computed at M062X/6-31G* level of theory and its structure is reported in figure 4.4. Given the complexity and the high number of degree of freedom, we cannot be sure whether we are describing the global minimum over the potential energy surface of this complex. Nevertheless, some characteristics of this structure may offer insights into potential interactions between com-

ponents in the mixtures. As for the 1:1 complexes, imidazole may again interact with the chloride anion; however we cannot exclude OH$\cdots$N hydrogen bonding between choline and imidazole as well as NH$\cdots$N bonds between imidazole molecules. The model here proposed is still too small to reproduce all the possible coordination sites.

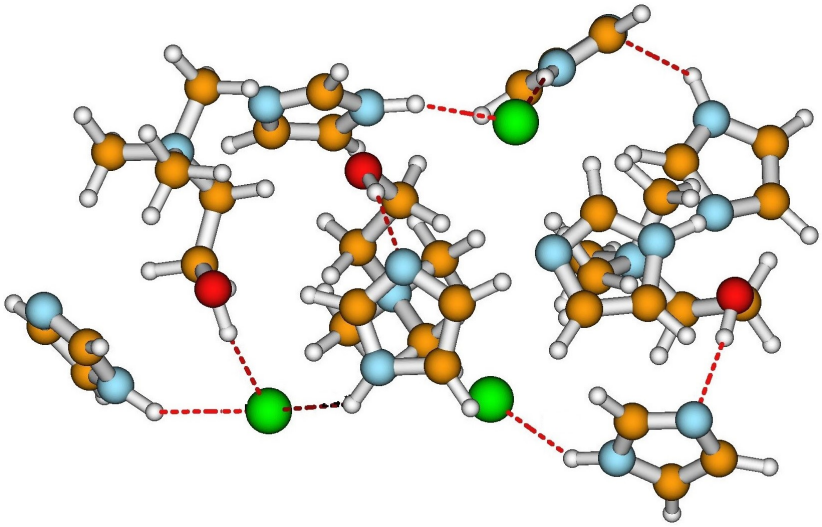

Figure 4.4: ChCl-imidazole (3:7) complex optimized at the M062X-6-31G* level.

Spectroscopic results

The vibrational spectra (IR and Raman) were measured to investigate the intermolecular contacts in the pure components and in the mixtures. From a direct comparison between the spectra of pure components and mixtures we noted only slight spectral shifts that can be attributed to various factors; the most significant one is the different physical state of the compared samples. All spectra were measured at room temperature: in the case of TBABr-IM DES, the pure components are solid while the mixture is liquid. It is widely known that the positions and the shapes of vibrational bands are strongly dependent on the physical state of the sample. In the case of solids, particularly those with a crystalline structure and high molecular order, bands appear narrower and more defined. Conversely, in liquid, the bands tend to be broader [85, 86]. The comparison

between the experimental IR spectra of ChCl, IM and ChCl-IM is reported in fig. (4.5) and the assigment of the main bands were conducted combining the theoretical results with previous studies.

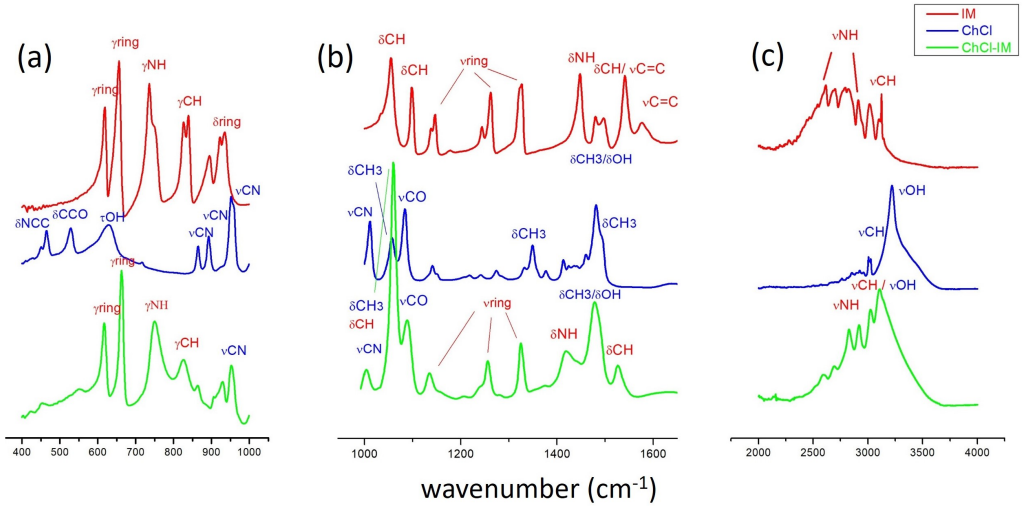

Figure 4.5: Experimental IR spectra for IM (red), ChCl (blue) and mixture (green). ν = stretching, δ = in plane bending, ρ = rocking, γ = out of plane bending

The spectral pattern of imidazole in the high frequencies region results complex, showing a multiplet at about 3000 cm^{-1}, which comprises two ν_{CH} and multiple characteristic bands of ν_{NH}, similar to those generally seen for NH groups that are strongly engaged in hydrogen bonding [87, 88, 89]. Regarding the ChCl spectrum it is evident that it is largely dominated by the signal of ν_{OH}. In the spectrum of the mixture, ν_{OH} results partially overlapped with the ν_{CH} of imidazole and the OH stretching is not drastically perturbed by the coordination: the shape and position of the spectral lines suggest that the coordination with cation and anion continues to be coupled in the mixture as it was in pure ChCl. The assignment of the bands in the other spectral zones resulted straightforward: the provided description of the normal modes is approximated, as these vibrations are mixed for each molecules. These bands appear however substantially unaltered in the mixture, compared to the pure components. Some slight shifts were observed for δ_{NH} and γ_{NH} and for δ_{OH} and ν_{C-O} of ChCl, suggesting that the coordination involves OH and NH groups. In the TBABr-IM mixture we observed some changes only in the high frequency region, where the absorption bands of the NH (imidazole) seems to be shifted between red and green curves (figure 4.6). The other main band remains almost unchanged, except for those concerning the vibrations of the NH group of imidazole, where small shifts are observed. The Raman spectra show essentially the same results of IR ones: we have not observed significant lines shifts between pure components and mixtures, with the exception of δ_{NH} vibrations, that appear again slight changed in the mixtures. Both techniques show that for both the mixtures imidazole interacts through NH group. For choline chloride it is instead quite hard to appreciate changes in the OH vibration since this absorption overlaps with other bands.

X-ray and MD simulation

The structure of both eutectic mixtures were characterized experimentally by X-Ray diffraction. The structure functions q·I(q) obtained from experiment were compared with the theoretical curves derived from MD simulations as reported in figure 4.8. The analytical form of I(q) is reported in equation 2.42, where q is defined as scattering variable. X-ray diffraction measurements

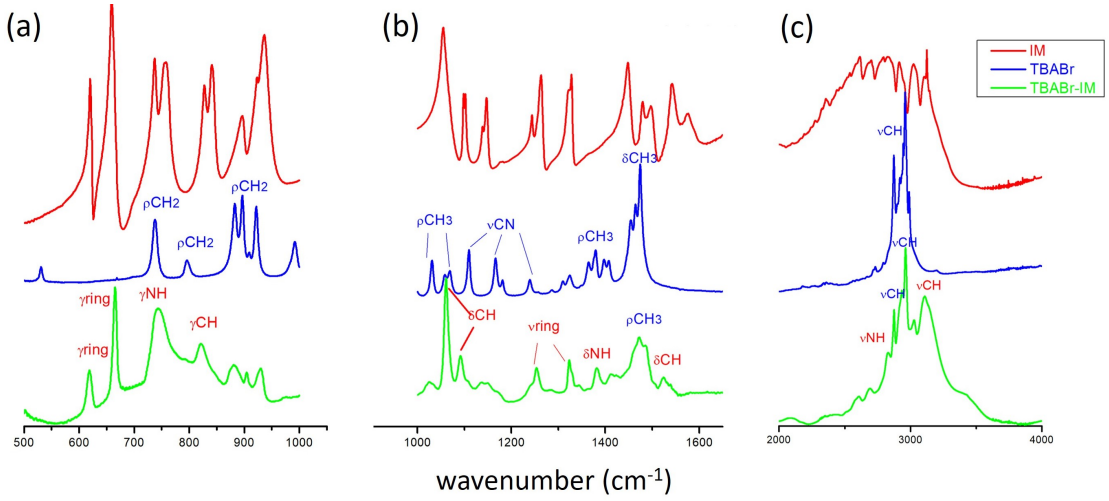

Figure 4.6: Experimental IR spectra for IM (red), TBABr (blue) and mixture (green). The assignation of lines for IM is reported in figure 4.5

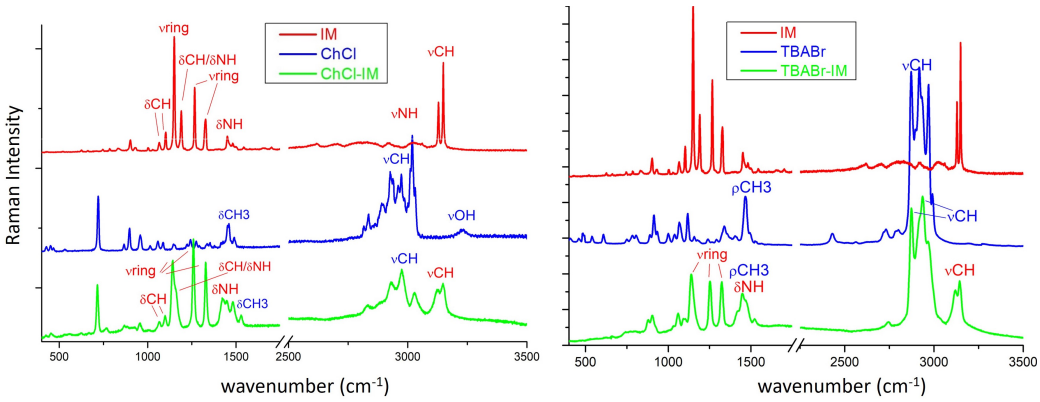

Figure 4.7: Experimental Raman spectra: ChCl-IM and pure components (left) and TBABr-IM and pure components (right)

on liquids allow to determine from an experimental standpoint the spatial organization which the components assume in the bulk liquid. The I(q) function, defined in the q domain, is in fact strictly connected with the radial distribution function, g(r), defined in the distance domain, through a Fourier transform relationship. It should also be noted that a relation approximately links the

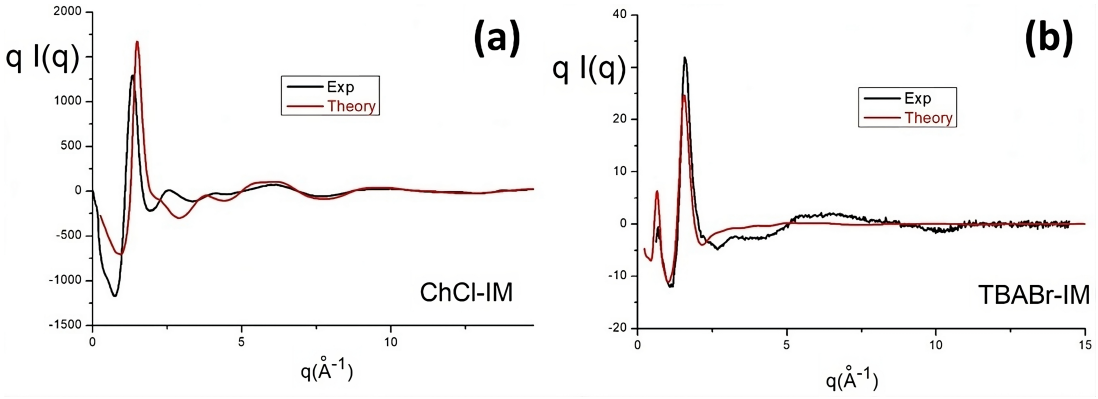

Figure 4.8: Theoretical and computational structure functions q·I(q) of ChCl-IM (a) and TBABr-IM (b)

q-domain to r-domain:

$$q \approx \frac{2\pi}{r} \tag{4.1}$$

More detailed descriptions of the X-ray diffraction and I(q) function can be found in specialized texts[55]. The curves of ChCl-IM and TBABr-IM reproduced in figure 4.8 appear noticeably different. Both systems are characterized by the presence of the main peak at about 1.5$\mathring{A}^{-1}$ which correlates with distances at about 4$\mathring{A}$: this pattern was found in several liquid systems (ILs and DESs) and is due to intermolecular interactions that in our cases can induce an alternating pattern of cations and anions in the liquid. The experimental curve of ChCl-IM shows another weaker peak at about 2.5$\mathring{A}^{-1}$ which correlates with a distance in the direct space of about 2.5$\mathring{A}$ and can be assigned to intermolecular contacts and is in agreement with the values of the O$\cdots$Cl and N(H)$\cdots$Cl predicted by our models. Some inconsistencies appear instead in the region of low q due to an overestimated strength of hydrogen bonding between cations and anions and to the small accuracy of the GAFF force field employed in our simulations. In addition the procedure of analysis of the experimental data to extract the I(q) curve requires the knowledge of the density of the mixtures. Since ChCl-IM is solid at room temperature, its density was estimated only as a weighted average of the values of the pure components, ChCl and IM. The diffraction curve of

TBABr-IM in figure 4.8 shows an additional peak measured at q values lower then 1 $\mathring{A}^{-1}$ (about 0.65$\mathring{A}^{-1}$). Many works discussed the nature of the pre-peaks and most of them attributed the peak to the formation of a medium range order due to the segregation of butyl tails of TBA in the bulk liquids. Although our model clearly overestimates the intensity of this peaks, we observed a correct prediction of its q-value. With the aim to strengthen our interpretation, the theoretical I(q) was divided into partial contributes (anion, aliphatic chains and imidazole, each of them computed for intramolecular and intermolecular contributions), as shown in figure 4.9. We observe that the pre-peak is influenced by the presence of intermolecular components within the alkyl terms, while the intramolecular ones remains inactive in the same low q values region. Moreover, the intermolecular factor of the the alkyl partial I(q) contributes also in the region of the main peak. Furthermore, the pre-peak is influenced by both the alkyl terms and interactions among anions, as well as the intermolecular characteristics of imidazole. These assumptions results compatible with the hypothesis of the existence of an alternating pattern of components in the liquid bulk.

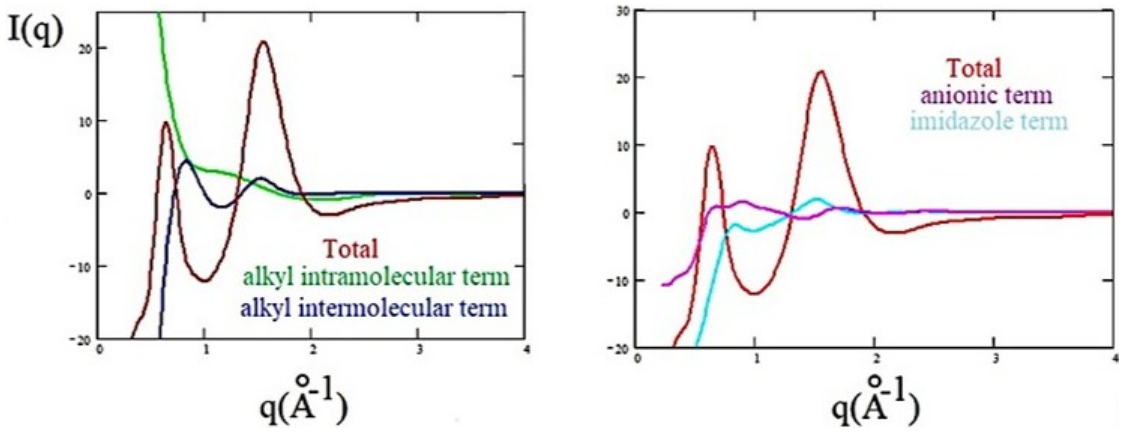

Figure 4.9: Partial structure function for TBABr-IM: comparison between the total I(q) (red) and alkyl intramolecular term (green), alkyl intermolecular term (blue), anionic-anionic term (magenta) and imidazole term (cyan)

Molecular dynamics analysis

In addition to the theoretical I(q), the analysis of the molecular dynamics trajectories has also allowed for a more detailed investigation of the morphology of the bulk phase of the liquids. The intermolecular contacts were investigated computing some characteristic pair radial distribution function, g(r). The significant structural differences between the two cations influence the structural configurations within the ionic pairs. Choline cation is an asymmetric quaternary ammonium cation with an hydroxyl substituent, while TBA is larger and more symmetrical than Ch, with four equivalent butyl chain; therefore, we do not aspect any preferential interaction site in TBA. In figure 4.10a we reported the pair radial distribution functions computed between choline and chloride ($Cl\cdots H(O)$, $Cl\cdots N$ and $Cl\cdots O$) to investigate how the ion couple is arranged in presence of imidazole. The reported g(r)s reveal that the OH group of choline coordinates the chloride anion through sharp $Cl\cdots H(O)$ hydrogen bonds, as predicted by DFT calculations. The weak peak around 4Å in g(r) of $N\cdots Cl$ distance suggests that the coordination marginally regards the polar heads of choline. Moreover, the coordination of the OH group with the chloride anion excludes any interaction with imidazole since the RDF of the $(O)H\cdots N$ intermolecular distance does not show peaks at values below 4Å. Figure 4.10b shows the RDF of the $Br\cdots N(TBA)$ distance: the most intense signal is the sharp peak at about 4.8Å in agreement with a marked localization of the bromide anion at distances close to that predicted for the ion pair optimized at DFT level of theory. Imidazole is an aromatic heterocycle with two different interaction sites: NH can behave as hydrogen bond donor while N as acceptor. The RDFs reported in figure 4.10c show a strong tendency exhibited by imidazole to establish hydrogen bonding with Br and Cl. The arrangement of chloride or bromide anions in relation to cations and imidazole was observed through the spatial distribution functions depicted in figure 4.11. Figures 4.11a and 4.11b demonstrate that the anions are tightly clustered around the H(N) group of imidazole in both liquids. The distribution of bromide exhibits a considerable symmetry in relation to the TBA cation (figure 4.11c), while chloride is predominantly concentrated around the OH group of the choline cation (figure 4.11d).

Summarizing all the result obtained from this study we can conclude that imidazole shows a pronounced tendency to form hydrogen bond coordinating the anions. Both cations, although with different sites (hydroxyl in choline and butyl chains in TBA) are linked to the anions. These liquids exhibit a high degree of structuring, attributed to the presence of a dense network of hydrogen bonds formed between their constituents. The vibrational spectra of the pure components and their mixtures, although not displaying pronounced shifts, yield important insights into the nature of interactions involved in the liquid phase formation. Notably, shift are discernible in the NH vibration bands of imidazole. This observation strongly supports the hypothesis that imidazole can act as a hydrogen bond donor, a conclusion subsequently reinforced by our calculations. Both ion couples, indeed, are capable of accepting the hydrogen bonds, exploiting their anion. A bridge-like structure is consequently formed, wherein the anion occupies the central position, coordinating both the cation and the imidazole. Furthemore, this arrangement leads to the formation of an alternating structure in the liquid phase, as confirmed by X-ray measurements. The results obtained sparked an interest in investigating deeper into the analysis of the roles that HBD and HBA have in the formation of DES. The chemical structure and size of an anion can influence its capacity to accept hydrogen bonds, while the chemical nature of a hydrogen bond donor (e.g., alcohol, carboxylic acid, aromatic NH) certainly modifies its ability to behave as HBD. For these reasons we proposed other systems, composed by Tetrabutylammonium Acetate (TBAAc) and Choline Acetate (ChAc) and three different natural organic acids, namely Ascorbic acid (AA), Citric acid (CA) and Maleic acid (MA). Fixing the nature of the cation, we select organic acids with different size and different HB donor groups with the aim to modulate the strenght of hydrogen bonding.

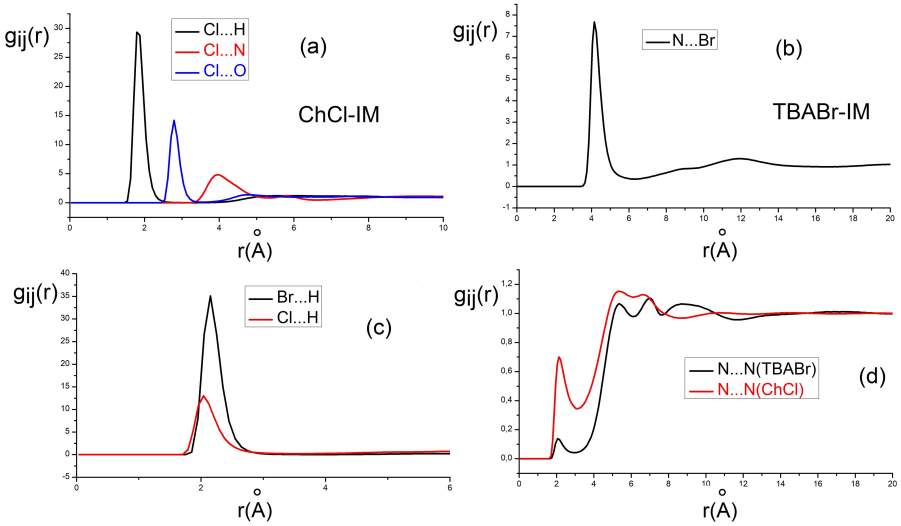

Figure 4.10: RDFs computed for ChCl-IM. (a) Distances between Cl and H, N, O atoms of choline. (b) Distances between N of TBA and Br. (c) Distances between Br···H(imidazole) and Cl···H(imidazole). (d) Distances between imidazole rings in TBABr-Im (black) and ChCl (red)

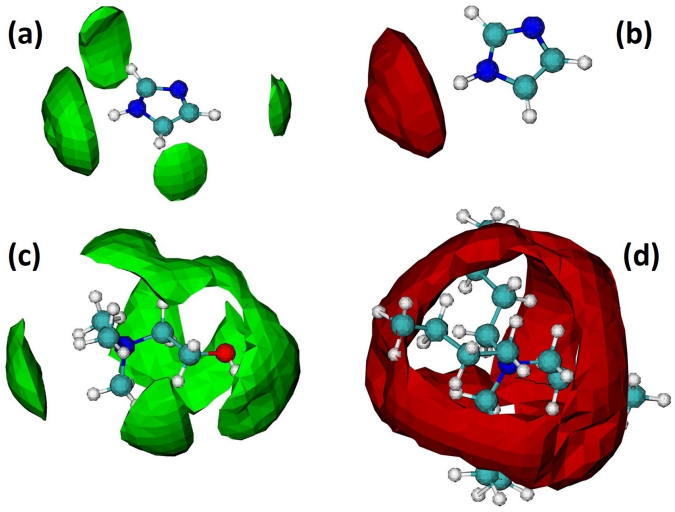

Figure 4.11: Spatial distribution functions of Cl with respect to imidazole (a) and choline (c) and Br with respect to imidazole (b) and TBA (d)

4.2 Choline acetate and Tetrabutylammonium acetate-Natural organic acids

The thermal and structural characterization of these natural organic acid based systems were carried out by considering two different variables, namely the typology of acid and its concentration in the mixture. The three acids here studied have OH groups with different acid properties and they are therefore HBDs of different strength. Varying the nature of acid and its concentration in the mixture can be therefore a valid procedure to analyse how the properties and the structure of the liquid are affected by the strength of intermolecular hydrogen bonding. In detail, we investigated mixtures with L-ascorbic acid (AA), citric acid (CA) and maleic acid (MA). In particular,

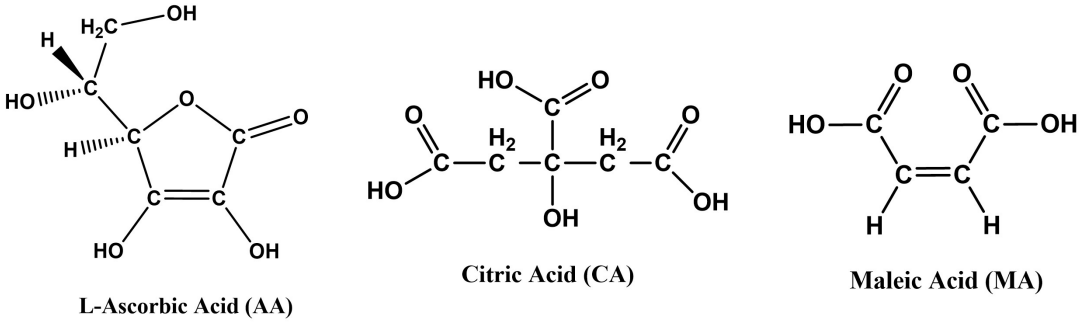

Figure 4.12: Molecular sketch of L-ascorbic acid, citric acid and maleic acid

AA is the only one that has no carboxylic function and contains three distinct hydroxyl groups; maleic and citric acids are substituted with two and three carboxylic substituents, respectively. Additionally, CA possesses an extra hydroxyl group. Following the definition of hydrogen bonds established by the International Union of Pure and Applied Chemistry (IUPAC) in 2011[90], it is plausible to draw a correlation between the strength of the hydrogen bond and the acidic property of the components (pKa and pKb). Several mixtures were obtained by mixing one of the two acetate samples with each acid at different molar ratios: the obtained samples (choline acetate based systems), their molar ratios and labels are reported in table 4.1. TBAAc-based systems were labeled analogously.

Table 4.1: Labels and molar ratios of the studied samples

Acetate	Acid	Molar ratio acetate:acid	Sample Label
ChAc	Maleic	2:1	ChAc-MA 2-1
		1:1	ChAc-MA 1-1
		1:2	ChAc-MA 1-2
	Ascorbic	2:1	ChAc-AA 2-1
		1:1	ChAc-AA 1-1
		1:2	ChAc-AA 1-2
	Citric	2:1	ChAc-CA 2-1
		1:1	ChAc-CA 1-1
		1:2	ChAc-CA 1-2

Thermal analysis results

Figure 4.13 shows the thermal behaviour of the pure components (ChAc and acids) and their mixtures. While for ChAc and acids, it is easy to determine the melting transitions (≈80°C for ChAc, and 198°C, 158°C and 143°C for ascorbic, citric and maleic acids, respectively), the situation for the mixture appears quite complex. All the studied mixtures exhibit a strong tendency to form glass

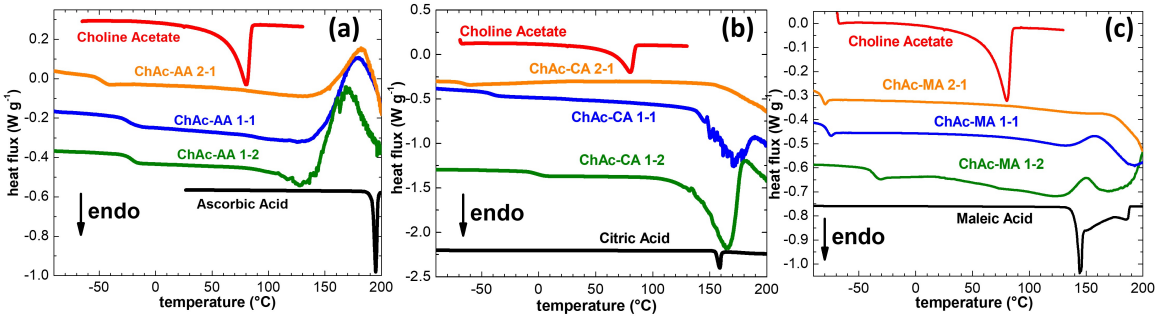

Figure 4.13: DSC curves measured on heating for ChAc based systems: (a) ChAc-ascorbic acid, (b) ChAc-citric acid and (c) ChAc-maleic acid. The DSC curves of pure components were also reported.

phases and indeed demonstrate glass transitions at relatively low temperature with the transition temperatures that rises proportionally with the concentration of the acid in the mixtures. GT is measured between -44°C and -17°C for ChAc-AA, between -60°C and 3°C for ChAc-CA and between -79°C and -32°C for ChAc-MA samples. Although evaluated only qualitatively, it is worth noting that the viscosity of these liquids is particularly high, which elucidates their propensity to undergo vitrification. At high temperatures the DSC curves show exothermic peaks, attributed to the decomposition process. In the light of verifying our interpretation, we measured the thermal stability of each sample (pure components and their mixtures) by thermogravimetry. The TGA curves reported in figure 4.14 show the mass loss ($\Delta m/m\%$) as a function of temperature. On the basis of the decomposition temperature (T_d), defined as that for which a $\Delta m/m\%$ of 5% was detected, we observe that ChAc and AA are more stable than their mixtures, exhibiting T_d equal

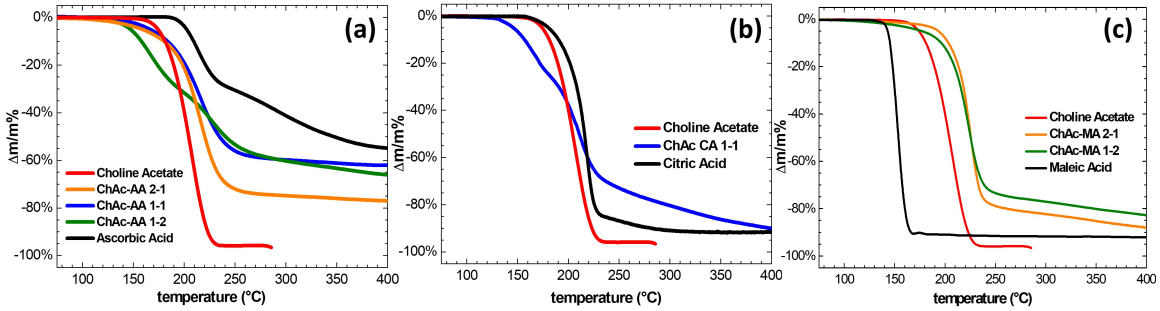

Figure 4.14: TGA curves for ChAc based systems: (a) ChAc-ascorbic acid, (b) ChAc-citric acid and (c) ChAc-maleic acid.

to 173°C and 202°C respectively, while the decomposition of their mixtures begins around 150°C. While the thermal decomposition pattern observed for ChAc-CA is similar to that of ChAcAA (the mixtures are less stable than their components), the situation appears completely different for the MA-based mixtures that show an increased thermal stability of the mixtures. A summary of the principal thermal process discussed in this section is reported in table 4.2

The situation appears slightly different for TBAAc-based systems: the curve of TBAAc indicates the presence of a glass transitions at -53°C, and a melting process that occurs in three subse-

quent steps between 69°C and 96°C. This can be explained by considering that the cation has a higher structural complexity and TBAAc can show polymorphism in the solid state. In general, the DSC profile (figure 4.15) of the mixtures composed by TBAAc is more complex than those involving ChAc and the presence of glass transitions was observed in many samples. All TBAAc-AA mixtures exhibit a glass phase below -44°C and -19°C (the lowest GT was observed for 2-1 composition). After passing the glass transition, TBAAc-CA based systems show exothermic peaks, occurring up to 0°C. This is attributed to the cold crystallization process, followed by melting between 65°C and 75°C. In conclusion MA-based mixtures present glass transition only for 1-2 composition. The 1-1 mixture undergoes melting at 63°C, while the 2-1 mixture melts with a two-step process between 75°C and 100°C. Although is not easy to measure the exact melting temperature of all the samples through this thermal characterization, it is still possible to observe a general lowering of the melting point in the mixtures as compared to pure components.

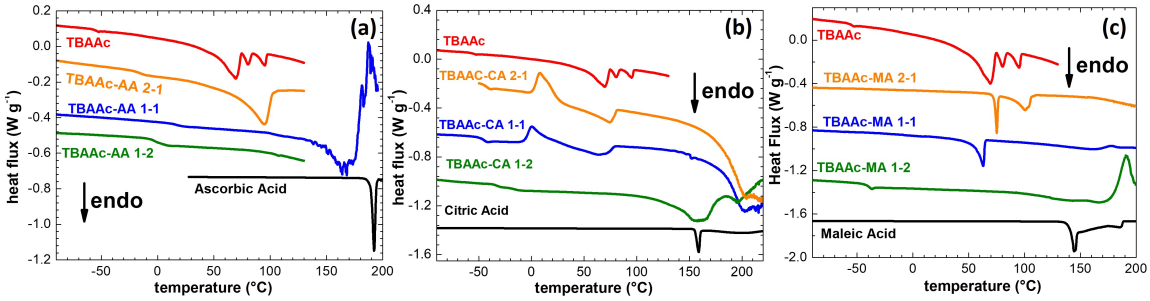

Figure 4.15: DSC curves for ChAc based systems: (a) ChAc-ascorbic acid, (b) ChAc-citric acid and (c) ChAc-maleic acid.

Table 4.2: Characteristic temperatures of the principal thermal process for ChAc-based mixtures (left) and TBAAc-based mixtures (right)

Sample	$\mathbf{T}_g$ (°C)	$\mathbf{T}_m$ (°C)	$\mathbf{T}_d$ (°C)
Choline Acetate	-	80	173
ChAc-AA 2-1	-44	-	157
ChAc-AA 1-1	-19	-	164
ChAc-AA 1-2	-17	-	146
Ascorbic Acid	-	194	202
ChAc-CA 2-1	-60	-	-
ChAc-CA 1-1	-17	-	146
ChAc-CA 1-2	3	-	-
Citric Acid	-	158	181
ChAc-MA 2-1	-79	181	178
ChAc-MA 1-1	-74	-	-
ChAc-MA 1-2	-32	-	194
Maleic Acid	-	143	143

Sample	$\mathbf{T}_g$ (°C)	$\mathbf{T}_{cc}$ (°C)	$\mathbf{T}_m$ (°C)
TBAAc	-53	-	69, 80, **96**
TBAAc-AA 2-1	-11	-	94
TBAAc-AA 1-1	20	-	-
TBAAc-AA 1-2	4	-	-
Ascorbic Acid	-	-	194
TBAAc-CA 2-1	-38	8	74
TBAAc-CA 1-1	-42	1	65
TBAAc-CA 1-2	-29	-	-
Citric acid	-	-	181
TBAAc-MA 2-1	-	-	75, 100
TBAAc-MA 1-1	-	-	63
TBAAc-MA 1-2	-36	-	-
Maleic Acid	-	-	143

Medium Infrared spectroscopy (MIR)

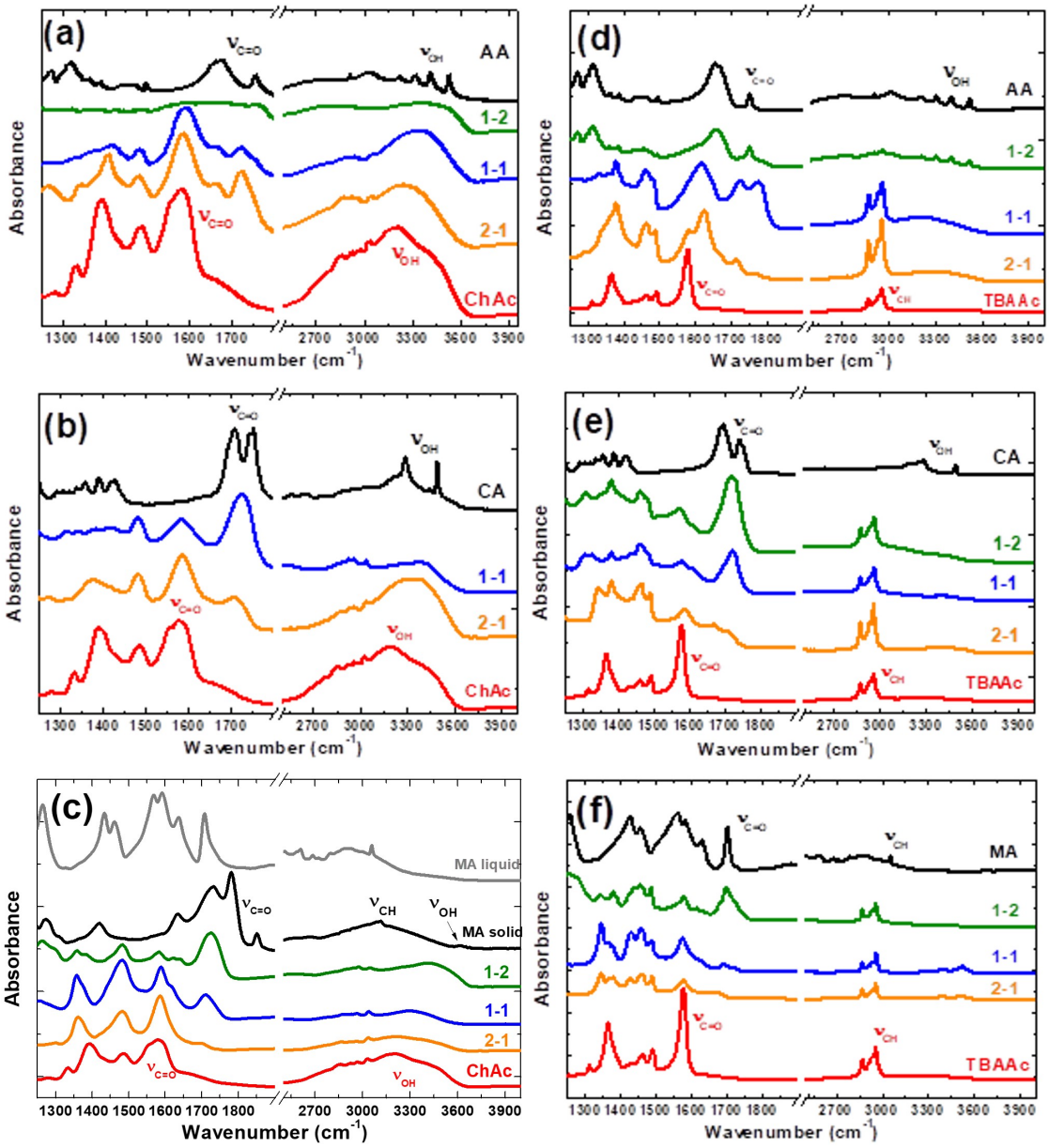

Figure 4.16: MIR spectra of acetate-based systems: (a) ChAc-ascorbic acid, (b) ChAc-citric acid and (c) ChAc-maleic acid; (d) TBAAc-ascorbic acid, (e) TBAAc-citric acid, (f) TBAAc-maleic acid

Infrared measurements, in the MIR region, were conducted to investigate the coordination between the various components. With this aim we compared the IR spectra of the pure compounds with those of the mixtures in figure4.16. We expected interactions to occur between the carboxylate and acids through the formation of hydrogen bonding and therefore we focused on the bands susceptible to this interactions, i.e. stretching modes, ν, of the carboxylic and hydroxyl groups. The spectra of each acid and ionic couple were assigned on the basis of quantum chemical calculation and previous assignments [91, 92, 93, 94, 30]. From the low frequency of the stretching modes of the carboxylic (1579 cm^{-1}) and hydroxyl groups (3200 cm^{-1}) we can affirm that the ionic species in ChAc are strongly coupled. This strong coupling is also confirmed by theoretical calculations. The spectrum of AA measured in solid phase, figure4.16a, shows a complex OH stretching region: the band is splited in four sub-bands in the range comprised between 3200-3500 cm^{-1} due to the presence of four different OH substituents in the molecule. Upon observing the spectra of ChAc-AA mixtures, discernible effects of coordination between ChAc and AA emerge. The OH stretching bands exhibit a notable shift towards higher frequencies with increasing acid concentration. Specifically, the lowest OH frequencies were recorded at 3198 cm^{-1} for ChAc, 3252 cm^{-1} for the 2-1 mixture, 3350 cm^{-1} for the 1-1 mixture, and 3404 cm^{-1} in ChAc-AA 1-2. These findings suggest that in the mixture, the ion pair remains coupled and the interactions with AA marginally destabilize the hydrogen bond between cation and anion. This effect is also evident in the stretching modes of the carboxylic group ($\nu_{C=O}$) of ChAc: the most intense peak slightly shifts to higher wavenumbers with increasing molar ratio of acid (1578 cm^{-1} in ChAc, 1584 cm^{-1} and 1589 cm^{-1} for ChAc-AA 2-1 and 1-1, respectively). The $\nu_{C=O}$ of AA is measured at higher frequencies (around 1700 cm^{-1}); the stretching of C=O shifts from 1755 cm^{-1} in pure AA to 1720 cm^{-1} in the ChAc-AA 1-1 and ChAc-AA 1-2 mixtures. This spectral change can be attributed to the coordination of functional groups in the liquid phase. A similar trend was also observed for other ChAc-based mixtures: typically, we measured a blue shift of the OH band as the ratio of acid in the mixtures increases. Notwithstanding the spectral feature of the $\nu_{C=O}$ vibrations results much complex, the slight shifts in the bands of the acids are indicative of a rearrangement

in the coordination of these groups between the pure acid and the mixtures.

The spectra of TBAAc were acquired by means of the ATR technique, in order to facilitate the sample treatment. Notwithstanding the structural differences between the choline and tetrabutylammonium cations in the coordination with anion, the frequencies related to the carboxylic vibrations are essentially the same observed in ChAc ($\approx$ 1580 cm^{-1}). As concerning the ν_{OH} modes in the TBAAc-AA 1-2 spectrum (figure 4.16d), the bands included in the 3500-3200 cm^{-1} range are substantially the same as those of pure AA. In the 1-1 and 2-1 mixtures the band structuring observed in 1-2 disappears and the bands are in general red shifted. Regarding the $\nu_{C=O}$ vibrations, the highest wavenumber is measured in pure AA and in TBAAc-AA 1-2 (1753 cm^{-1}); in the equimolar mixture, the $\nu_{C=O}$ band appears splitted into two contributions (1728-1780 cm^{-1}). The same is observed in TBAAc-AA 2-1 although the intensity of the second peak is quite small (1715-1770 cm^{-1}). The $\nu_{C=O}$ of TBAAc is barely visible in 2-1 mixtures and probably covered by the $\nu_{C=C}$ band in other mixtures. Some analogies can be found for other TBAAc-based mixtures. From the analysis of the MIR spectroscopy results, several noteworthy observations can be made. The low frequency of ν_{OH} and $\nu_{C=O}$ vibrations of choline acetate suggests a strong binding within the ionic couple. When mixed with acids, $\nu_{C=O}$ slightly shifts to higher wavenumbers; conversely, ν_{OH} undergoes blue shifts proportional to the acid content. The $\nu_{C=O}$ frequency of the acid appears to be primarily influenced by coordination, as it progressively undergoes a red shift with decreasing acid concentration in the mixtures. These general considerations also apply to TBAAc-based mixtures. All these results seem to demonstrate the presence of a strong network of H-bonds in the mixtures. For these reason, to deeply investigate on the H-bonds, we performed measurements in the far infrared spectral region (20-600 cm^{-1}).

Far infrared spectroscopy (FIR)

Far-infrared (FIR) spectroscopy, although necessitating a sophisticated and expensive experimental setup, have provided fascinating insights into the interaction of hydrogen bond and dispersion forces[95]. In the case of water, FIR spectra reveal, around 100K, two distinct bands at approx-

imately 230 and 160 cm^{-1}, corresponding to the stretching modes of intermolecular hydrogen bonds in different directions[86]. Additional information can be obtained by collecting FIR spectra as a function of temperature: the spectral changes can be related to possible intermolecular rearrangements due to phase transitions. Moreover the amplitudes of the low frequency intermolecular vibrational modes increase at low temperature; for example the H-Bond directionality increases and its vibrations are better detectable and resolved in the FIR region. The measurements described here were conducted at the AILES beamline of the synchrotron SOLEIL, using a cryogenic system to control the thermal cooling and heating rates of the samples. Due to the

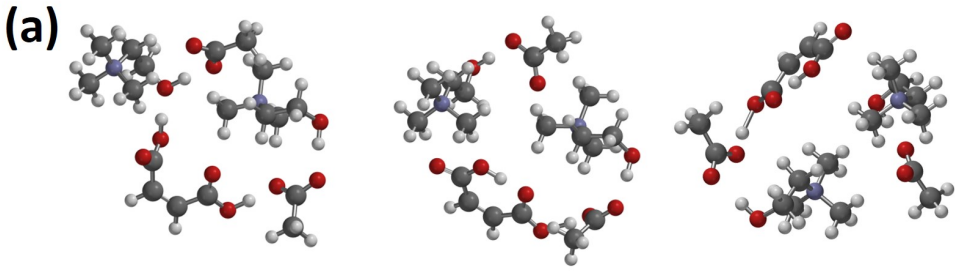

(a) 2-1 composition

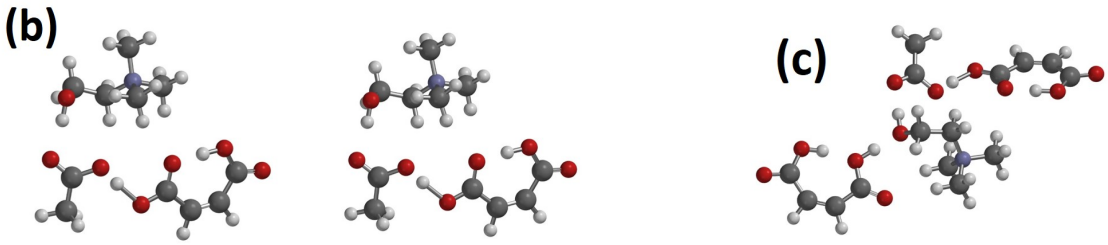

(b) 1-1 composition

(c) 1-2 composition

Figure 4.17: MM/B3LYP/6-31G** conformational analysis for each composition

high complexity of this spectral region, the interpretation of the experimental results was assisted by DFT calculations. The computational procedure for FIR spectrum assignment involves a preliminary conformational analysis at molecular mechanics level of theory, to explore all potential configurations assumed by the systems under analysis. The structures obtained from the explo-

ration of the potential surface were optimized at B3LYP/6-31G* level of theory. The conformers were selected on the basis of their energy, only including the configurations found within 6 kJ/-mol above the most stable one, as reported in figure 4.17. Only for this subset of structures, the Hessian matrix was computed for simulating their IR spectra. The contribution of higher energy conformers to the Boltzmann population has been omitted since negligible. In figure 4.18

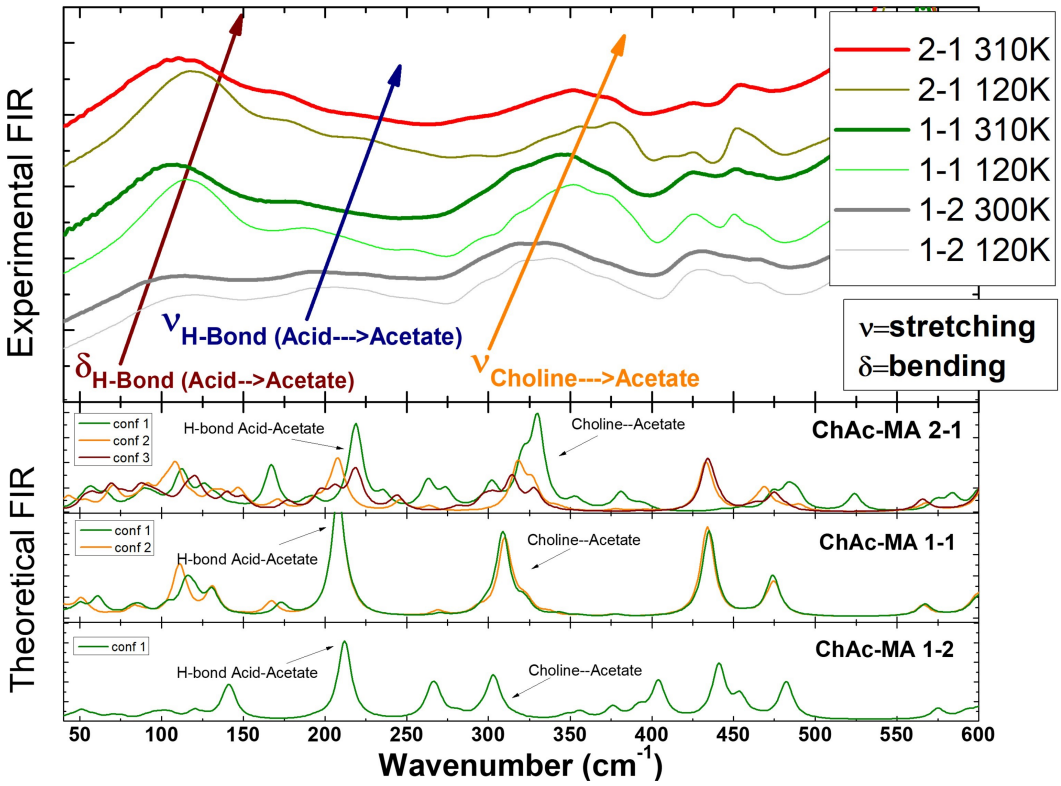

Figure 4.18: Experimental and theoretical FIR of ChAc-MA, measured as a function of temperature

we reported the experimental (upper panel) and computational (bottom panel) FIR spectra. The experimental spectra were acquired as a function of the temperature between room temperature and 120K. We reported the spectra measured on heating at the highest and lowest temperature for each mixture. The temperature was varied according to the same heating/cooling cycle used in the DSC measurements (at a rate of 5°C/min). The spectra collected at different temperatures

do not show significant differences in the positions of the bands: this is in accordance with the formation of glass phases on cooling, as observed by DSC (figure 4.13). The experimental spectra show a broad peak at about 100 cm^{-1} and another broader one at about 160 cm^{-1}, similarly to what previously observed for protic and aprotic ionic liquids [96, 97, 98, 99, 100] and respectively ascribed to the dispersion forces and the highly directional H-bonds, typically found in these liquids. Indeed, the bands at 160 cm^{-1} can reasonably be interpreted as the stretching of an highly directional hydrogen bond, as confirmed by DFT calculations. Conversely, the band at about 100 cm^{-1} appears more challenging to be interpreted. The computational models suggested that these bands are generated by the superposition of numerous contributions related to intermolecular interactions and skeletal movements of the components. Moreover, the calculations reveal that one component can be attributed to hydrogen bonding, specifically in the bending mode. As expected, the bands in the low-temperature spectra exhibit greater structuring and appear narrower. Experimentally, it is noteworthy that a hypsochromic shift of both the bands was observed as the concentration of the acid in the mixtures increase: this is rationalizable as an increase in the strength of the hydrogen bond at high acid concentrations, since the described bands are attributed to the movements of the hydrogen bond. It is also noteworthy that, based on the conformational analysis, an increase in acid concentrations in the mixtures leads to a reduction in the number of configurations. An initial interpretation was given by hypothesising that the acid, being able to donate multiple hydrogen bonds, forces the components to fix their positions in a more rigid structure. It is therefore possible to state that a higher quantity of acid is able to crosslink more efficiently, providing a greater number of hydrogen bonds and resulting in a stiffer structure. However, it is possible to further analyze the configurations present in the mixtures. The relative weight of each configuration depends on the Boltzmann distribution. As the temperature changes, the population of each level changes until the formation of glassy or solid phase, where the evolution of configurations no longer follows the Boltzmann population. In the experimental spectra as a function of temperature, especially for the measurements performed on the 2-1 composition, we observe the presence of an asymmetric band around 350 cm^{-1}, whose

shape noticeably varies with temperature. At low temperatures, a structured peak is observed in which two or three distinct contributions can be distinguished. The relative weights of these bands change as the temperature increases, and at temperatures close to RT, the contributions are almost indistinguishable. Our DFT investigation suggested that the band around 350 cm^{-1} is due to the superimposing contributions coming from different conformers. Although the univocal assignment of bands based on theoretical spectra is challenging, these spectra clearly indicate that in this frequency range each of the configurations obtained from the DFT calculation generates a band, mainly due to movements of the choline acetate but also involving maleic acid. The experimental band can be decomposed into different contributions by performing a deconvolution, with three Gaussian functions respectively centered at 340, 360 and 380 cm^{-1}, after a baseline correction. To investigate if changes in temperature of the band intensity are given by different conformations that superimpose their absorption bands and change their distribution with temperature, we chose to conduct a detailed analysis of the band profile as previously carried out on other systems[96]. In a liquid, the ratio (r) of a specific configuration concentration is proportional to the ratio of the intensities of its bands. The ratio r is defined as:

$$r = \frac{[C_{conf2}]}{[C_{conf1}]} \tag{4.2}$$

The thermodynamic equilibrium constant K between configurations is proportional to r and depends on ΔG^0:

$$-RTlnK = \Delta G^0 = \Delta H^0 - T\Delta S^0 \tag{4.3}$$

which can be rearranged in:

$$lnK = -\frac{1}{T}\frac{\Delta H^0}{R} + \frac{\Delta S^0}{R} + c \tag{4.4}$$

Plotting ln(r) vs 1/T allows to verify the van't Hoff dependence of the concentration from the temperature evolution; ΔH^0 can be also obtained by the slope of the best fit line. A linear relation of ln(r) vs 1/T is clearly observed from room temperature to approximately -90°C (figure 4.19) while a notable deviation from linearity is observed below this range. This can be attributed to the

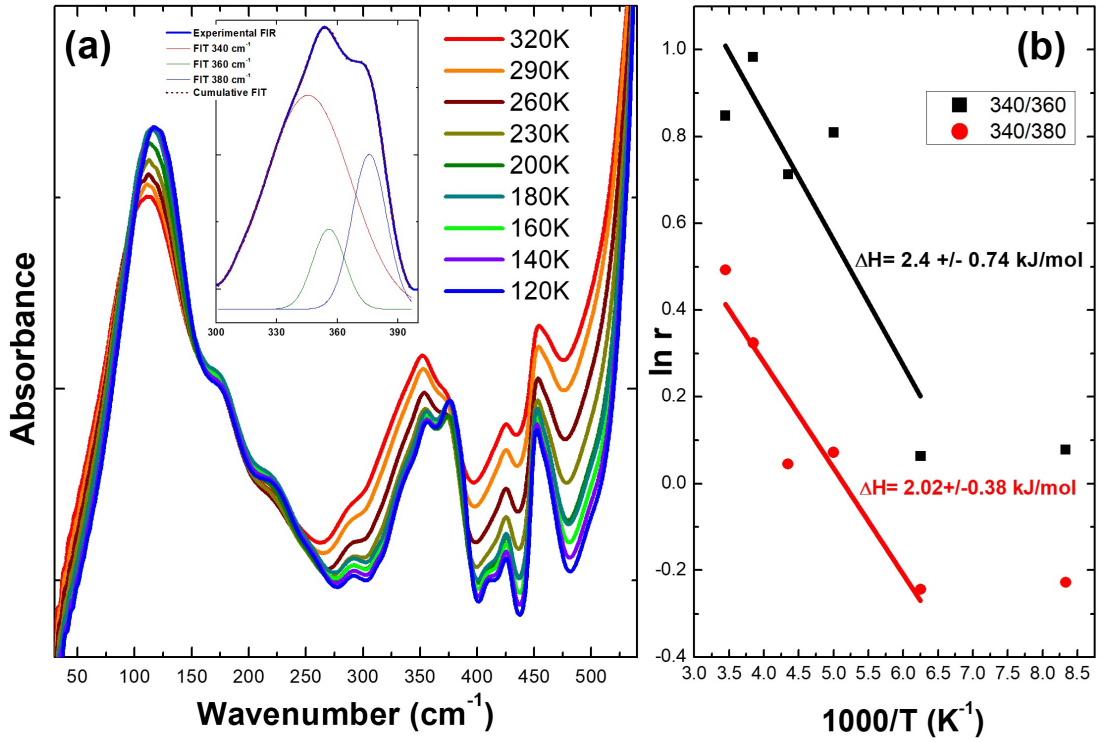

Figure 4.19: (a) ChAc-MA 2-1 experimental FIR spectra as a function of temperature and spectral deconvolution. (b) van't Hoff fit

formation of a glassy phase, consistently with the temperatures measured by DSC, and described in the preceding paragraphs. The energy separation between the configurations is about 2kJ/mol, slightly more pronounced than the energetic difference obtained from the DFT calculations. In figure 4.20 we reported the same analysis performed for the 1-1 composition. Fitting the peak between 280 and 400 cm^{-1} with the same Gaussian functions used in the previous analysis, a more linear trend in van't Hoff plot was observed up to T≈-90°C and the values of ΔH^0 obtained was again about 2kJ/mol. In addition, it should be specified that the error of ΔH^0 reported in both plots is a parameter obtained from the fit, derived from the χ^2 test and rationalizable as the standard deviation of the fit. In the composition 1-2, the analyzed band did not exhibit significant variations with changing temperature, when compared to the other compositions: the spectra are

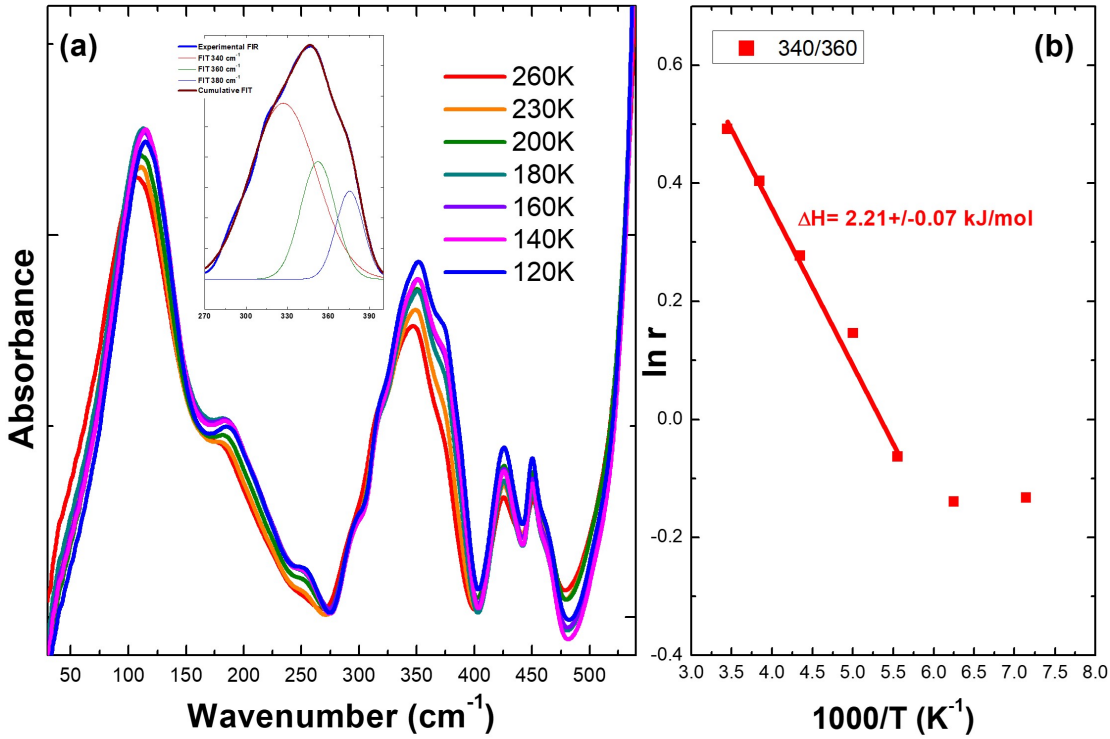

Figure 4.20: (a) ChAc-MA 1-1 experimental FIR spectra as a function of temperature and spectral deconvolution. (b) van't Hoff fit

reported in figure 4.21. The relative weights of the bands remained practically unchanged: this means there is no population redistribution , as confirmed by the DFT calculation, which indicated the presence of a single conformer. These results are in agreement with our hypothesis that the a higher amount of acid in the mixtures forces the system into a more rigid configuration, as it enhances crosslinking. The values of the energy separation between the configurations obtained from the fit of the experimental data, in good agreement with those arising from the DFT data, further enhances our interpretation.

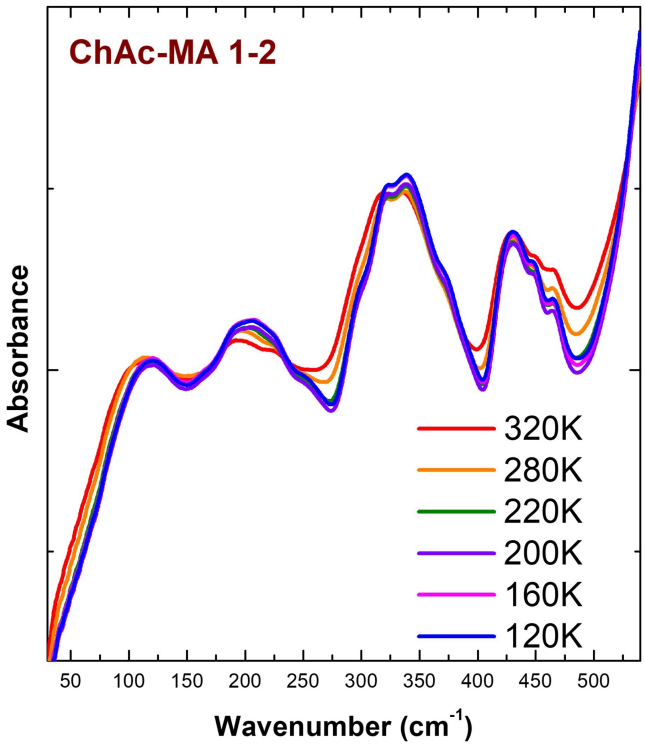

Figure 4.21: (a) ChAc-MA 1-2 experimental FIR spectra as a function of temperature

Molecular Dynamics analysis

With the aim of confirming the conclusions obtained from the infrared spectroscopy data, we decided to simulate all the mixtures and the two salts (ChAc and TBAAc) using classical molecular dynamics. The experimental results described in the previous paragraphs show that all the mixtures are characterized by a strong presence of hydrogen bonding. The idea was to investigate in detail all the possible distances that can be involved in these bonds (OH and C=O groups), comparing the obtained g(r) for each mixture, so as to verify a potential concentration effect. In Figure 4.22, we present the radial distribution functions (g(r)) computed for the ChAc-AA mixtures. Figure 4.22a illustrates g(r) between the hydroxylic hydrogen of choline (H3) and the oxygen atoms of acetate. In pure ChAc, the ionic couple is formed through a strong hydrogen bond between choline (donor) and acetate (acceptor). The observed distance of 1.6Å is consistent with a strong

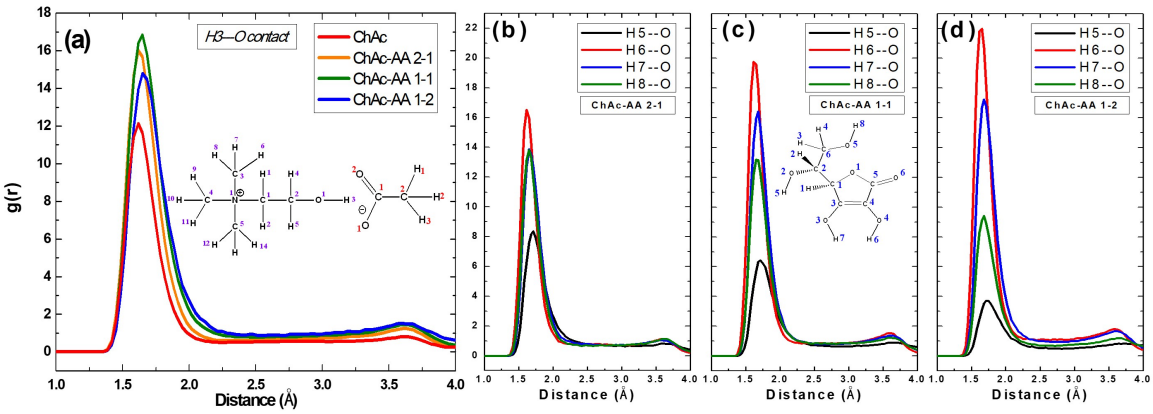

Figure 4.22: Radial distribution function g(r) computed for distances between H3 (choline) and O (acetate) and hydrogen atoms of AA and O-acetate (a). (b) composition 2-1, (c) composition 1-1 and (d) composition 1-2.

H-bond length. As indicated by infrared measurements, the interactions with AA do not significantly alter the coordination of the ion pair. The interaction between AA and ChAc involves the establishment of additional hydrogen bonds: AA contains four hydroxyl groups that can serve as H-bond donors. Therefore, we computed g(r) between the hydroxylic hydrogen atoms (H5, H6, H7, H8) of AA and the oxygen atoms of acetate (see figure 4.22b,c,d). All the considered hydrogen atoms can act as H-bond donors, with a notable preference for H6. The highest integral value for these peaks is obtained for the 1-2 composition, where the number of AA molecules is the largest one. This observation indicates that the acid acts as hydrogen bond donor: the g(r)s reported in figure 4.22 demonstrate that all the OH groups can act as HBDs, but higher integrals are observed the most acidic proton H6 (atomic labels are reported in figure 4.23). These considerations can be extended to the other ChAc-acids compositions. The coordination of the ionic couple remains unchanged regardless of the coordinating acids. In both cases, CA or MA act as H-bond donors, coordinating the anion through their most acidic hydrogen. In the case of the citric acid based mixtures, the most intense peak is related to the H5 proton, an alcholic proton stabilized by many resonance effects. Maleic acid curves, instead, reveal the occurrence of an

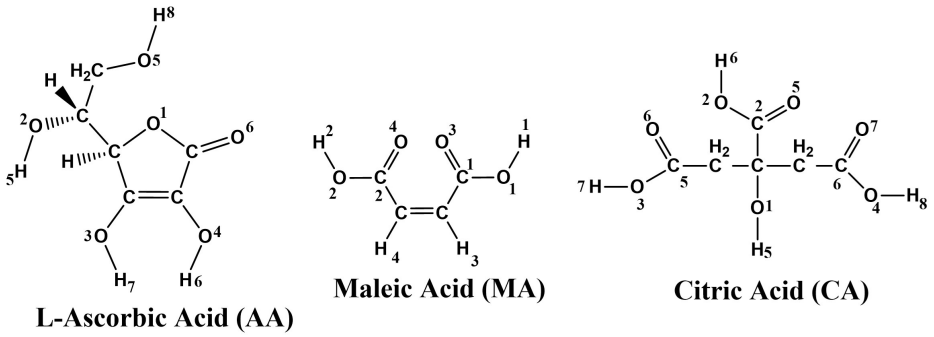

Figure 4.23: Atomic labels of acids

equiprobable interaction between H1 and H2 protons as a consequence of the symmetry of MA (the rdfs curve for ChAc-CA and ChAc-MA were reported in figure 6.3, in the Appendex section). The scenario appears quite different for TBAAc-based systems: unlike choline, TBA cation lacks OH groups and couples with the cations through CH$\cdots$O interactions. In figure 4.24, the radial

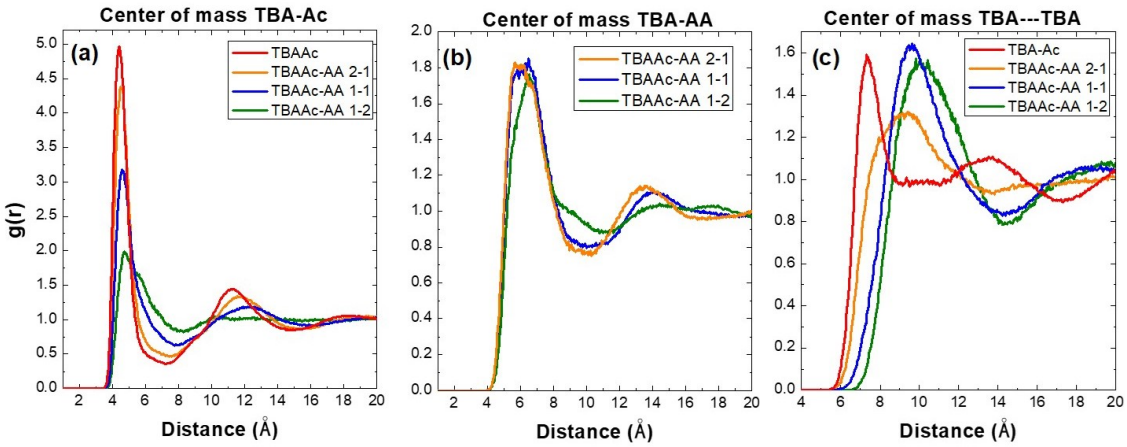

Figure 4.24: Radial distribution function g (r) computed between the center of mass of TBA and Ac (a), TBA and AA (b) and TBA and TBA (c)

distribution function (g(r)) was calculated between the centers of mass of the cation (TBA) and anion (acetate). This analysis reveals a significant contact at around 4.3 Å in pure TBAAc (red curves). This contact is only weakly destabilized by coordination with the acid, and it remains

substantially unchanged in the mixtures. The acids in the mixtures are situated approximately 6Å from the center of mass of the cation, as depicted in figure 4.24. The most interesting observation can be done observing the distances between the CM of the cations, which are increased when the ratio of acid rises: starting from the lowest values registered for the pure TBAAc (7.30Å) the distances increases at about 9.6-10.2Å in the mixtures. These results, as observed in all the mixtures with TBAAc, indicates that the ion pair remains substantially unaltered by the acids coordination, which can interpose between the ion pairs. As observed in ChAc-AA mixtures, ascorbic acid (AA) displays a strong tendency to act as a hydrogen bond donor, employing its four hydroxyl substituents. From the analysis of RDFs shown in figure 4.25, we indeed observe robust H-bond interactions. Specifically, AA forms a strong hydrogen bond with the acetate anion, with a length of approximately 1.6 Å. This interaction is consistently present across all ChAc-AA mixtures (see figure 6.2 in Appendix). As previously described, AA coordinates with the anion by employing the most acidic hydrogen, H6, which exhibits the highest integral. The microscopic arrangements described in TBAAc-AA mixtures are recurrent across all studied systems. In both TBAAc-AM and TBAAc-AC (as shown in figures 6.3 in Appendix), the coordination with acids leads to an increase of approximately 2Å in the distances between the centers of mass of the TBA molecules (TBA–TBA distance). On average, the acids are coordinated at a distance of approximately 9-10Å from the center of mass of the TBA, forming an alternating pattern of ionic pairs and acids. The coordination with acids occurs via hydrogen bonding at approximately 1.6-1.7Å. In Appendix section, figure 6.1 we reported the g(r)s for the distances between the centers of mass for both systems.

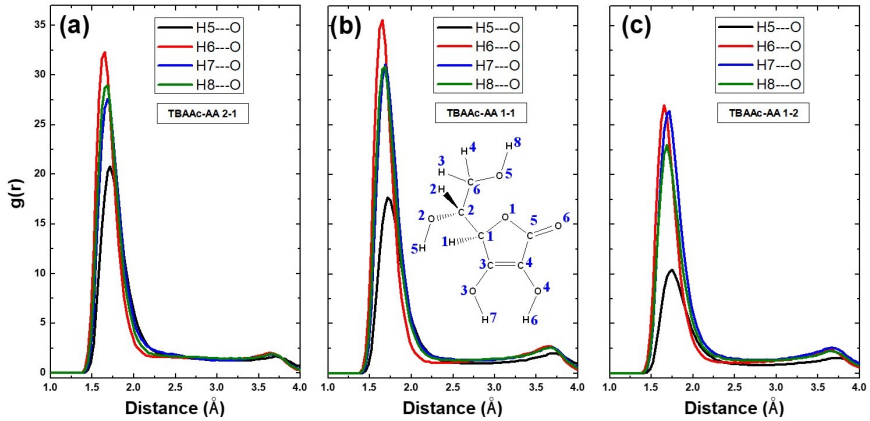

Figure 4.25: Radial distribution function g(r) computed between the hydroxyl hydrogens of ascorbic acid and oxygen atoms of acetate. (a) composition 2-1, (b) composition 1-1 and (c) composition 1-2

4.3 Phenol-Cyclohexanol

The results discussed in the previous paragraphs pertain to Type III deep eutectic solvents, specifically those in which the hydrogen bond is formed by quaternary ammonium salts. In both the discussed systems it is evident that the role of HBD is carried out by the anions: both imidazole and organic acids donate hydrogen bonds to the anions, which in turn are coordinated in a bridging structure with the cations. Many experimental and computational results suggest that the mixtures present in general a higher degree of disorder with respect to the starting materials, especially in the systems based on tetrabutylammonium. This disorder is reflected in the thermal properties of the systems and can also observed from the molecular dynamics analysis. The X-ray and the g(r) functions, in fact, suggest that the liquid phases are organized in an alternate pattern of the components. In all systems the presence of hydrogen bond interactions has been observed through experimental and computational techniques. In recent years, alongside the formulation involving ionic H-bond acceptor, non-ionic systems, called type V deep eutectic solvents were proposed. Our idea, therefore, in light of what was studied for type III DESs, was to investigate the possible differences in the formation of these polar and neutral mixtures, whose

HBA structures are significantly different from those used in type III. The most compelling type V DESs was proposed by Coutinho and coworkers[28] and consists in the 1-1 thymol-menthol mixtures. This system shows a strong deviation from thermodynamic ideality: deviations from ideality are originated from the strength of the hydrogen bond between different components. The system proposed by us consists in DESs formed by cyclohexanol and phenol, which differs from the thymol-menthol system in that the starting components have no substituents on the rings. Therefore, the idea is to investigate how the substituents may influence the spatial arrangement of the components and how these can impact the thermodynamic properties.

Phase diagram by means of DSC investigation

The eutectic point of the studied binary mixture was initially estimated by thermodynamic modelling of the ideal solid-liquid equilibrium phase diagram (SLE) solving equation 4.5 equation [31]:

$$ln(a_i) = \frac{\Delta H_m}{R}\left(\frac{1}{T_m} - \frac{1}{T}\right) \tag{4.5}$$

where a_i is the activity of the i-th component, T_m and ΔH_m the melting temperature and enthalpy of the pure compound, respectively. It is noteworthy that in equation 4.5 we considered negligible the differences in molar heat capacity of the i-th component in the liquid and solid phase. The ideality behaviour is obtained imposing the activity coefficient equal to molar ratio (a_i=x_i). The ideal SLE suggest that the eutectic composition is expected at molar ratio of cyclohexanol (x_c) equal to 0.8. Based on this premise, we investigated the phase diagram of the PheOH-CycOH system using differential scanning calorimetry (DSC), preparing mixtures with compositions in close proximity to this particular value. Figure 4.27 illustrates the DSC curves for both pure cyclohexanol and pure phenol, as well as ten of their mixtures. As shown in figure 4.27 cyclohexanol melts at 25.6°C, although the curve exhibits additional endothermic peaks, which are attributed to transitions of the polymorphic structure of cyclohexanol [101, 102, 103]. Phenol melts at 45°C. According to thermodynamics, an eutectic composition refers to an homogeneous phase that undergoes melting at a precise temperature. For mixtures that deviate from the eutectic composition, we expect

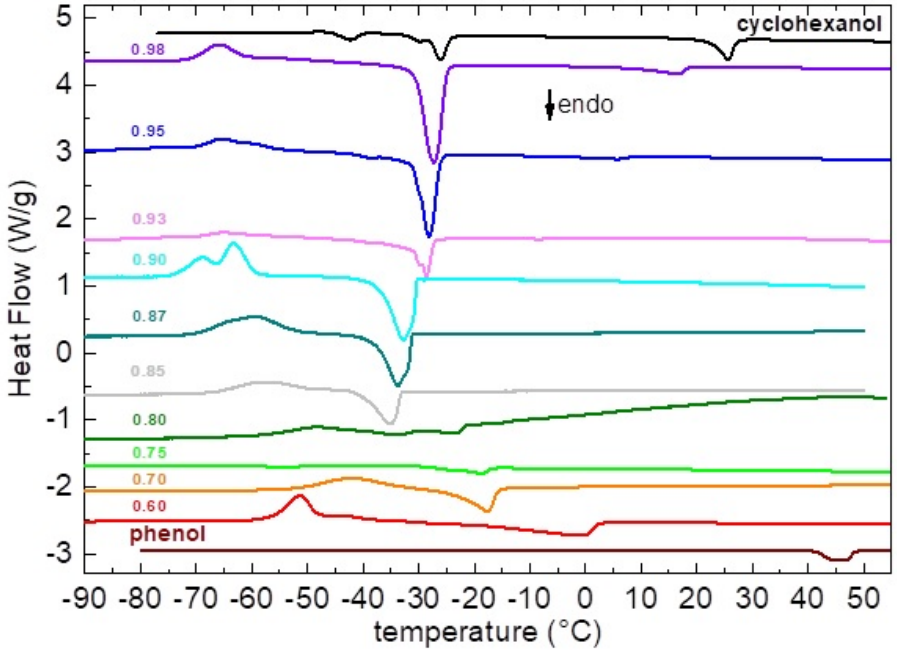

Figure 4.26: DSC curves measured on heating for cyclohexanol and phenol pure components and for their mixtures at different compositions

to observe two melting transitions: one close to the eutectic melting and another associated with the phase containing an excess of one of the two components. Indeed, in our system we observe two melting processes for the non-eutectic compositions with $x_c \neq 0.85$. It is interesting to note that the ΔT between the two peaks for each composition decreases as it approaches the eutectic composition. For example, in x_c=0.98 the first transition is at 17°C and the second at -28°C, in x_c=0.95 the first is centered at 6°C and the second one at -28°C. The other composition exhibits the same trend: this is explainable considering the transition at lower temperature originated by the melting of a composition close to the eutectic composition (quasi-eutectic) and the other related to the melting of a composition containing an excess of one component. The scenario appears different for composition with lower concentration ($x_c \leq 0.75$). with only one clear en-

dothermic peak observed, whose temperature increases as the concentration approaches that of pure phenol. All the mixtures show the presence of a cold crystallization process. The intermediate compositions ($0.80 \leq x_c \leq 0.93$), when measured at the same temperature scanning rate (5°C/min) used for the other mixtures, do not show clear phase transitions. In $x_c \geq 0.95$ and $x_c \leq 0.75$ it was also observed the absence of crystallization, sign that the crystallization of samples is slow and can be suppressed or retarded at high temperature rates. Hence, for samples where $0.80 \leq x_c \leq 0.93$, DSC measurements were conducted again at a significantly lower temperature scanning rate ($\Delta T/\Delta t$=0.6 °C/min), which is nine times slower than the previous rate. Apart for the mixture at x_c=0.85 the melting transitions is composed of two differentiated process: the lowest T_m, -35°C, was found for the composition x_c=0.85, which reasonably corresponds to the eutectic composition.

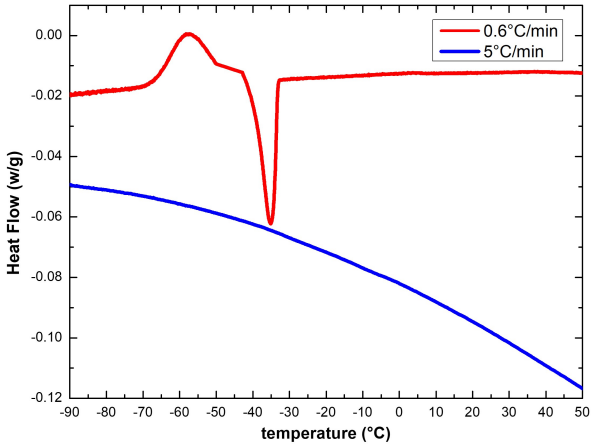

Figure 4.27: Comparison between heating process of 0.85 samples: 5°C/min (blue line) and 0.6°C/min (red line)

Table 4.3: Melting temperature and Cyclohexanol Molar Ratio

Cyclohexanol Molar Ratio (x_c)	Temperature (°C)
1	25.6
0.98	17
0.95	6
0.93	-28
0.90	-32
0.87	-33.7
0.85	-35
0.80	-34.1
0.70	-18
0.60	0.7
0	45

Quantum chemical modelling

The phenol-cyclohexanol system was modelled by QM calculations, proposing a series of complexes where both molecules (phenol, PheOH and cyclohexanol, CycOH) interact between each other with different geometries: these calculation were conducted to characterize the energetic and geometrical features of the interactions between the components. For these reasons, we initially studied models to describe the interactions between the pure components, optimizing cyclic tetrameric structures of cyclohexanol and phenol at the M062X/6-311G** level of theory within S_4 symmetry. It is quite evident that these models do not accurately describe the structural organization in either the crystalline or liquid phases. Furthermore, cyclohexanol, due to its polymorphic structure, exists in two configurations in the solid phase. Nevertheless, each tetramer here proposed describes a structural arrangement expected in condensed phase where molecules simultaneously act as both donors and acceptors of hydrogen bonding. For phenol we found two stable structures: the first one sees a cyclic tetramers were the four phenol groups interacts only via H-bonds; the second one shows a further π-π interaction between two phenolic rings

which stabilize (27 kJ/mol) the structures. When mixed, both molecules can interact via hydrogen bonding. To analyze the hydrogen bonds resulting from the interaction, we introduced two heterotetramers with S_2 symmetry. These consisted of two CycOH and two PheOH molecules, arranged in an alternating and cyclic manner, as reported in figure 4.28. The O$\cdots$H distances

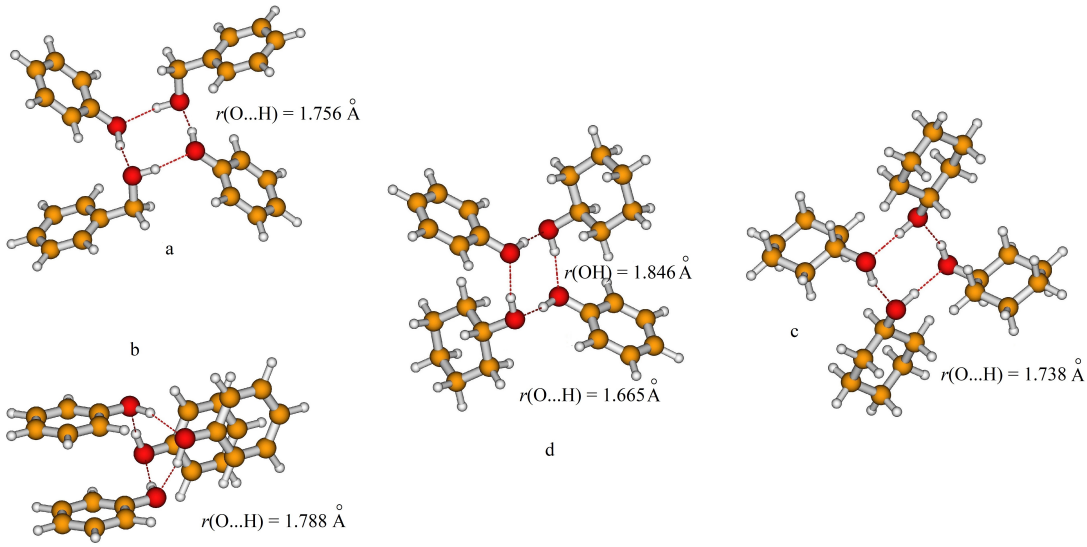

Figure 4.28: Tetramers of phenol, (a and b, S_4 symmetry), cyclohexanol (c, S_4 symmetry) and phenol-cyclohexanol (d, C_2) symmetry)

computed for the homotetramers suggested that, although PheOH is an excellent HBD, CycOH promotes a more efficient H-bond: CycOH, in fact, can donate and accept the hydrogen bonding better than PheOH, which is a good HBD but can scarcely behave as HBA. thus the better HBD property of PheOH mixed with the better HBA property of CycOH gives the formation of the shortest intermolecular O$\cdots$H distances (1.665 Å).

A complementary way to describe the nature and strength of the interactions can be obtained from the Atom in Molecules theory (AIM): this method lays the foundation on the topological analysis of the molecular electron density surface. The characterization of intramolecular and intermolecular bonds is made by localizing bond critical points (r_c) on the bond path between the

acceptor and donor, and analysing the values of electron density ($\rho(r_c)$ and its Laplacian $\nabla^2\rho(r_c)$ at the bond critical point. Hydrogen bonds can be classified on the basis of the values of $\rho(r_c)$ and $\nabla^2(r_c)$. Our calculations suggested that CycOH forms H-bonds more stable than ones formed by PheOH. In addition the negative values of the total electron density (potential and kinetic electron densities) H(r_c) suggested that the H-bond in both homoclusters can be classified as strong, with a slight preference for CycOH molecules. Regarding the heterocluster, instead, PheOH and CycOH are linked via stronger H-bonds, as suggested by AIM analysis. The results are summarized in table 4.4.

Table 4.4: Hydrogen bond geometry (Å), topological analysis (a.u.) and interaction energy ΔE (kJ/mol) obtained at the M062X/6-311G** level for the tetramer models.

	PheOH (4.28a)	**PheOH(4.28b)**	**CycOH**	**PheOH+CycOH**[a]
ρ (r_c) (a.u.)	0.0372	0.0356	0.0411	0.0494
∇^2 (r_c) (a.u.)	0.1346	0.1277	0.138	0.1467
H (r_c) (a.u.)	-0.0007	+0.0003	-0.0022	-0.0064
rO$\cdots$H (Å)	1.756	1.788	1.738	1.665
ΔE(kJ/mol)	-71	-79	-77	-82

[a] Only PheOH$\cdots$O values are reported

The association energy (ΔE) in each molecular cluster was evaluated computing the difference between the total energy and the energy of each monomer and corrected by the basis set superposition error (BSSE)[84]. The results presented in Table 4.4 indicate a stronger hydrogen bonding between PheOH and CycOH in the heterotetramers compared to the homoclusters. It is important to note that while hydrogen bonding is undoubtedly the primary intermolecular interaction in both pure and mixed components, weaker van der Waals interactions can also play a substantial role in stabilizing the systems. The reported energy interaction values consider all components comprehensively. In order to better characterize the different energy contributions to the stabilization of the structures we applied the Noncovalent Interaction (NCI) approach: this

computational tools, also known as reduced density gradient (RDG) allow to discriminate van der Waals, hydrogen bonds and steric repulsion in a complex [104]. The isosurfaces obtained for the tetramers are reported in figure 4.29: each contribution is represented by a proper color (blue corresponds to highly attractive interactions, i.e. hydrogen bonds, green corresponds to weak interactions, such as van der Waals contribution and red indicates strong repulsion)[65]. In the PheOH tetramer case (figure 4.29a), the intermolecular association is defined by a specific interaction site in the OH$\cdots$O region, revealed by the presence of a hydrogen bond (shown in blue). Additionally, there are regions (highlighted in green) with limited extension, indicating van der Waals interactions involving the hydrogen atoms of the benzene ring and the oxygen of the OH group. In the PheOH tetramer shown in figure 4.28,b, when the benzene rings are aligned to promote π-π interactions, a substantial van der Waals region is found between the two rings. This interaction contributes to the greater stability observed in this tetramer, as mentioned earlier. In the CycOH tetramer depicted in figure 4.29, in addition to the hydrogen bond sites, we observe green areas over an extended region, indicating a stabilizing interaction between cyclohexyl rings. In the PheOH-CycOH tetramer in figure 4.29 we once again see hydrogen bonds between molecules, with more prominent spots in the OH$\cdots$O region where phenol acts as the hydrogen bond donor, in line with expectations. Additionally, there are smaller green spots, suggesting that the interactions between benzene and cyclohexyl rings are weaker than those between cyclohexyl rings in the CycOH tetramer. The AIM analysis combined with the NCI study indicates therefore that heteroassociation is energetically preferred with respect to homoassociation in the PheOH-CycOH system because hydrogen bond is stronger between different components, however van der Waals interactions between cyclohexyl rings have a significant role in self association of cyclohexanol beyond the localized hydrogen bond.

Infrared spectra

As previously discussed for deep eutectic solvents, infrared spectroscopy was demonstrated to be a valid approach for studying the effects arising from intermolecular interactions. In the phenol-

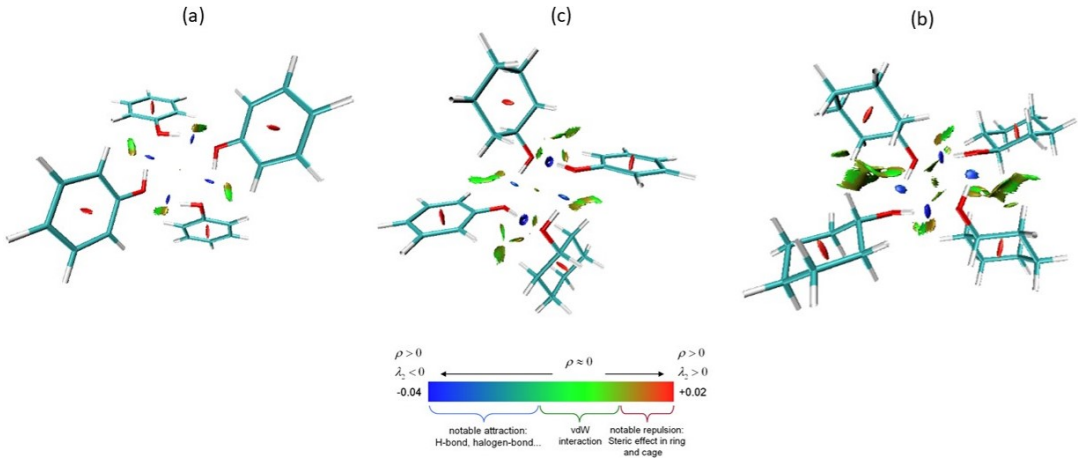

Figure 4.29: NCI analysis for the PheOH, CycOH and PheOH-CycOH tetramers.

cyclohexanol system, the main interactions occurred through hydrogen bonding between two alcoholic molecules. Although the bands related to the movements of the OH group in phenol and cyclohexanol are distinguishable, evaluating the shifts of these bands in their mixtures becomes practically impossible. Therefore, we decided to calculate the theoretical vibrational spectra, assigning the bands, and analyze the experimental spectra in light of the computational spectra. Initially, we compared the vibrational spectra calculated for the PheOH, CycOH, and PheOH-CycOH tetramers, previous described. The assignment of the primary bands, determined through the analysis of normal modes, is presented in figure4.30. In the spectrum of the PheOH-CycOH complex, we distinguished the bands associated with each component using different colors. Notably, in the high-frequency region the OH stretching modes are clearly influenced by the coordination pattern between the components. Upon heteroassociation, the νOH frequencies shift from their values calculated for the PheOH and CycOH homotetramers. Specifically, the νOH mode of PheOH, acting as a hydrogen bonding donor, shifts to a lower frequency, whereas the νOH of CycOH, acting as a hydrogen bond acceptor, moves to a higher frequency. This spectral pattern aligns perfectly with the strengthening of hydrogen bonding between components due to mixing. Consequently, the frequency shifts of the νOH mode can serve as a diagnostic indicator

for changes in the strength of the intermolecular interaction. Additionally, the remaining vibrational modes of the OH group—namely, the in-plane (δ) and out-of-plane (γ) bending modes—also exhibit frequency values that are sensitive to the strength of the O(H)$\cdots$O interaction. When different components are mixed, the δOH frequency of PheOH increases while the δOH of CycOH decreases. This aligns with the formation of a stronger hydrogen bond. The same, and even more pronounced, effect is found for the γOH modes. In light of the results obtained from the theoretical spectra, we proceeded to analyze the hydrogen bonds between different components based on the spectral changes observed in the infrared spectra after mixing. In figure4.31, we present a

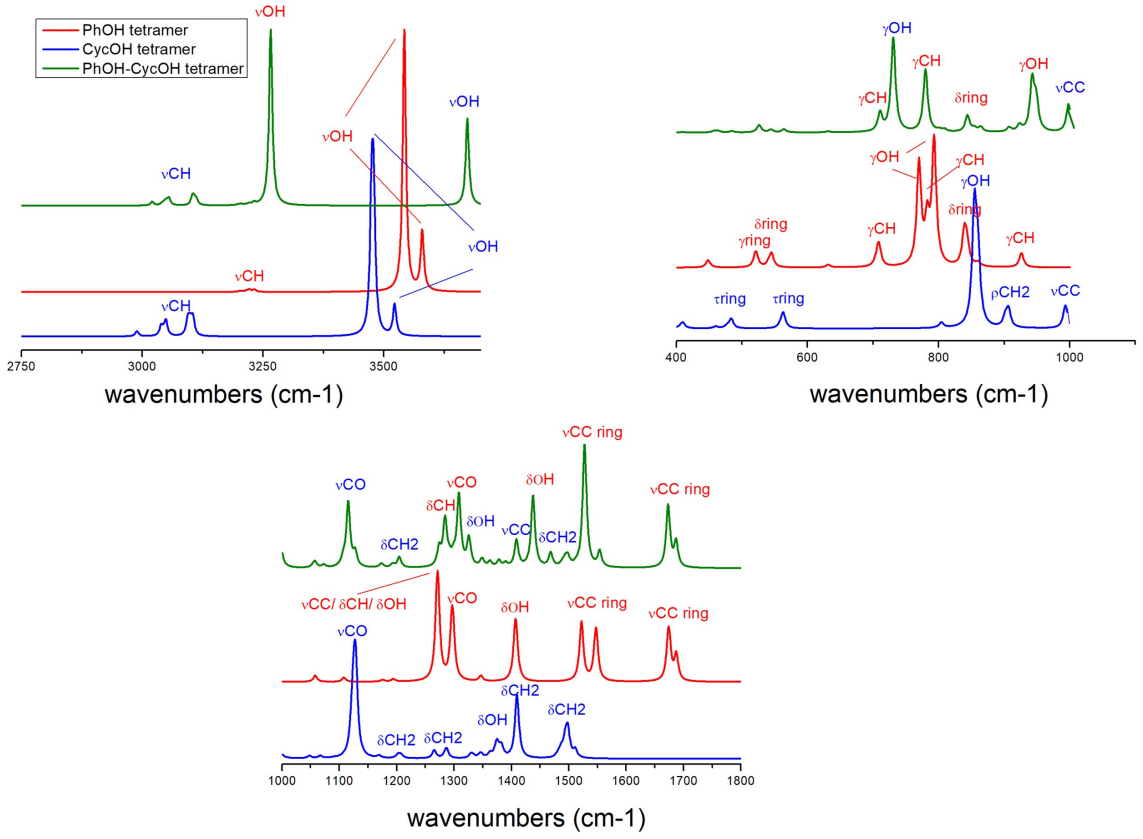

Figure 4.30: Theoretical infrared spectra calculated at M062X/6-311G** level of theory for the tetramers of PheOH, CycOH and PheOH-CycOc.

comparison between the experimental IR spectra of pure PheOH and CycOH components and the spectrum of the liquid mixture at the composition x_c=0.85. The assignment of the main bands is based on information obtained from our calculated spectra and from literature sources for CycOH [105, 106, 102] and PheOH [107, 108]. The OH stretching absorption exhibits a broad band in the spectra of the pure components, with frequency maxima observed at about 3364 cm^{-1} for PheOH and 3328 cm^{-1} for CycOH. This band appears slightly broader in the mixture compared to the pure component spectra, suggesting a potential variation in the coordination of the OH group. Due to the challenge of assigning the overlapping νOH bands of each component in the mixture spectrum, the absorption band was deconvoluted into two Gaussian-shaped components (figure 4.32). The band profile is reproduced by two Gaussian components peaking at 3254 cm^{-1} and 3396 cm^{-1}, indicating a small alteration in the vibration stretching frequency of the OH groups. In the mid-frequency range, the δOH absorption of phenol manifests as a shoulder to the more pronounced νCO band, both in the pure phenol spectrum and in the mixture spectrum. The δOH absorption of cyclohexanol is clearly discernible in both pure and mixed states, and its frequency remains largely unchanged. The spectra maintain a high degree of similarity in the low frequency range, where the γOH frequency of cyclohexanol appears to be rather unaffected by the mixing process. Conversely, a slight blue shift is observed for the γOH frequency of phenol. The infrared spectra confirm that the majority of absorptions in the PheOH and CycOH mixture at eutectic composition closely align with the frequencies of the pure components. Only marginal blue shifts are evident in the δOH and γOH vibrations of phenol, which qualitatively corresponds to the spectral characteristics of the discussed tetramers.

X-ray and MD simulations

The computational models described so far, while providing valuable insights into the intermolecular coordination of the components before and after mixing, are too limited in scope to capture the long-range interactions present in the bulk phase of the eutectic liquid. Indeed, the spectroscopic characterization has enabled a comprehensive exploration of hydrogen bonding inter-

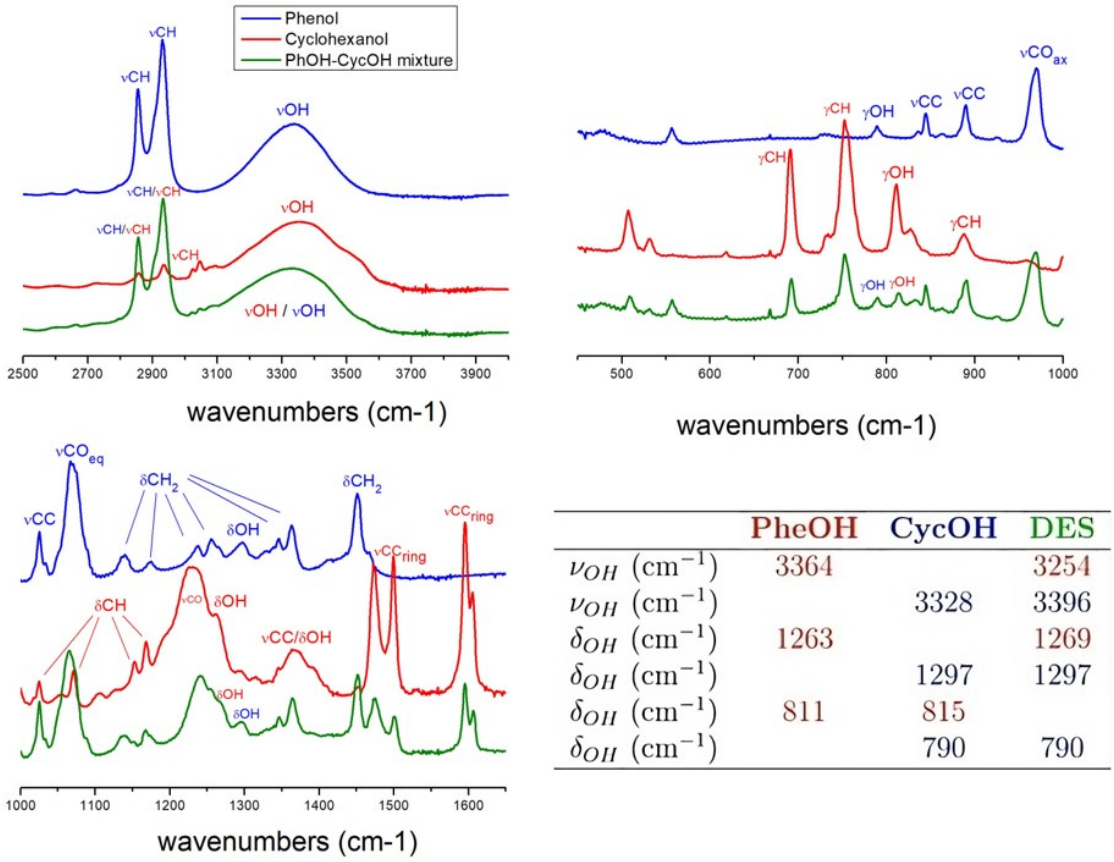

	PheOH	CycOH	DES
ν_{OH} (cm^{-1})	3364		3254
ν_{OH} (cm^{-1})		3328	3396
δ_{OH} (cm^{-1})	1263		1269
δ_{OH} (cm^{-1})		1297	1297
δ_{OH} (cm^{-1})	811	815	
δ_{OH} (cm^{-1})		790	790

Figure 4.31: Experimental infrared spectra

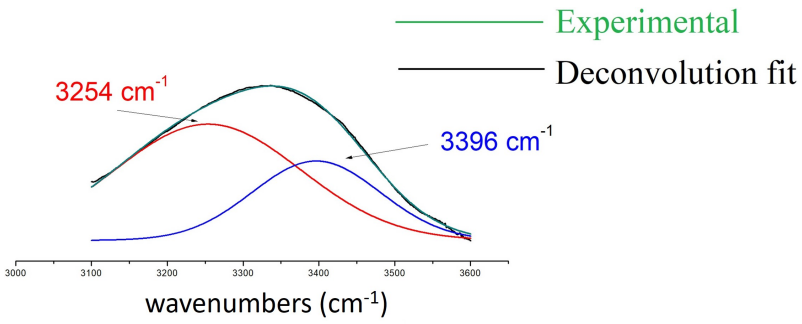

Figure 4.32: Deconvoluted OH stretching band of the PheOH-CycOH mixture IR spectrum

actions, necessarily omitting the other factors that contribute to the formation and stabilization of the liquid phase (van der Waals, π-π stacking, etc.). As demonstrated in the examples of the other DES described in the previous paragraphs, an investigation of this kind can be carried out through a combined theoretical-experimental approach. This involves conducting wide-angle X-ray diffraction measurements and comparing the structure functions I(q) with those obtained from molecular dynamics calculations. Both experimental and theoretical curves (figure 4.33 are dominated by the main peak at about 1.4 $\mathring{A}^{-1}$ which correlates with distances at about 4.5 $\mathring{A}$ due to several intermolecular terms that mainly involve the C$\cdots$C contributions. A second weaker peak at about 3.2 $\mathring{A}^{-1}$ correlates with distances at about 2 $\mathring{A}$ in the direct space due to intramolecular contacts. We observe good agreement for the primary peak arising from intermolecular contributions (1.4 $\mathring{A}^{-1}$) and for the remaining pattern. However, the accuracy of the theoretical simulation decreases for the X-ray diffraction curve at low q values. The X-ray curve also reveals a small prepeak at approximately 0.5 $\mathring{A}^{-1}$, which is barely discernible in the theoretical simulation. The presence of a prepeak situated at q values below 1 $\mathring{A}^{-1}$ has been interpreted as evidence of medium-range order, attributed to the presence of heterogeneities or clustering phenomena induced by hydrogen bonding [109, 110]. This phenomenon was also documented in 1:1 Thymol-Menthol mixtures, where the rings of menthol and thymol hinder the development of an extensive network of hydrogen bonds. This allows molecules to aggregate into small, hydrogen-bonded clusters ([111]). Moreover, there is a significant probability of oligomer formation, which may include molecules of thymol, menthol, or a combination of thymol and menthol, particularly in a liquid with equimolar composition. In our mixture of PheOH and CycOH, X-ray diffraction and MD simulations were conducted at the eutectic composition. Here, cyclohexanol is present in a substantial excess, and its ring does not have any alkyl substituents that might promote clustering phenomena. This is fully confirmed by the analysis of the intermolecular contacts through the calculation of the radial distribution function (g(r)). Self-association of PheOH and CycOH, as described through the g(r) of the O$\cdots$O contacts (figure 4.33a), highlights that interactions among cyclohexanol molecules, being the most abundant component, clearly dominate

over those between phenol molecules. Furthermore, the relative peak is sharper and observed at a shorter distance. This is consistent with the fact that hydrogen bond between CycOH molecules is stronger than that between PheOH molecules, in agreement with the geometries of the tetramers discussed in the previous section. The presence of hydrogen bonds between different components is clearly indicated by the O(CycOH)$\cdots$O(PheOH) peak, which occurs at distances quite similar to that of the O(CycOH)$\cdots$O(CycOH) peak. The nature of the O(CycOH)$\cdots$O(PheOH) intermolecular contact is further elucidated by the RDFs of the H$\cdots$O distance shown in figure 4.33b: the peak corresponding to the OH(PheOH)$\cdots$O(CycOH) distance is sharper and more intense than that of the OH(CycOH)$\cdots$O(PheOH) distance. This aligns with the fact that the oxygen of PheOH acts as a more effective hydrogen bond donor, as previously observed in the geometry of the heterotetramer in figure 4.28. A particularly convenient way to study the relative orientations of the two rings of the components in the mixture is to calculate the radial distribution functions between their center of mass positions. We observed that the CycOH-CycOH peak was relatively symmetrical and centered around 6Å . The PheOH-PheOH and CycOH-PheOH peaks exhibited maxima at very similar distances, with a slight shoulder at lower values (approximately 5Å). This subtle asymmetry could have arisen from the fact that PheOH, being a planar molecule, might have approached CycOH more closely than CycOH approached PheOH. The low concentration of phenol in the mixture at the eutectic composition, coupled with the absence of peaks at around 4Å in the center of mass RDFs, seemed to rule out any $\pi - \pi$ interaction between the benzene rings.

Structural characterization of deep eutectic solvents: discussion

The results described in this chapter demonstrate that the studied systems exhibit a strong propensity to interact, forming a dense network of intermolecular hydrogen bonds. Examining the type III-DESs provided in this chapter it becomes apparent that, despite the chemical, physical and structural distinctions among the starting materials, some common features can be identified. In these ionic DESs, the anion assumes the role of hydrogen bond acceptor and is coordinated by the

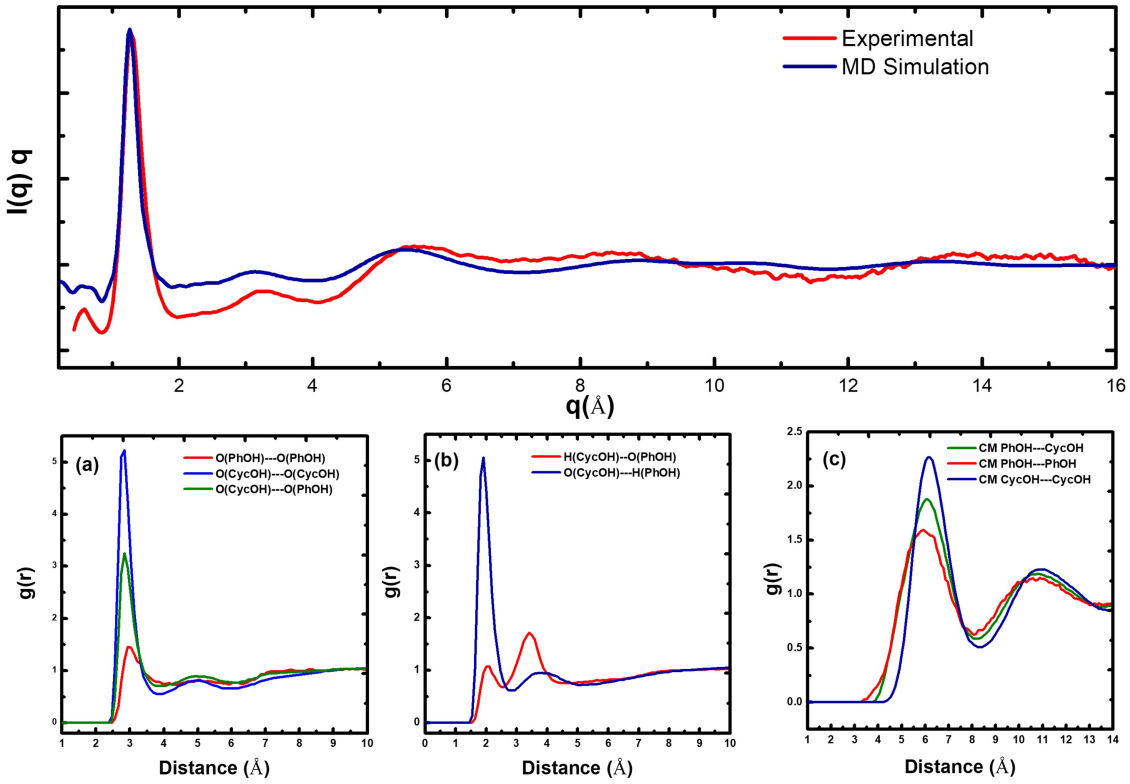

Figure 4.33: Upper panel: Experimental and theoretical $I(q) \cdot q$ curves of the PheOH-CycOH mixture at eutectic composition. Bottom panel: RDFs of the O$\cdots$O (a) and OH$\cdots$O (b) distances and RDFs of the centre of mass positions (c).

HBD through strong H-bonding interactions: this coordination does not deeply alter the geometry of the ionic couple, as observed by spectroscopic results and confirmed by all the computational models here presented. In the systems where the HBD consisted of molecules with multiple HBD groups (as in the case of acetate-based systems, where polyfunctional organic acids were chosen on the basis of number and chemical properties of the OH groups), the donation of H-bonds preferably occurs from the more acidic proton, aligning with the acid-base theory, as indicated in the definitions proposed by the IUPAC[90]. In any case the structures formed in the liquid phase see the anion bridged coordinated between the HBD and the cation. The notable structural differ-

ences between the two cations here studied (cholinium and tetrabutylammonium) manifest in the microscopic properties of the liquids: various spectroscopic and computational results clearly reveal that the TBA-based systems are more disordered than cholinium ones. As an example, X-ray diffraction results of TBABr-IM show the presence of pre-peaks: these pre-peaks are indicative of a substantial separation of alkyl segments, resulting in the formation of localized regions of inhomogeneity. This increased microscopic complexity is also reflected in the macroscopic properties, as evident from the thermal profiles (DSC) measured for the TBA-based systems and in particular for TBA-acetate. Indeed, when comparing mixtures composed by the same acid with choline acetate and TBA acetate, it is observed that the thermograms for the TBAAc-based systems exhibit a more complex thermal profile: this includes transitions related to processes like cold crystallization and melting, which are not observed in the samples with choline acetate. Hence, after assessing the similarities and distinctions among the previously described systems, we sought to understand the nature of interactions in the liquid phase for systems where both components are neutral (Type V DES). As known from the literature, these systems exhibit a significant deviation from the ideal thermodynamic behaviour: the most important example of this non-ionic deep eutectic solvents is the thymol-menthol eutectic mixture. In order to investigate how the interactions between these molecules lead to the formation of a deep eutectic, we considered a system composed of non-substituted structural analogues of thymol and menthol. It is important to note that thymol and menthol have alkyl groups attached to both rings. From the experimental phase diagram, it can be observed that the obtained eutectic composition does not deviate from the thermodynamic ideality condition. This indicates that the alkyl substituents on the rings play a key role in the spatial organization of the components in the liquid bulk. For these reasons, following similar approaches to those described for other systems, we conducted a structural characterization of the eutectic composition and its starting components. Despite the structural differences between the components of Type III and Type V DES, our analyses led to the identification of numerous similarities between the two types of systems. Once again all experimental results point towards a dense network of hydrogen bonds however, the hydrogen

bonding interactions in the mixtures here proposed are not sufficient to produce deviations from ideality. The alkyl substituents on thymol and menthol provide an additional stabilizing factor due to the establishment of van der Waals interactions. The provided example highlights the crucial importance of conducting a thorough structural characterization. This is fundamental because the microscopic properties are affected by the specific geometries assumed by the components in the liquid phase, which can directly influence their thermal properties. Consequently, it becomes clear that a comprehensive understanding of the structures and mechanisms governing the formation of these liquid phases allows us to effectively customize the properties of these liquids. This, in turn, enables us to refine and optimize these systems for the specific practical application required.

Chapter 5

Adsorption of ionic liquids on graphene surfaces

In the previous chapter we thoroughly discussed the structural characterization of pure deep eutectic solvents. Recently, the scientific community has increasingly focusing on studying the interactions of ionic liquids and deep eutectic solvents with nanomaterials, such as pristine graphene and its derivatives, carbon nanotubes and fullerenes[23, 24, 21, 22]. These nanomaterials are frequently at the foundation of technological applications: they are often used in energy storage systems, catalytic applications, as well as in the fabrication of membranes and sensors[12, 24, 112],. Many applications also involve the chemical absorption properties of pollutants and greenhouse gases. Perhaps one well-known application of these systems relates to the development of innovative electrochemical devices, such as in the realization of unconventional electrodes, electrolytes, or actuators (bucky gels, a physical gel obtained by a mix of nanotubes and ionic liquids[113, 114]). We focused on studying the adsorption properties of liquid systems capable of adsorbing polluting gases like CO_2 on structural derivates of graphene. To reduce the complexity of the studied systems, we initially proposed an investigation of the interaction of a bio-ionic liquid composed of Choline cation [Ch] and Phenylalanylate anion [Phe] with polyaromatic hydrocarbon-shaped graphene (N-pyridine graphene). Such liquid shares numerous chemical-physical properties with

deep eutectic solvents and possesses a less complex structure (1:1 stoichiometric ratio, without the presence of the hydrogen bond donor). As previously investigated [19], the chosen ionic liquid exhibits a remarkable capacity to react with polluting gases, making it an excellent CO_2 scrubber as it is economical, environmentally friendly and noticeably reactive. The surface was chosen with the aim of providing a significant aromatic portion able to interact with the [Phe] anion and a surface portion with polar sites (namely, pyiridinic holes) that can adsorb the [Ch] cation. The idea, therefore, was to first examine the structure formed by interaction between the liquid and a N-doped graphenic surface. Then, to assess whether the interactions with the surface can affect the thermodynamics of the CO_2 fixation reaction. The structural characterization and the study of reaction mechanisms were conducted using a computational approach, involving classical molecular dynamics simulations and DFT calculations.

5.1 ChPhe ion pair adsorbed on graphene surface

The adsorption of [Ch][Phe] on N-doped graphene surface was investigated using two computational approaches. This included the proposal of several scaled-down calculation models to investigate the interactions of individual ion pairs on graphene in detail. A particular focus was on the evaluation of interaction energies and charge transfer processes at the quantum mechanical level (DFT). Then the interaction between ionic species and the graphene surface was further investigated by means of molecular dynamics simulations, considering a graphene sheet immersed in a liquid bulk.

Structures from DFT

The choline phenylalanylate ionic liquid can adsorb onto the graphene surface through multiple interaction sites, involving cations, anions, or ion pairs, resulting in a diverse range of adsorption structures. We initially proposed two Polycyclic Aromatic Hydrocarbons (PAHs) as models to illustrate the interaction of [Ch][Phe] with graphene: $C_{42}H_{16}$ (figure5.1a) serves as a model to

represent the interaction of [Phe] anions with an unmodified graphene surface, while $C_{33}H_{15}N_3$ (figure5.1c) is a compact yet suitable model for simulating the interaction of an N-doped graphene surface with [Ch] cations. In the optimized $C_{42}H_{16}$[Phe] structure (figure 5.1b), the phenyl ring

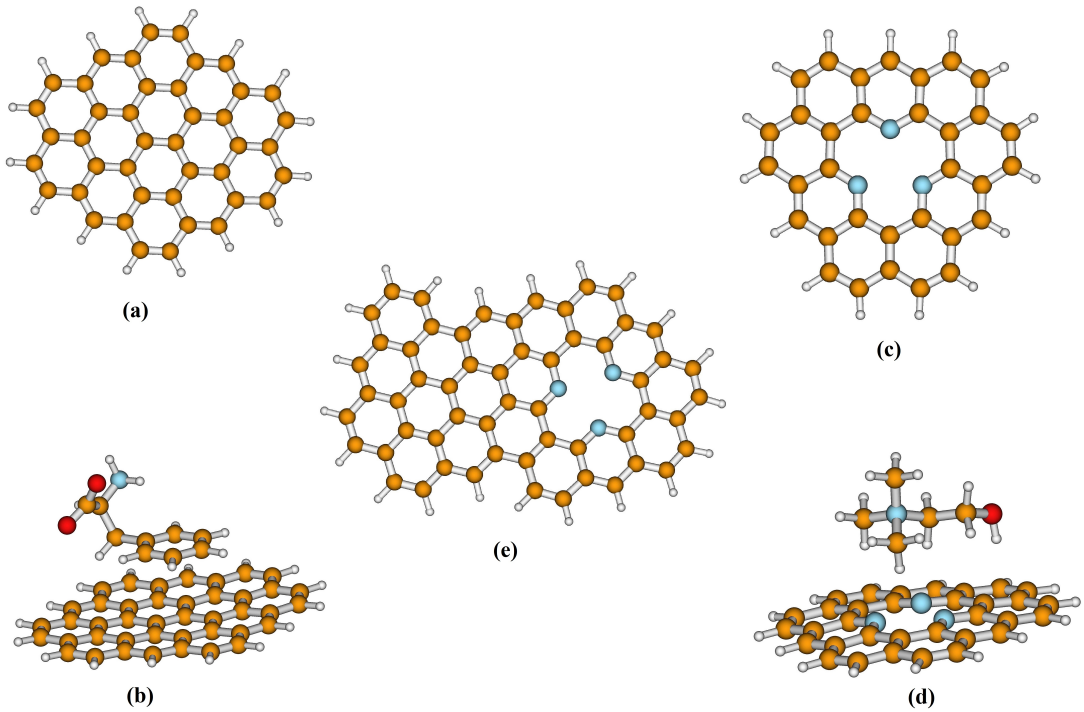

Figure 5.1: Structures of $C_{42}H_{16}$ (a) and $C_{42}H_{16}$ interacting with the [Phe] anion (b), $C_{33}H_{15}N_3$ (c) and $C_{33}H_{15}N_3$ interacting with the [Ch] cation (d), and structure of N-doped graphene model (e)

of [Phe] maintains its initial parallel alignment with the graphene plane. The average $C\cdots C$ distance measures approximately 3.554 Å, which is indicative of a typical $\pi - \pi$ stacking distance. Regarding the optimized geometry of $C_{33}H_{15}N_3$ (5.1d), the N-doped site serves as an interaction site for the polar heads of the [Ch] cations. The arrangement reveals that a methyl group of [Ch] is directed towards the center of the $C_{33}H_{15}N_3$ system, particularly the N-pyridinic vacancy. The binding energies (E_{ads}), computed as difference between the energy of the complex and the energies of the separated ionic species and graphene, reported in table 5.1, indicate that cations and

anions are physically adsorbed on the graphene models. The presence of an aromatic portion on the anion causes $\pi - \pi$ interactions with the aromatic part of $C_{42}H_{16}$, which is the most important energetic contribution of anion adsorption. The N pyridinic vacancy of graphene drives the coordination of the [Ch] cation through CH$\cdots$N interactions. In figure 5.2 we showed two different

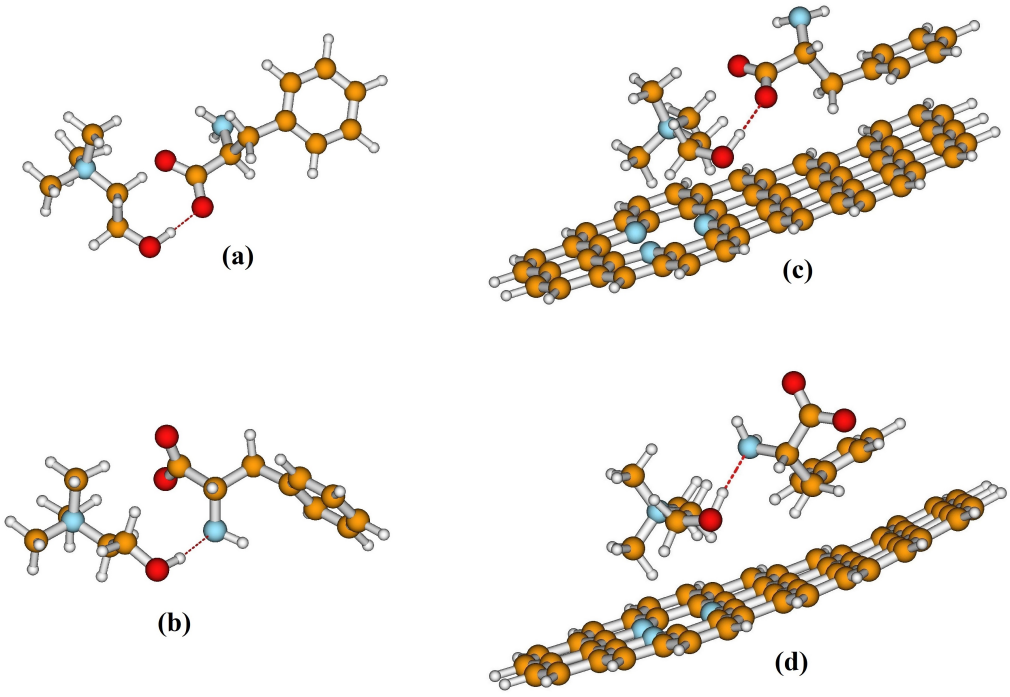

Figure 5.2: Structures of $C_{42}H_{16}$ (a) and $C_{42}H_{16}$ interacting with the [Phe] anion (b), $C_{33}H_{15}N_3$ (c) and $C_{33}H_{15}N_3$ interacting with the [Ch] cation (d), and structure of N-doped graphene model (e)

configurations of ion pair, in which the hydroxyl of choline coordinates the carboxylate group by OH$\cdots$O bond (a) and the amino group by OH$\cdots$N bond. Although the OH$\cdots$O bond is shorter (1.662 Å) than OH$\cdots$N (1.783 Å), the structure (b) resulted more stable by 13 kJ/mol. This slight stabilization is due to a different strength of the hydrogen bond as well as to a stronger electrostatic interaction and attractive dispersion term, as confirmed by the SAPT0 (Symmetry-Adapted

Perturbation Theory) calculation, which involves the decomposition into individual energy contributions to the total interaction energy [66, 67, 68]. [Ch][Phe] was then studied in presence of graphene by placing both structures on the plane of $C_{57}H_{21}N_3$ (figure 5.1e): we oriented the [Phe] anion with the phenyl ring on the pristine graphene zone, with the positive head (Ch^+) placed up to the N-pyridinic vacancy. Firstly, it is interesting to observe that the length of the hydrogen bond connecting cation and anion in ion pair increases upon adsorption: $OH\cdots O$ distances goes from 1.662 Å in the pure IL to 1.741 Å when adsorbed on the graphene: this suggested that the adsorption on the surface slightly destabilizes the strength of the interactions. On the contrary, when cation and anion interact by $OH\cdots NH_2$ bond, the stability of pair seems to be less affected by adsorption since the hydrogen bond distance undergoes a very small contraction from 1.783 Å to 1.755 Å. These results implies that the formation of ion pairs, which is prevalent in the bulk IL, may still occur even when the species are adsorbed on graphene. The values outlined in table5.1 affirm that physisorption on graphene could involve both individual ionic species and ion pairs. However, the binding energy of the [Phe][Ch] on graphene is notably lower than the sum of the adsorption energies of the [Ch] cation (figure 5.1d) and the [Phe] anion (figure 5.1d). This result suggests therefore that ionic coupling perturbs the electron properties of the cations and anions and consequently changes the extent of their adsorption on graphene surfaces.

Noncovalent interactions and charge transfer

To assess how the adsorption of the ionic liquid on graphene influences the charge distribution, we performed the Electron Density Difference (EDD) analyisis for the adsorbed species. The EDD is defined by the equation:

$$\Delta\rho(r) = \rho(r) - [\rho_{graphene}(r) + \rho_{ion-pair}(r)] \tag{5.1}$$

where $\rho(r)$ represents the electron density of the entire system, which includes N-doped graphene with the adsorbed ion pair. $\rho_{graphene}(r)$ is the electron density of the N-doped graphene,

and $\rho_{ion-pair}(r)$ is the electron density of the ion pair. The results of the EDD analysis are reported in figure 5.3. By the comparison of the EDD isosurfaces we can deduce that both the anion

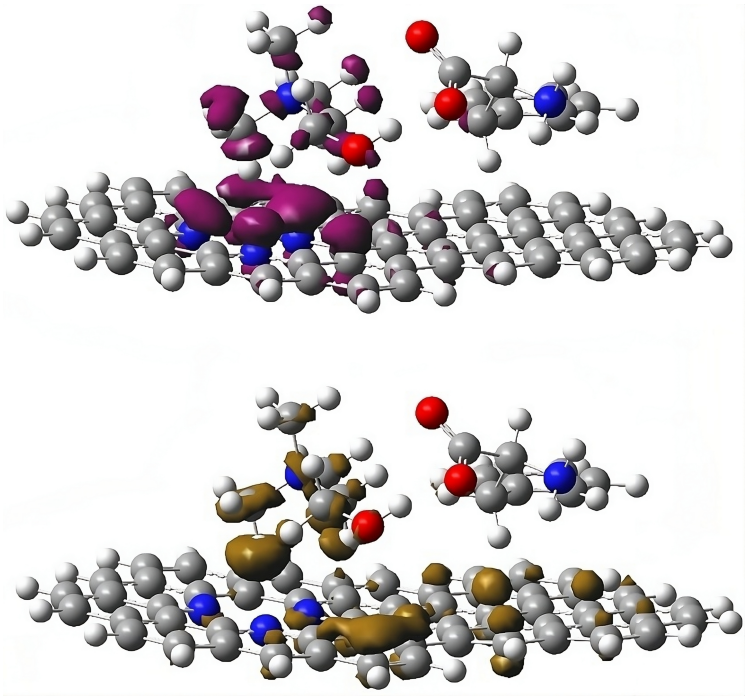

Figure 5.3: Electron Energy Difference (EDD) analysis of graphene-ion pair system: increases are reproduced in olive and depletions in purple

and cation alter the charge distribution on graphene. The electron density on graphene surface decreases in the zone of the interaction with the cation and a slight increase was observed in the region close to the anion. Based on the analysis, it is suggested that a small charge transfer can occur between the ion pair and the graphene sheet, with the positively charged head of the cation primarily involved in the process. To assess the respective contributions of the cation and anion to the charge transfer with graphene, we performed Bader charge analysis [64]. The charges of the cation, anion, and the graphene surface were determined by summing the charges of all the atoms in each unit before and after the interaction and the results were reported in table 5.1. In the case of a single [Ch] cation interacting with N-doped graphene a charge transfer of 0.078 e

occurs from graphene to the cation. Conversely, upon the adsorption of a single [Phe] anion a charge transfer from the anion to graphene ensues, albeit of a smaller magnitude (0.027 e). As expected, after the adsorption of individual ionic species, cations tend to diminish the electron charge of graphene, while anions make the graphene surface more negatively charged. The cation exhibits a more notable extent of charge transfer, despite the closely similar adsorption energies for both cation and anion, as indicated in table 5.1. We further evaluated the charge transfer in cases of ion pairing by comparing the charges of cations and anions before and after adsorption for both models depicted in figure 5.2

In absence of graphene, the ion pair depicted in figure 5.2b, where the interaction between [Ch] and [Phe] includes an OH$\cdots$NH$_2$ hydrogen bond, displays a charge transfer of 0.89 e between the cation and anion. This value closely resembles the charge transfer calculated for the ion pair in Figure 2a (0.904 e), where the interaction involves a hydrogen bond between the OH group of [Ch] and the carboxylate group of [Phe]. After adsorption of [Ch][Phe], the charge transfer between cation and anion is reduced because each ionic species exchanges electron charge with the graphene. Since, as indicated by the previous results, the charge transfer involving the cations are more consistent than those involving the anions, the adsorption of ion pair makes the graphene surface slightly positive. It is remarkable to note that the effect is more evident in the structure of Figure 2b; in this case the cation forms a OH$\cdots$N hydrogen bond weaker than the OH$\cdots$O bond formed in the alternative structure and probably it is more available to accept electron charge from graphene.

The role of Noncovalent Interactions (NCIs) in the adsorption was evaluated by reduced density gradient (RDG) analysis. Studying the electron density, denoted as ρ, along with its first derivatives, $|\nabla\rho|$, provides a method to assess non-uniformities in electron distribution and identify both weak and strong intermolecular interactions. In the low density region, where weak interactions are expected, the appearance of a peak indicates the presence of non covalent interactions. The study of the Laplacian of density $\nabla^2\rho$ and the sign of the second of its eigenvalues (λ_2) is a valid method for distinguish van der Waals, hydrogen bonding (negative sign) and steric

Table 5.1: Charge, q(e.u.), of cation, anion and graphene before and after adsorption and its variation, Δq, induced by adsorption. Adsorption energy (E_{ads}) of cation, anion and ion pair on the graphene models.

	q(before)	q(after)	Δq	E_{ads}(kJ/mol)$^{(a)}$
[Ch] + N-doped graphene				
[Ch]	1.000	+0.922	+0.078	
Graphene	0.000	+0.078	-0.078	-74 (-59)
[Phe] + Graphene				
[Phe]	-1.000	-0.973	-0.027	
Graphene	0.000	-0.027	+0.027	-85 (-74)
[Ch][Phe]$^{(b)}$ + N-doped graphene				
[Phe]	-0.904	-0.896	-0.008	
[Ch]	+0.904	+0.867	+0.037	
Graphene	0.000	+0.029	-0.029	-129 (-103)
[Ch][Phe]$^{(c)}$ + N-doped graphene				
[Phe]	-0.892	-0.888	-0.004	
[Ch]	+0.892	+0.847	+0.045	
Graphene	0.000	+0.041	-0.041	-119 (-95)

$^{(a)}$ Values in parentheses are corrected for BSSE; $^{(b)}$ Structure of figure 5.2a; $^{(c)}$ structure of 5.2b.

repulsion interactions (positive sign)[115]. The red and green regions represent strong and attractive van der Waals interaction and the blue ones represent the hydrogen bond. The RDG scatters and NCI surfaces were computed for a single anion, single cation and both the proposed structures of ion pair, as reported in figure 5.4. Regarding the interaction between the cation and anion in the ion pair, the spike observed at a significantly negative value (-0.04 e) signifies the establishment of a robust hydrogen bond. In the structure reported in figure 5.2a the analysis showed that the red and green spikes are close to zero, indicating very weak interactions. However, in

the structure of 5.2b, there is a noticeable green region, suggesting the existence of van der Waals interactions between the methyl groups of [Ch] and the phenyl ring of [Phe]. This observation aligns with the SAPT decomposition analysis discussed earlier. The adsorption of cation and anion involves extensive regions with van der Waals interactions. In particular, the interactions of the cations involve mainly hydrogen atoms of cations and carbon and nitrogen atoms of graphene; adsorption of the anions occurs instead through interactions of carbon atoms of the phenyl ring and carbon atoms of graphene. All these interactions are shown by the green regions in the NCI plots reported in figure 5.4. The adsorption of the ion pair on the graphene surface involves again van der Waals interactions between carbon and nitrogen atoms of graphene and hydrogen and oxygen atoms of the cation and carbon atoms of the phenyl ring of the anion. The blue spikes found in the NCI plots reported in figure 5.5 indicate that hydrogen bonding continues to be the main cause to stability of the ion pair before and after adsorption on graphene.

Structures from MD simulations

The calculations described so far allowed for a detailed investigation into the interactions of the cation, anion, and ionic pair with the graphene surface. However, it is clear that, in order to better characterize the structure formed by the interaction of the liquid with the surface, the DFT calculations we have proposed so far involve models that are too small. After elucidating the electronic process governing the interaction of the ionic liquid with the graphene surface at DFT level of theory, we opted to increase the dimension of the graphene model. Specifically, we decide to simulate 1000 ion pairs on a surface measuring approximately 37Å $\cdot$ 57Å, consisting of four pyridinic subunits placed at the center of a cubic box surrounded by ionic pairs. The distribution of cations, anions and their association products was analyzed by means of the radial distribution functions (RDFs), as reported in figure 5.6. The RDF for the hydroxyl hydrogen of choline and the oxygen atoms of the carboxylate group (figure 5.6a) exhibits a pronounced peak at approximately 2 Å, indicating a strong hydrogen bonding between cations and anions in the liquid. Figure5.6b displays the distribution of distances between the hydrogen atom of the OH group in choline and two

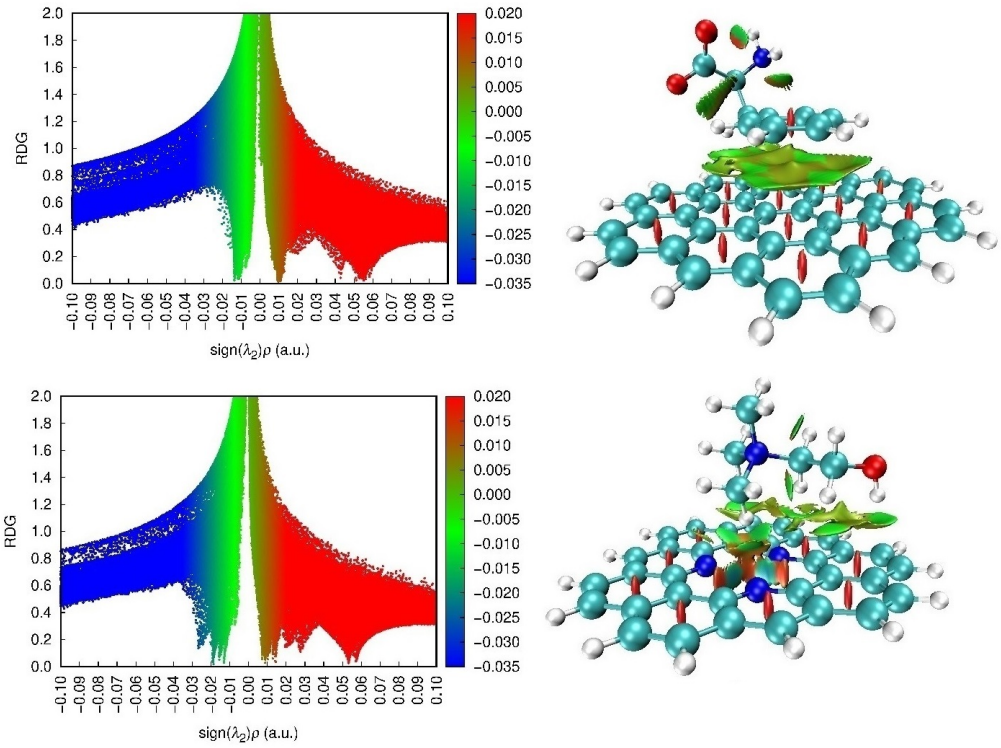

Figure 5.4: NCI isosurfaces and scatter plot using promolecular density for [Ch]-Graphene, [Phe]-Graphene (isosurface=0.5)

oxygen atoms of the CO_2^- group. This plot emphasizes that the O···HO interactions are mainly centered on a single oxygen, with configurations where OH is bonded to both oxygen atoms of the carboxylate being infrequent. The RDFs for the choline nitrogen around the CO_2^- group represented in figure5.6c reveal significant peaks at around 5 Å, suggesting potential direct interactions between the polar heads of cations, $N(CH_3)_3^+$, and anions, CO_2^-. The RDF of the nitrogen in the NH_2 group of [Phe] and the hydroxyl hydrogen of choline (figure5.6d) displays moderately intense peaks at approximately 2 and 5 Å, indicating that the association between cations and anions seldom involves OH···N hydrogen bonds. Consequently, the potential used in our simulations suggested that ions in the liquid are primarily connected by OH···O interactions.

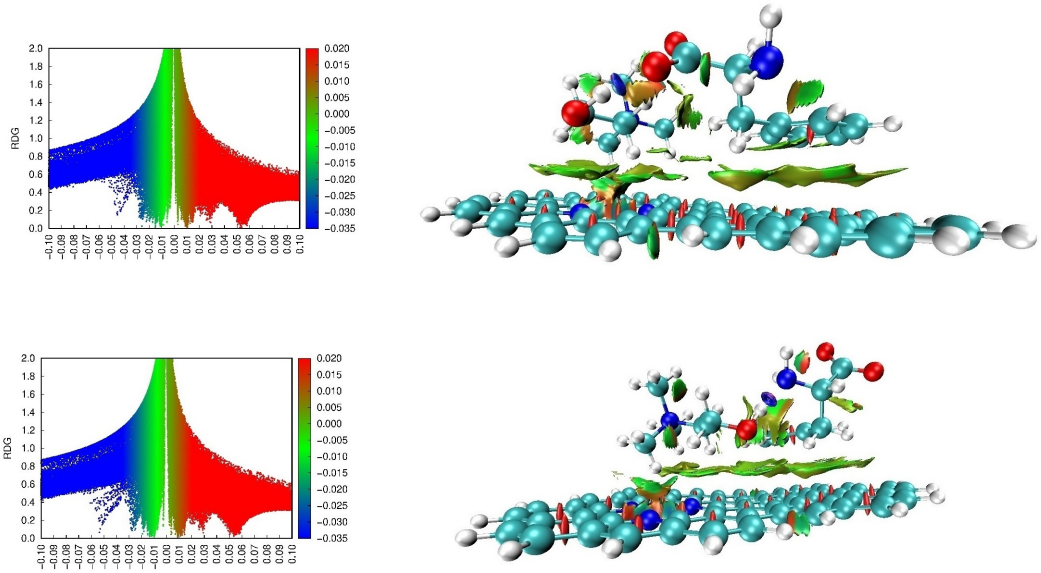

Figure 5.5: NCI isosurfaces and scatter plot using promolecular density for [Ch][Phe]-Graphene (isosurface=0.5)

Alternative structures bonded through OH$\cdots$N interactions, as localized by DFT calculations, appear to be quite improbable in the liquid phase. . The results of the analysis of the interaction between cation and anion with the N-doped graphene sheet were reported in figure 5.7. The arrangement of [Phe] anions in relation to the graphene surface was initially suggested by the RDF between the center of mass of the graphene sheet and the center of the phenyl ring of the [Phe] anion, as visible from 5.7a.The plot displays a prominent peak at approximately 5 **Å**, corresponding to the distance between phenyl rings and the graphene surface, that it appears to be significantly greater than the value of 3.5 **Å** determined by our static models via DFT calculations. The inclusion of dynamic effects in MD simulations undoubtedly contributes to the increased interaction distance between phenyl rings and graphene. To understand the orientation between tha plane of the graphene and that of the phenyl ring we studied the the combined distribution function curve (CDF) of figure 5.7 where the angular distribution function (ADF) between the plane of the

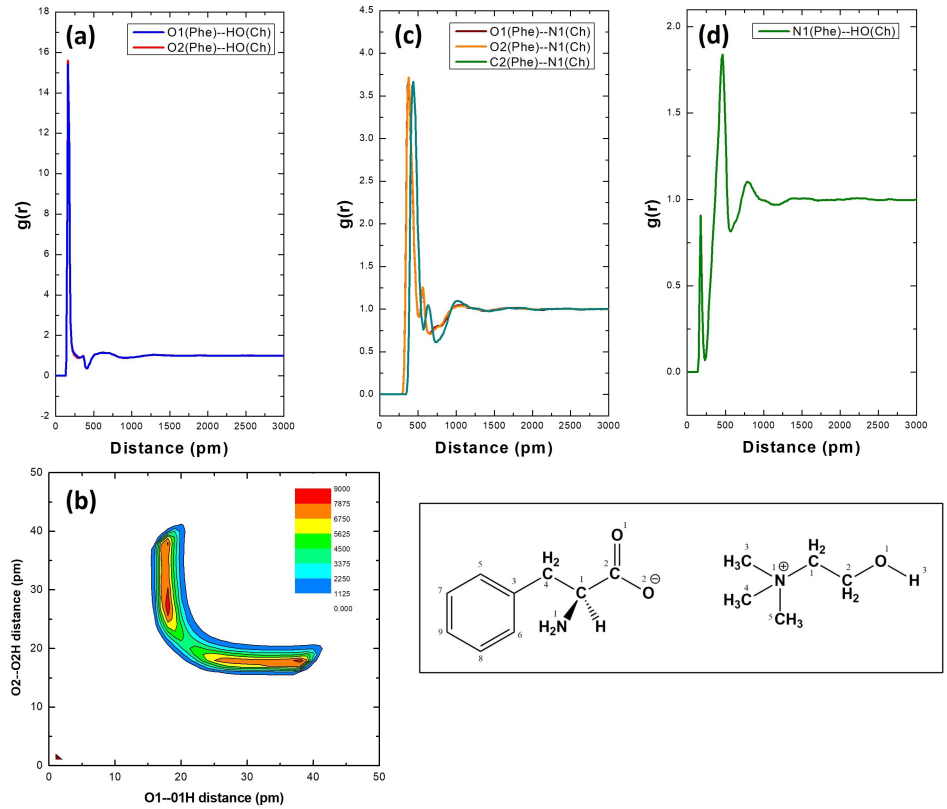

Figure 5.6: Radial distribution functions of $r(\mathrm{O}\cdots\mathrm{HO})$, (a), distance between oxygen of the CO_2^- group and hydrogen of the OH group of [Ch] and plot of the distances $r(\mathrm{O}_1\cdots\mathrm{HO})$ vs. $r(\mathrm{O}_2\cdots\mathrm{HO})$ where O1 and O2 are the oxygen atoms of the CO_2^- group of [Phe] (b). Radial distribution functions of $r(\mathrm{O}\cdots\mathrm{N})$ and $r(\mathrm{C}\cdots\mathrm{N})$ (c), distance between nitrogen of [Ch] and oxygen of [Phe] and between nitrogen of [Ch] and carbon of CO_2^-, respectively. Radial distribution functions of $r(\mathrm{N}\cdots\mathrm{HO})$ (d), distance between hydrogen of the OH group of [Ch] and nitrogen of NH_2 group of [Phe].

graphene and the plane of the phenyl ring is plotted against the rdf between the centre of the graphene sheet and the centre of the phenyl ring. The plot reveals that the ring of the anion is positioned at distances from the graphene plane ranging between 3.5 and 6 Å, assuming orientations that are fairly evenly distributed from 60 to 180 degree. A slight preference for a parallel

orientation appears to be observed at a distance of approximately 6 Å. The rdf between the centers of the phenyl rings 5.7, panel c, exhibits a prominent peak at approximately 6 Å, indicating an orthogonal orientation between the phenyl rings. This is corroborated by the plot in 5.7d, which illustrates the angular distribution function (ADF) between phenyl rings in conjunction with the distance between their centers. The cdf shows higher values for perpendicular orientations of the phenyl rings at distance of 6 Å. The absence of noteworthy $\pi - \pi$ stacking interactions in the bulk liquid phase was previously noted in analogous ionic liquids, such as choline salicylate, through X-ray diffraction experiments and MD simulations, utilizing the GAFF force field [116].

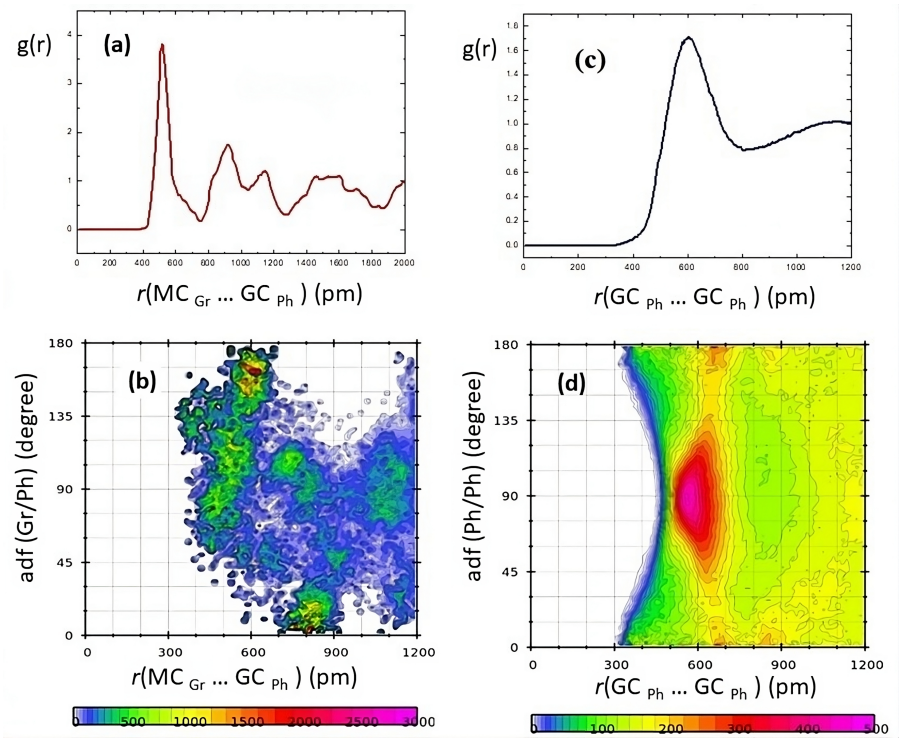

Figure 5.7: (a), RDF of the distance between the center of mass of the graphene sheet (MC_{Gr}) and the geometric center of the phenyl ring of [Phe] (GC_{Ph}); (b) CDF of the adf between the planes of the graphene sheet and the phenyl ring of [Phe], $adf_{(Gr/Ph)}$, and the rdf of the distance $MC_{Gr} \cdots GC_{Ph}$; (c) RDF of the distance between geometric centers of phenyl rings of [Phe], $GC_{Ph} \cdots GC_{Ph}$; (d) CDF of the adf between the planes of the phenyl rings of [Phe],$adf_{(Ph/Ph)}$, and the rdf of the distance $GC_{Ph} \cdots GC_{Ph}$;

5.2 Reaction of CO_2 with [Ch][Phe]

The results described in the previous section demonstrate a strong affinity of the liquid to adsorb onto the surface. Among the various applications of ionic liquids, particularly aminic ones, their ability to react with CO_2 has emerged. CO_2 is one of the most pollutant greenhouses gas, produced by many anthropic activities through the burning of fossil fuels such as coal, oil, and natural gas. Research on technologies to capture the large quantities of CO_2 emitted into the atmosphere

is increasingly capturing the attention of the scientific community. It is worth to investigate how the surface adsorption can affect the CO_2 affinity of ILs and within this aim we studied the reaction mechanism of CO_2 when the IL is adsorbed on the surface. The reaction mechanism can considered divided into two steps, as reported in the following scheme:

$$[\mathrm{Phe}]^- + CO_2 \longrightarrow [\mathrm{Phe}-CO_2]^- \longrightarrow [\mathrm{Phe}-CO_2-\mathrm{H}]$$

The first step, previously identified as the rate-determining step, involves the formation of a zwitterionic addition product between the anion and CO_2. The zwitterion adduct can undergo self-rearrangement through internal rotation, ultimately leading to the formation of a carbamate and a carboxylic acid. The mechanisms were studied in the liquid phase by considering the stability of the zwitterionic complex and the energetic barrier to its formation by a fully relaxed PES scansion along the C$\cdots$N distance. The thermodynamics and the transition states were evaluated in presence and absence of graphene by geometry optimization at the ωB97xd/6-311++G** level of theory. The vibrational frequencies were computed to univocally characterize each critical point. The intrinsic reaction coordinates (IRC[117]) were identified to verify that the saddle points really connected the corresponding reagents and products. As widely known[118], the interaction between AA anions and CO_2 entailed the participation of the amino group, initiating with the establishment of a N$-$C bond, resulting in the formation of a zwitterionic addition complex, subsequently denoted as [PheCO_2]. The addition of CO_2 to the [Phe] anion was initially examined by progressively shortening the C$\cdots$N distances while positioning a CO_2 molecule in proximity to the NH_2 group and optimizing the geometric arrangements. The potential energy profiles were obtained for both the isolated [Phe] as shown in figure 5.8a and [Phe] in the presence of choline cation, considering the ion pair coupled by an OH$\cdots$O hydrogen bond (figure5.8b). Following an initial physisorption, during which CO_2 interacts with [Phe] through van der Waals forces and maintains its linearity, the progressive approach of CO_2 leads to the formation of the [PheCO_2] adduct, with a C$-$N bond distance of approximately 1.6 Å. The reaction is exothermic, and the formation of the adduct is less favorable (24 kJ/mol) in presence of the choline cation compared to its absence (37 kJ/mol). To explore how the adsorption on the graphene surface might impact the

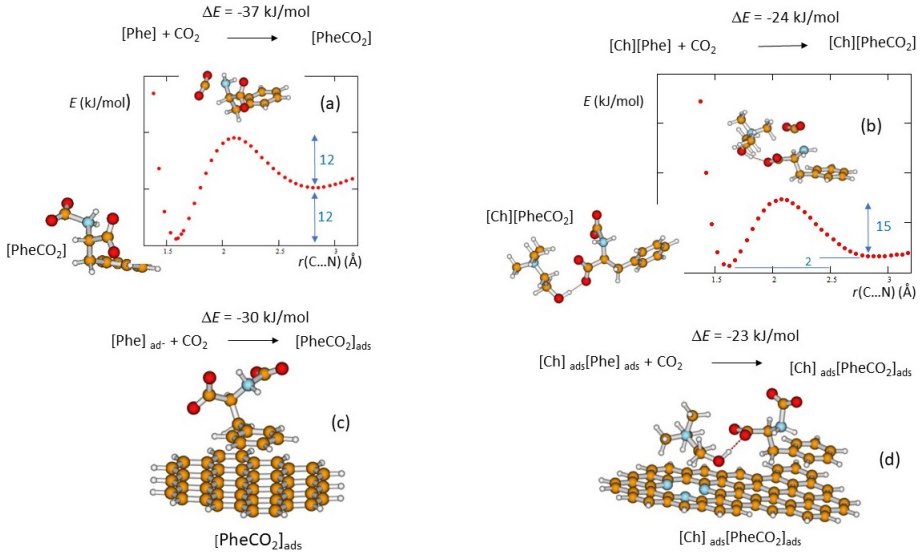

Figure 5.8: ωB97xd/6-311++G** PES calculated at various C$\cdots$N distances between CO_2 and [Phe] (a) and between CO_2 and [Ch][Phe] (b) and structure of the saddle points. Structures of the zwitterionic adduct [$PheCO_2$] (c) and [$PheCO_2$][Ch] (d) adsorbed on the graphene surface models and energy of reaction with CO_2. ΔE is calculated as $E_{[PheCO_2]ads}$ - (E[Phe]ads + ECO_2) (c) and as $E_{[Ch]ads[PheCO_2]ads}$ - ($E_{[Ch]ads[Phe]ads}$ + E_{CO_2}) (d)

CO_2 capture capacity of the phenylalanylate anion, we introduced the molecular systems shown in figure 5.8c and 5.8d. The structure in figure 5.8c, hereafter referred to as [$PheCO_2$]ads illustrates the zwitterionic complex adsorbed onto the same graphene model employed for the adsorption of the [Phe] anion. On a graphene surface, the reaction between the [Phe] anion and CO_2 remains exothermic. Specifically, it releases 30 kJ/mol when the single anion (figure 5.8c) is adsorbed and 23 kJ/mol when the ion pair is adsorbed (figure 5.8d). This indicates that the ability of the [Phe] anion to chemically adsorb and capture CO_2 is not significantly impacted by its adsorption on graphene surfaces. Furthermore, this efficiency appears to be on par with what is expected in a bulk liquid environment. As previously studied[118], the zwitterionic complex [$PheCO_2$] can rearrange into carbamic derivatives through intramolecular mechanism. Specifically, a proton from the amino group can be transferred to one of the two carboxylate groups of [$PheCO_2$], re-

sulting in the formation of distinct carboxylic acids $PheCO_2H$. From our previously theoretical investigation[19] it was found that the proton transfer towards the newly added CO_2^- resulting from the reaction with CO_2 is exothermic. However, this process involves relatively high energy barriers due to the formation of transition states characterized by a cyclic structure with four atoms. We excluded this pathway, by focusing solely on the alternative pathway, which entails proton transfer to the other carboxylate group, resulting in the formation of $PheCO_2H$ via a five-membered transition state (TS). Although the reaction continues to be exothermic it exhibits a low activation energy. $PheCO_2H$, initially formed through intramolecular proton transfer, ex-

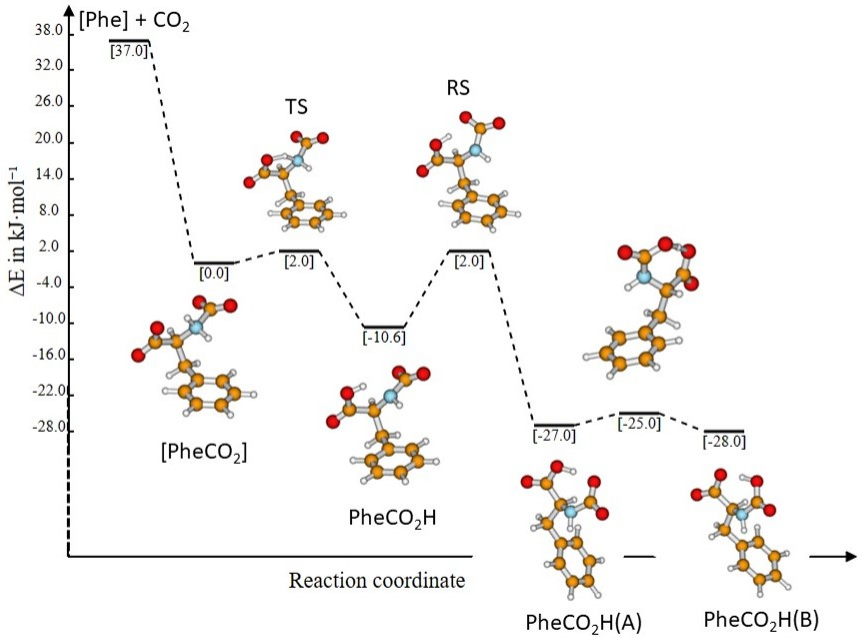

Figure 5.9: Energy profile of the conversion reaction of the zwitterionic complex $[PheCO_2]$ to carboxylic acid and structures of the stationary points along the reaction pathway

hibits rapid internal rotation about the C−C bond. This rotation, facilitated by the rotational transition state (RS), results in the formation of an intramolecular hydrogen bond between the carboxylic and carboxylate groups, yielding the stable isomer $PheCO_2H(A)$. The intramolecular hydrogen-bonded seven-membered cyclic structure enables facile proton transfer and the for-

mation of $PheCO_2H$(B), where the proton is situated on the second carboxylate group. Quick intramolecular proton transfer leads therefore to the formation of two isomers that have energies nearly equivalent and are found at about 28 kJ/mol lower than initial zwitterionic complex. The addition reaction of CO_2 to the [Phe] anion, followed by the subsequent intramolecular rearrangement, is exothermic, with a reaction energy of approximately 64 kJ/mol. In the case of [$PheCO_2$] adsorbed on the graphene surface, the zwitterion formed can interact via $\pi - \pi$ interaction with the surface, being the phenyl ring parallel to the graphene plane with an average distance of 3.494 Å. Once adsorbed (the adsorption energy is 65kJ/mol), $PheCO_2$ can be involved in a pathway of intramolecular proton transfer and rearrangement to give [$PheCO_2H$] products already proposed for [$PheCO_2$] in the liquid bulk. In addition, all the intermediate molecules and transitions states continue to be adsorbed to the graphene surface by $\pi - \pi$ stacking. The reaction product, [$PheCO_2H$], is once again strongly stabilized by intramolecular hydrogen bonding, facilitating rapid proton exchange between the neighboring carboxylate groups. The computed energetic landscape for the whole reaction in the liquid bulk closely resembles that computed on the graphene surface 5.10, although the transfer of a proton from the NH_2 group through the TS structure is more energetic. In summary, the reaction of the [Phe] anion with CO_2 and the subsequent rearrangement to produce carbamic derivatives is overall exothermic, albeit with a lower energy value (50 kJ/mol) compared to the bulk liquid (64 kJ/mol). This indicates that the adsorption of the anion on the surface may marginally diminish the CO_2 capture capacity of the phenylalanylate anion.

The impact of ion pairing on the process of intramolecular proton transfer and the ensuing rearrangement was assessed by examining various potential pathways. The scenario depicted in figure 5.11 may occur, for instance, if the zwitterionic adduct [$PheCO_2$] is initially generated in the liquid bulk and subsequently adsorbed onto graphene. The resulting ionic couple structure exhibith a geometrical conformation of [$PheCO_2$] that can facilitate the proton transfer from the NH_2 group towards the non-hydrogen bonded CO_2^-. The energy profile for intramolecular proton transfer suggests that the proton is effectively transferred from NH_2 to form the carboxylic acid,

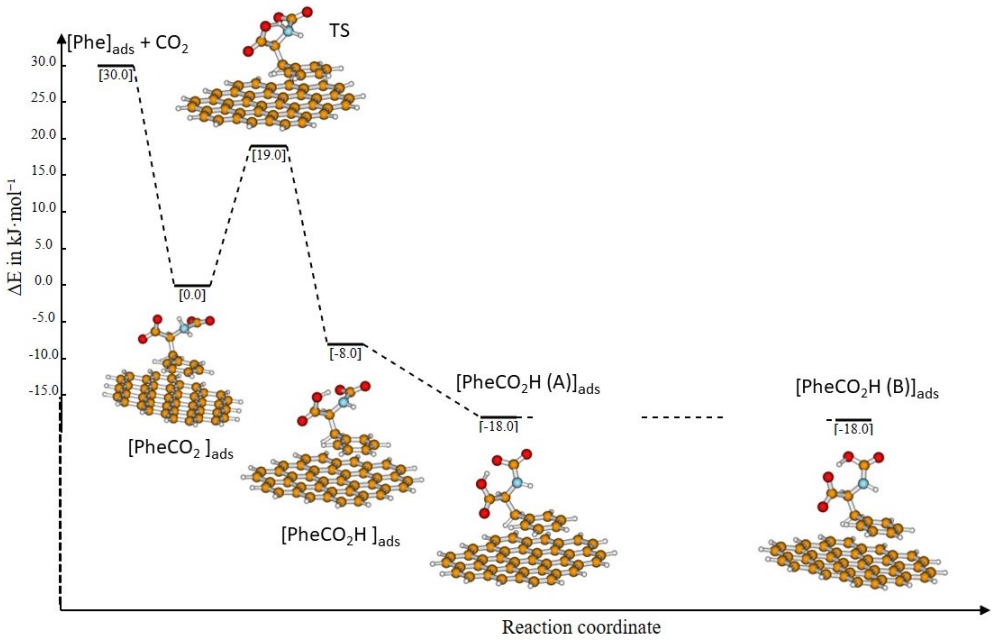

Figure 5.10: Energy profile of the conversion reaction of the zwitterionic complex [PheCO$_2$] adsorbed on graphene surface to carboxylic acid and structures of the stationary points along the reaction pathway

denoted as [Ch]ads[PheCO$_2$H]ads in figure 5.11, without a significant energetic barrier. A fast rotation of the CO$_2$H group to form intramolecular hydrogen bonding with CO_2^- not only stabilizes the product, but it also promptly leads to the formation of the isomer [Ch]ads[PheCO$_2$H(B)]ads without any intermediate [PheCO$_2$H(A)].

Discussion

The adsorption of ionic liquids onto the N-doped graphene surface was studied by means of DFT and molecular dynamics simulations. The structures of ionic liquids are in general simpler compared to deep eutectic solvents: this led to select the choline phenylalanylate (ChPhe) as the systems to study the interactions with N-doped graphene surface. All the computational results

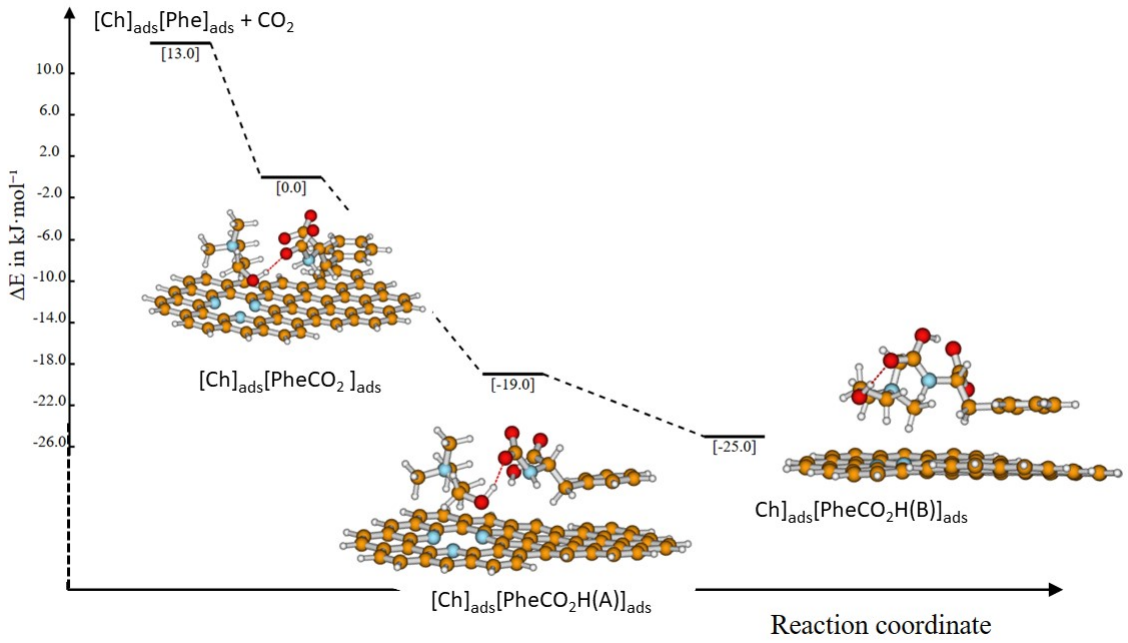

Figure 5.11: Energy profile of the conversion reaction of the zwitterionic complex [Ch][$PheCO_2$] adsorbed on graphene surface to carboxylic acid in presence of [Ch] cation

revealed that the ionic liquid is physisorbed, through van der Waals interactions between the phenyl ring of the anion and the surface: the parallel orientation of the phenyl rings with respect to pristine region of the graphene, suggested that the interactions occur predominantly via $\pi - \pi$ stacking. The cation, instead, coordinate mainly the N-pyridinic vacancy area through CH$\cdots$N contacts. The interaction between cations and anions leads to the creation of stable ion pairs via OH$\cdots$O or OH$\cdots$N hydrogen bonds involving the hydroxyl group of [Ch] and the CO_2^- or NH_2 groups of [Phe]. This ion pairing aggregation was observed both in the bulk solution and on the surface of graphene. By analyzing the electron density and the atomic charges before and after the adsorption on the graphene surface is possible to observe a substantial charge transfer which makes the graphene surface more negative. This effect is less pronounced when the adsorp-

tion involves the ion pair, as the charge transfer occurs simultaneously between cations, anions, and graphene. The MD simulations confirmed the results obtained by DFT characterization, although the introduction of dynamic models leads to the description of a more random orientation of the ionic couples onto the surface. These ionic couples are well supported on the surface of graphene: this enables these supported liquids to be used in numerous applications. One of these could be the chemi-fixation of pollulant gas, as CO_2. The initial product of addition of carbon dioxide and [Phe] anion sees the formation of a zwitterionic compound [PheCO_2], can give firstly the carboxylic acid [PheCO_2H] through an intramolecular proton transfer from the NH_2 group to one CO_2^- group. Subsequently, the intermediate [PheCO_2H] species may undergo a rapid interconversion into a more stable isomer, [PheCO_2H], facilitated by rotational rearrangement and intramolecular proton transfer between CO_2^- groups driven by intramolecular hydrogen bonding. The reaction was studied both in bulk phase and in the adsorbed species, considering the isolated anion and the ionic couple. All calculation were conducted by introducing an implicit solvation model (PCM). The overall reaction between [Phe] and CO_2 is consistently found to be exothermic across all cases. The inclusion of specific interaction with the choline cation gives a further decrease of the reaction energy suggesting that ion pairing of the graphene surface could slight inhibit the reaction with CO_2, as already observed in the bulk liquid [19]; the presence of choline appears to play a significant role in the structural rearrangement of the zwitterionic [PheCO_2] anion, as all the proton transfer processes are predicted to be barrierless.

Chapter 6

Conclusion

In this thesis we investigated different topics concerning physical and chemical properties of systems classifiable as soft matter. We focused our attention on the structural characterization of deep eutectic solvents and ionic liquids, pointing the attention on their microscopic organization. A great number of experimental and computational techniques has been employed to analyse the structure of pure deep eutectic solvents and to investigate the absorption of ionic liquids onto graphene surfaces. From an experimental point of view the microscopical structure of DESs was characterized by means of infrared and Raman spectroscopy. The IR spectra was acquired in medium (MIR) and, in some cases, far (FIR) regions, by measuring the spectra as a function of the temperature: FIR spectroscopy allows to directly observe the hydrogen bond vibrations. The IR spectra were assigned by comparing the experimental spectra with those obtained by DFT calculations. All the results reported in Chapter 4 show that the formation of liquid phases is mainly driven by the formation of strong H-bond between the HBD (imidazole or organic acids) and HBA (halide anions or acetate). In this thesis we proposed several systems where the cations, cholinium (Ch) or tetrabutylammonium (TBA), have a deeply different structure with the aim to modulate the nature and the strength of the interactions between components and vary the degree of order/disorder in the mixtures. These differences can be observed by DSC curves: the TBA-based systems, in fact, exhibit more complex DSC traces. To better investigate the molecular organiza-

tion in the bulk phases, we performed X-Ray diffraction measurements and molecular dynamic simulations: the choline-based liquids show a structural alternating pattern, as found in several ionic liquids. Indeed, the DES formulated with TBA are characterized of an additional interaction at longer distance-order, caused by the nano-segregation and clustering of the alkyl portions. Computational modeling reveals that hydrogen bonding can occur between all the donor groups, with a preference for the more acidic ones. Despite the profound differences in the starting materials, many similarities between Type III and Type V DESs were observed. In Chapter 5 we reported the principal results obtained by a computational investigation on the interaction of an aromatic amino-acid based ionic liquid, [Ch][Phe], with pyridinic-doped graphene sheets. Its adsorption on the graphene surface can occur through various interactions involving the cation and the pyridinic vacancies as well as the anion and the sp^2 carbon atoms of the graphene, establishing π-π interactions. The π-stacking was predicted by DFT models while less so by classic molecular dynamics simulations that describe a more random distribution of the cations and anions on the graphene surface. In the perspective of investigating the potential green application of this ionic liquid, its ability to adsorb CO_2, one of the greenhouse gases most emitted by anthropogenic activities, was explored. The reaction pathway was studied both in bulk and adsorbed liquid by means of DFT calculations. The initial product resulting from the addition of CO_2 to the [Phe] anion, specifically the zwitterionic [PheCO_2] anion, may undergo a sequential intramolecular reactions. The formation of the carboxylic acid [PheCO_2H] via an intramolecular proton transfer from the NH_2 group to one CO_2^- group is followed by a rapid interconversion into a more stable [PheCO_2H] isomer by rotational rearrangement and intramolecular proton transfer. The absorption on graphene, although it slight hinders the propensity of the ionic liquid to react with CO_2 compared to the bulk, can serve as an effective approach to support the liquid in preparation for potential practical applications.

Appendix

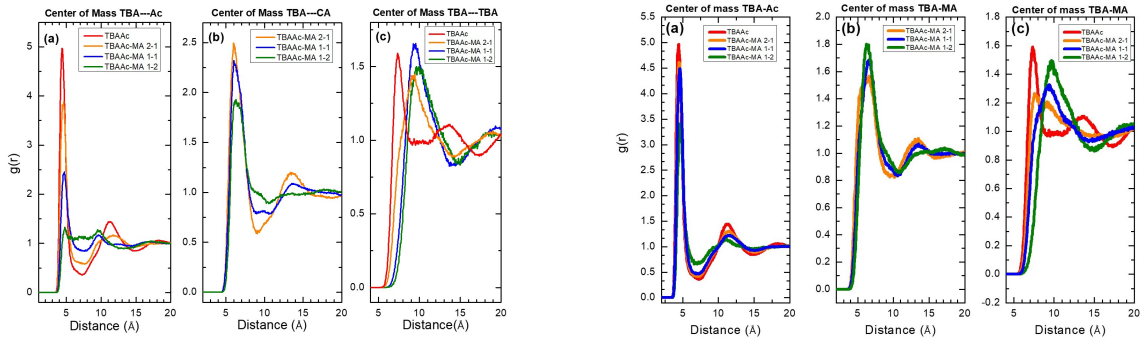

Figure 6.1: : g(r) computed between the center of mass of TBA and Ac (a), TBA and CA (or MA) (b) and TBA and TBA (c)

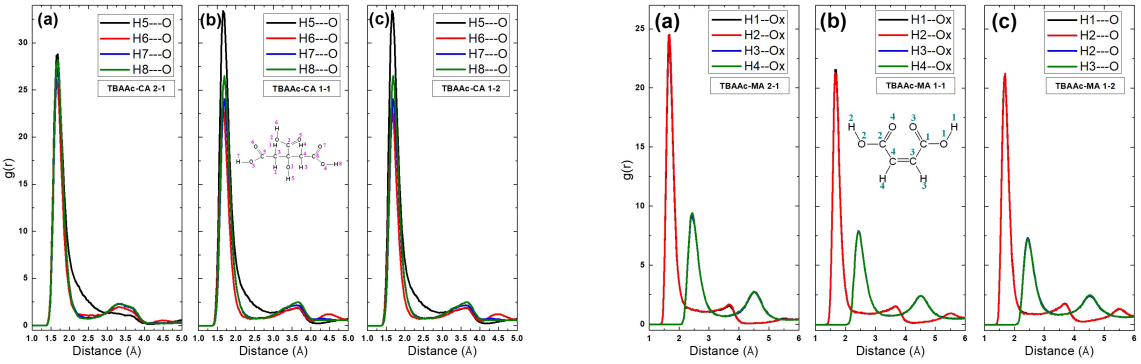

Figure 6.2: g(r) computed between the hydrogen atom (OH) of citric acid (left) or maleic acid (right) and oxygens atoms of acetate.

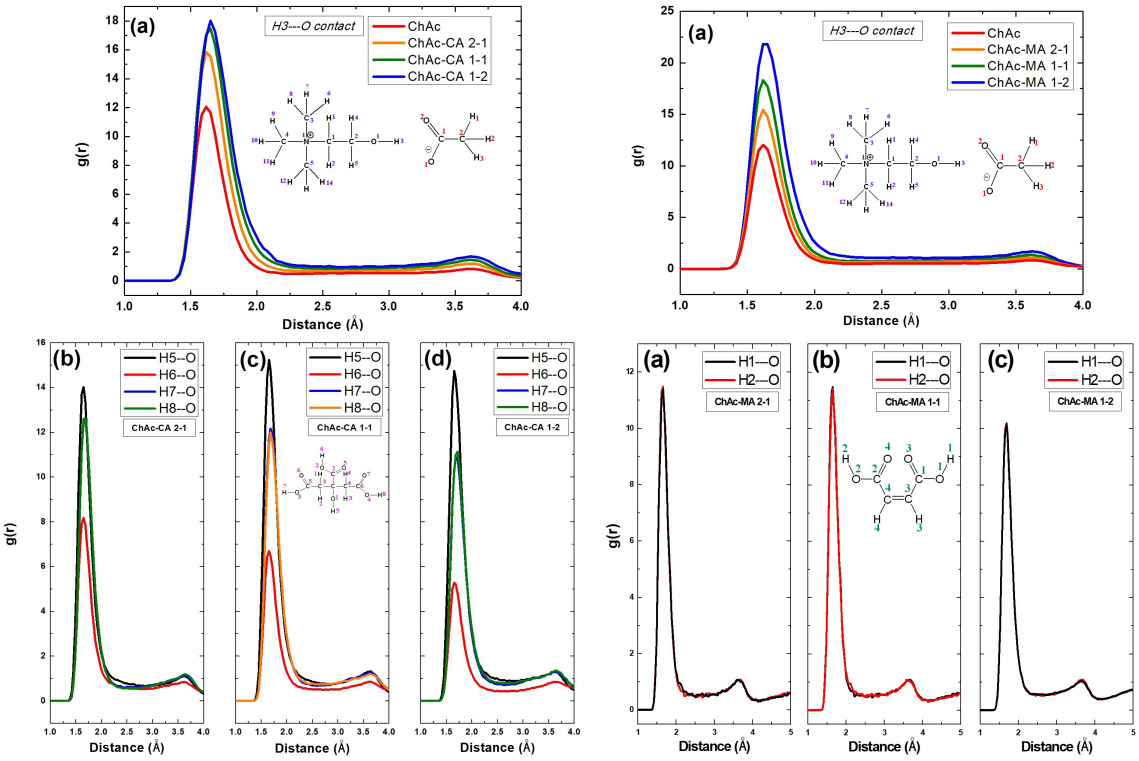

Figure 6.3: g(r) computed for ChAc-CA (left) and ChAc-MA (right) systems. Upper panels (a): distances between H3 (choline) and O (acetate). Bottom panels: distances between hydrogen atoms of CA (or MA) and O (acetate). (b) composition 2-1, (c) composition 1-1 and (d) composition 1-2.

Chapter 7

Pubblications and conference relations

7.1 Pubblications

Most of my works published in literature concerns topics described in this doctoral thesis. The complete list is:

- F. Ramondo, S. Di Muzio - **Adsorption of choline phenylalanylate on polyaromatic hydrocarbons shaped graphene and reaction mechanism with CO_2: a computational study**, Journal of Physical Chemistry A, 2023
- A. Paolone, S. Di Muzio, O. Palumbo, S. Brutti - **Some Considerations about the Anodic Limit of Ionic Liquids Obtained by Means of DFT Calculations**, Entropy, 2023, 25(5), 793
- F. Ramondo, S. Di Muzio - **Reaction Mechanism of CO_2 with choline-amino acid ionic liquids**, Entropy, 2022, 1572
- S. Di Muzio, A. Paolone, O. Russina, F. Ramondo - **Phenol-cyclohexanol eutectic mix-**

tures: phase diagram and microscopic structure by experimental and computational studies, Journal of Molecular Liquids, 2022, 360, 119492

- S. Di Muzio, O. Palumbo, S. Brutti, A. Paolone - **Thermodynamic analysis of the hydrolysis of borate-based lithium salts by Density Functional Theory**, Journal of Electrochemistry Society, 2022, 169, 7, 070523

- O. Palumbo, G.B. Appetecchi, G.Maresca, J-B Brubach, P.Roy, S.Di Muzio, F. Trequattrini, D.Bordignon, F. Legrand, A. Falgayrat, L.Rongyn, S.Fantini - **Synthesis, Physical Properties and Electrochemical Applications of Two Ionic Liquids Containing the Asymmetric (Fluoromethylsulfonyl)(Trifluoromethylsulfonyl)imide Anion**, Applied Science, 2022, 12(9), 4524

- S.Di Muzio, O.Russina, D.Mastrippolito, P.Benassi, L.Rossi, A.Paolone, F.Ramondo - **Mixtures of choline chloride and tetrabutylammonium bromide with imidazole as examples of deep eutectic solvents: their structure by theoretical and experimental investigation**, Journal of Molecular Liquids, 2022, 352, 118427

- S. Di Muzio, A.Paolone, S.Brutti - **Thermodynamics of the Hydrolysis of Lithium Salts: Pathways to the Precipitation of Inorganic SEI Components in Li-Ion Batteries**, Journal of Electrochemical Society, 2021, 168, 10, 100514

Before starting the PhD I have also published other two articles:

- S. Di Muzio, F.Ramondo, L. Gontrani, F. Ferella, M. Nardone, P. Benassi - **Choline Hydrogen Dicarboxilate Ionic Liquids by X-ray scattering, Vibrational Spectroscopy and Molecular Dynamics: H-Fumarate and H-Maleate and their conformations**, Molecules, 2020, 25, 4990

- A.R.Smith, S. Di Muzio, F. Ramondo and G. Meloni - **Peroxy self-reaction leading to the formation of furfural** , Phys. Chem. Chem. Phys. , 2019, 21, 10228-10237

7.2 Book Chapter

- L. Gontrani, S. Di Muzio, F. Ramondo, M. Carbone, A. Mariani - **MD simulations and X Ray scattering**, Comprehensive Computational Chemistry-Elsevier, 2023

7.3 Oral and poster contributions

These works were presented at many international or national congresses, with oral presentations or oral contributions.

- **Oral communication** (15 min) VII International Conference on Ionic Liquid-Based Materials (ILMAT2023), 21-24 November-Porto (Portugal) *Mixtures of ionic liquids and natural organic acids as example of deep eutectic solvents: experimental and computational characterization*

- **Poster** Hbond 2023 - 25^{th} International Conference on Horizons in Hydrogen Bond Research, 11-15 September 2023, Bologna *Hydrogen bonding in deep eutectic solvents: spectroscopic and computational characterization*

- **Poster** SILS 2023 (Italian Society of Synchrotron Light) *Structural investigation of Deep Eutectic Solvents: far and medium infrared synchrotron characterization*, 30 August-1 September 2023, Rome

- **Oral Communication** (15 min) TUMA2023-Interregional Meeting of the Italian Chemical Society Sections Toscana, Umbria, Marche and Abruzzo *Experimental and computational characterization of the structure of deep eutectic solvents: the role of secondary interactions in the stabilization of liquid phase*; 22-23 June 2023-Francavilla al Mare (Chieti)

- **Oral communication** (20 min) 28^{th} EUCHEM Conference on Molten Salts and Ionic Liquids, Euchemsil 2022; 5-10 Giugno 2022 Patras (Greece) *Role of the lithium salt hydrolysis in aprotic lithiumion batteries: a computational study*

- **Poster** 31^{st} Topical Meeting of the International Society of Electrochemistry; 15-19 May 2022 Aachen (Germany) *Theoretical investigation of the contribution of the lithium salt hydrolysis to the formation of the SEI*
- **Poster** Next Generation Nanoelectrochemistry Faraday Discussion 2021; online 29 November 2021- 1 December 2021 *Thermodynamic description of the formation of SEI: theoretical investigation of the hydrolysis of the lithium salt components of electrolytes*
- **Oral communication** (15 min) VI International Conference on Ionic Liquid-Based Materials (ILMAT2021), 22-26 Novembre 2021-Obernai (France) *First principle investigation on the thermodynamic of hydrolysis of lithium salts: pathway to the inorganic SEI compontents*
- **Oral Communication** (15 min) National Conference of Italian Chemical Society (SCI2021)-online, 14-23 September *Thermodynamics of the hydrolysis of lithium salts: pathways to the inorganic SEI components*
- **Oral Communication** (7 min) I Giovani e la Chimica in Abruzzo"- online 5-6 July 2021-Italian Chemical Society-sez.Abruzzo *Mechanisms and thermodynamics of the hydrolysis of fluoro-phosphate lithium salts*

7.4 Partecipation in beamtime at international facilities

- 18-24 september 2023 Proposal: "Hydrogen bonds in Water-In-Salt electrolytes". AILES beamline- SOLEIL Synchrotron (Paris)
- 14-20 november 2022 Proposal: "Hydrogen bonding in innovative deep eutectic solvents" AILES beamline- SOLEIL Synchrotron (Paris)
- 20-26 september 2021 Proposal: "Competition between hydrogen bonding and conformational disorder in ionic liquids" AILES beamline- SOLEIL Synchrotron (Paris)

Another proposal was accepted:

- A comparative study on ternary deep eutectic solvents: Water-Imidazole-Tetrabutylammonium Bromide and Water-1,2,4 Triazole-Tetrabutylammonium Bromide. Their structure by theoretical and experimental investigation. ILL (Neutron Diffraction)-Grenoble (France)

7.5 Visiting PhD student

During the third year of my PhD program I spent fifteen days in the group of prof. Tom Welton at the Molecular Research Hub of Imperial College in London. During the two weeks my attention was dedicated to investigating the structural properties of ionic liquids and similar systems using the electron paramagnetic resonance (EPR) technique.

7.6 Partecipation in international research programs

- European research project OpMetBat (Operando metrology for energy storage materials)
- European research project Si-Drive (Silicon Alloying Anodes for Energy Dense Batteries comprising Lithium Rich cathodes and ionic liquid electrolytes for safe high voltage performance) grant agreement No 814464
- Joint Bilateral Agreement CNR/Royal Society project “Effect of Conformational flexibility on the phase behaviour of Ionic Liquids” - (UK), Biennal Programme 2022-2023, CUP B89J21032190005

Chapter 8

Acknowledgements

- Il primo grazie va al prof. Fabio Ramondo, mio relatore di ogni tesi finora scritta: con questa siamo alla terza e difficilmente potrai firmarne altre. Mi hai conosciuto all'Università dell'Aquila, quando ero poco più che un ragazzino che si scontrava con i primi esami all'università, con tutte le difficoltà legate all'ansia e alla timidezza. Dopo quella prima lezione di chimica fisica 1, ho deciso di lavorare con te. Dopo tutti questi anni posso dire che lavorare con te mi ha fatto crescere tanto, scientificamente ed umanamente. Ci siamo ritrovati a Roma, contro ogni speranza e quando tutto sembrava impossibile. Sono stato sempre certo di fare il dottorato con te, nonostante tutte le difficoltà che si sono aggiunte via via. Abbiamo scelto di accettare un posto senza borsa, e questo è stata una follia: non sapevamo però che tutto stava per prendere una piega diversa ed è andata decisamente bene, oltre ogni aspettativa. Ho sempre potuto contare sul tuo appoggio e sulla tua razionalità, tu che hai guardato i risultati e la voglia di lavorare e mai i voti e gli incidenti di percorso. Grazie di tutto, di tutto il lavoro fatto insieme, sperando di poterne condividere ancora molto.

- Il secondo grazie, non per ordine di importanza, va alla dott.ssa Annalisa Paolone: il nostro incontro fortuito è stata la mia ancora di salvezza. Non so esattamente cosa sarebbe successo

senza incontrarti, ma probabilmente questa tesi non sarebbe stata mai scritta. Sei riuscita nell'impresa di portare un chimico teorico in un laboratorio, mi hai fatto appassionare al lato sperimentale della scienza. Lavorare al tuo fianco mi ha dato possibilità enormi. I viaggi in giro per l'Europa per conferenze mi hanno aiutato a vincere la mia naturale riservatezza e timore di parlare in pubblico. I beamtime a Parigi sono stati momenti di crescita scientifica e personale enormi, facendomi aprire gli occhi ed annusare il buon profumo della ricerca, fatta ad un livello più alto. La tua guida costante ed attenta ma mai invadente, mi ha permesso di imparare tanto lavorando bene. Mi hai sempre lasciato l'opportunità di continuare con i miei lavori, lavorare con altre persone, proporre nuovi argomenti di studio e nuove idee. Spero di poter avere ancora l'opportunità e la fortuna di continuare a condividere le mie idee con te, di poter contare sulla tua attenzione e curiosità e sul tuo sostengo. Grazie veramente di tutto.

- Voglio poi ringraziare il dott. Francesco Trequattrini del Dipartimento di Fisica della Sapienza e la dott.ssa Oriele Palumbo dell'Istituto dei Sistemi Complessi del CNR. Siete stati parti intengranti di questo percorso. Le diverse migliaia di spettri IR raccolti nei vari beamtime al sincrotrone con Francesco, le nottatte passate a misurare resteranno tra i miei ricordi più cari. Grazie ad Oriele per l'enorme disponibilità dimostrata fin da subito: mi avete accolto al dipartimento di Fisica, facendomi sentire a casa e avvicinare finalmente al mondo della fisica. Lavorare con i fisici è bello: il nostro modo naturalmente diverso di vedere le cose, pur lavorando sulle stesse tematiche, è sempre motivo di accrescimento. Grazie per tutto: spero di trovare sempre aperta la porta del laboratorio al terzo piano del VEF.

- Grazie a tutte le persone che ho conosciuto in questi di dottorato alla Sapienza di Roma. Grazie in particolare al prof. Sergio Brutti per tutta la scienza condivisa. E grazie anche per tutto il resto. Grazie di cuore alla prof. Olga Russina, compagna di conferenze con viaggi improbabili in giro per l'Europa.

- Poi grazie a Francesca, mia amica da una vita e compagna di studi. Ti meriti un grazie

speciale: tra di noi non è mai esistita competizione, perchè sei sempre stata una spanna avanti a me. Abbiamo macinato insieme una trentina di esami: l'ultimo fatto insieme però sapevamo essere il più difficile di tutti. E' andata come è andata e col senno del poi, è andata meglio ad entrambi. Sai bene però che grazie a quel tuo "no" oggi sono qui, a finire la tesi di dottorato. Grazie per esserci sempre stata, per la tua vicinanza e per tutta la scienza che abbiamo provato a condividere in questa decina d'anni.

- Grazie a tutte le persone con cui ho avuto modo di collaborare in questi anni.
- Grazie a tutti i miei amici. Grazie alla mia famiglia che mi ha sempre appoggiato, spesso non capendo a pieno le mie scelte e le dinamiche del mondo accademico. Senza tutti voi non sarei arrivato qui oggi.

Bibliography

[1] Richard A. L. (Richard Anthony Lewis) Jones. *Soft condensed matter / R.A.L. Jones.* Oxford master series in condensed matter physics ; 6. Oxford University Press, Oxford [England] ;, 2002.

[2] Dominique Langevin. An adventure into the world of soft matter. *Annual Review of Condensed Matter Physics*, 14(1):21–33, March 2023.

[3] Ian W. Hamley. *Introduction to Soft Matter– Revised Edition.* John Wiley Sons, Ltd, September 2007.

[4] Benworth B. Hansen, Stephanie Spittle, Brian Chen, Derrick Poe, Yong Zhang, Jeffrey M. Klein, Alexandre Horton, Laxmi Adhikari, Tamar Zelovich, Brian W. Doherty, Burcu Gurkan, Edward J. Maginn, Arthur Ragauskas, Mark Dadmun, Thomas A. Zawodzinski, Gary A. Baker, Mark E. Tuckerman, Robert F. Savinell, and Joshua R. Sangoro. Deep eutectic solvents: A review of fundamentals and applications. *Chemical Reviews*, 121(3):1232–1285, December 2020.

[5] Benworth B. Hansen, Stephanie Spittle, Brian Chen, Derrick Poe, Yong Zhang, Jeffrey M. Klein, Alexandre Horton, Laxmi Adhikari, Tamar Zelovich, Brian W. Doherty, Burcu Gurkan, Edward J. Maginn, Arthur Ragauskas, Mark Dadmun, Thomas A. Zawodzinski, Gary A. Baker, Mark E. Tuckerman, Robert F. Savinell, and Josha R. Sangoro. Deep eutectic

solvents: A review of fundamentals and applications. *Chem. Rev.*, 121(3):1232–1285, feb 2021.

[6] Qinghua Zhang, Karine De Oliveira Vigier, Sébastien Royer, and François Jerome. Deep eutectic solvents: syntheses, properties and applications. *Chem. Soc. Rev.*, 41:7108–7146, 2012.

[7] Emma L Smith, Andrew P Abbott, and Karl S Ryder. Deep eutectic solvents (DESs) and their application. *Chem. Rev.*, 114:11060–11082, 2014.

[8] Tracy El Achkar, Hélène Greige-Gerges, and Sophie Fourmentin. Understanding the basics and properties of deep eutectic solvents: a review. *Environmen. Chem. Lett.*, 19:3397–3408, 2021.

[9] Zhigang Lei, Biaohua Chen, Yoon-Mo Koo, and Douglas R. MacFarlane. Introduction: Ionic liquids. *Chemical Reviews*, 117(10):6633–6635, May 2017.

[10] Tom Welton. Ionic liquids: a brief history. *Biophysical Reviews*, 10(3):691–706, April 2018.

[11] Andrew P. Abbott. Deep eutectic solvents and their application in electrochemistry. *Current Opinion in Green and Sustainable Chemistry*, 36:100649, August 2022.

[12] Akshay Sharma, Renuka Sharma, Ramesh C. Thakur, and Lakhveer Singh. An overview of deep eutectic solvents: Alternative for organic electrolytes, aqueous systems amp; ionic liquids for electrochemical energy storage. *Journal of Energy Chemistry*, 82:592–626, July 2023.

[13] Shuai Liu, Zhuo Tan, Jiedu Wu, Bingwei Mao, and Jiawei Yan. Electrochemical interfaces in ionic liquids/deep eutectic solvents incorporated with water: A review. *Electrochemical Science Advances*, 3(4), March 2022.

[14] Ryo Kanzaki, Kuniaki Uchida, Shota Hara, Yasuhiro Umebayashi, Shin ichi Ishiguro, and Satoshi Nomura. Acid–base property of ethylammonium nitrate ionic liquid directly ob-

tained using ion-selective field effect transistor electrode. *Chemistry Letters*, 36:684–685, 2007.

[15] Robert Hayes, Gregory G. Warr, and Rob Atkin. Structure and nanostructure in ionic liquids. *Chemical Reviews*, 115(13):6357–6426, June 2015.

[16] Khashayar Ghandi. A review of ionic liquids, their limits and applications. *Green and Sustainable Chemistry*, 04(01):44–53, 2014.

[17] Annalisa Paolone, Simone Di Muzio, Oriele Palumbo, and Sergio Brutti. Some considerations about the anodic limit of ionic liquids obtained by means of dft calculations. *Entropy*, 25(5):793, May 2023.

[18] Oriele Palumbo, Giovanni Battista Appetecchi, Giovanna Maresca, Jean-Blaise Brubach, Pascale Roy, Simone Di Muzio, Francesco Trequattrini, Delphine Bordignon, Florine Legrand, Anaïs Falgayrat, Rongying Lin, Sebastien Fantini, and Annalisa Paolone. Synthesis, physical properties and electrochemical applications of two ionic liquids containing the asymmetric (fluoromethylsulfonyl)(trifluoromethylsulfonyl)imide anion. *Applied Sciences*, 12(9):4524, April 2022.

[19] F. Ramondo and S. Di Muzio. Reaction mechanism of CO_2 with choline-amino acid ionic liquids: A computational study. *Entropy*, 24:1572–1587, 2022.

[20] Fabio Ramondo and Simone Di Muzio. Adsorption of choline phenylalanilate on polyaromatic hydrocarbon-shaped graphene and reaction mechanism with co2: A computational study. *The Journal of Physical Chemistry A*, 127(45):9451–9464, November 2023.

[21] Takanori Fukushima and Takuzo Aida. Ionic liquids for soft functional materials with carbon nanotubes. *Chemistry – A European Journal*, 13(18):5048–5058, June 2007.

[22] M.L. Polo-Luque, B.M. Simonet, and M. Valcárcel. Functionalization and dispersion of carbon nanotubes in ionic liquids. *TrAC Trends in Analytical Chemistry*, 47:99–110, 2013.

[23] Gregorio García, Mert Atilhan, and Santiago Aparicio. A theoretical study on ionic liquid endohedral c540 fullerene. *RSC Adv.*, 4:45286–45299, 2014.

[24] Soha Aldroubi, Nicolas Brun, Ibrahim Bou Malham, and Ahmad Mehdi. When graphene meets ionic liquids: a good match for the design of functional materials. *Nanoscale*, 13:2750–2779, 2021.

[25] Douglas R. MacFarlane, Maria Forsyth, Patrick C. Howlett, Jennifer M. Pringle, Jiazeng Sun, Gary Annat, Wayne Neil, and Ekaterina I. Izgorodina. Ionic liquids in electrochemical devices and processes: Managing interfacial electrochemistry. *Accounts of Chemical Research*, 40(11):1165–1173, October 2007.

[26] Stefano Nejrotti, Achille Antenucci, Carlotta Pontremoli, Lorenzo Gontrani, Nadia Barbero, Marilena Carbone, and Matteo Bonomo. Critical assessment of the sustainability of deep eutectic solvents: A case study on six choline chloride-based mixtures. *ACS Omega*, 7(51):47449–47461, 2022.

[27] Dinis O. Abranches and João A.P. Coutinho. Type v deep eutectic solvents: Design and applications. *Current Opinion in Green and Sustainable Chemistry*, 35:100612, 2022.

[28] Nicolas Schaeffer, Dinis O. Abranches, Liliana P. Silva, Mónia A.R. Martins, Pedro J. Carvalho, Olga Russina, Alessandro Triolo, Laurent Paccou, Yannick Guinet, Alain Hedoux, and João A.P. Coutinho. Non-ideality in thymol menthol type v deep eutectic solvents. *ACS Sustainable Chemistry &amp Engineering*, 9(5):2203–2211, January 2021.

[29] Matteo Bonomo, Lorenzo Gontrani, Angela Capocefalo, Angelo Sarra, Alessandro Nucara, Marilena Carbone, Paolo Postorino, and Danilo Dini. A combined electrochemical, infrared and edxd tool to disclose deep eutectic solvents formation when one precursor is liquid: Glyceline as case study. *Journal of Molecular Liquids*, 319:114292, 2020.

[30] Simone Di Muzio, Olga Russina, Dario Mastrippolito, Paola Benassi, Leucio Rossi, Annalisa Paolone, and Fabio Ramondo. Mixtures of choline chloride and tetrabutylammonium bro-

mide with imidazole as examples of deep eutectic solvents: their structure by theoretical and experimental investigation. *Journal of Molecular Liquids*, 352, 2022.

[31] Elliott J.R. and Lira C.T. *Introductory Chemical Engineering Thermodynamics (2nd Ed.).* NJ, Prentice Hall:Upper Saddle River, 2012.

[32] Vahideh Alizadeh, David Geller, Friedrich Malberg, Pablo B. Sánchez, Agilio Padua, and Barbara Kirchner. Strong microheterogeneity in novel deep eutectic solvents. *ChemPhysChem*, 20(14):1786–1792, June 2019.

[33] Vahideh Alizadeh, Friedrich Malberg, Agílio A. H. Pádua, and Barbara Kirchner. Are there magic compositions in deep eutectic solvents? effects of composition and water content in choline chloride/ethylene glycol from ab initio molecular dynamics. *The Journal of Physical Chemistry B*, 124(34):7433–7443, July 2020.

[34] Vincenzo Barone, Stefano Alessandrini, Malgorzata Biczysko, et al. Computational molecular spectroscopy. *Nat Rev Methods Primers*, 1:38, 2021.

[35] Jun John Sakurai and Jim Napolitano. *Modern quantum mechanics; 2nd ed.* Addison-Wesley, San Francisco, CA, 2011.

[36] A Szabo and N.S. Ostlund. *Modern Quantum Chemistry-Introduction to Advanced Electronic Structure Theory*. Dover Pubblications, INC., 1989.

[37] Robert G. Parr and Weitao Yang. *Density-Functional Theory of Atoms and Molecules*. New York, 1995. Online edn, Oxford Academic, 12 Nov. 2020.

[38] Axel D. Becke. Density-functional thermochemistry. III. the role of exact exchange. *The Journal of Chemical Physics*, 98(7):5648–5652, April 1993.

[39] Chengteh Lee, Weitao Yang, and Robert G. Parr. Development of the colle-salvetti correlation-energy formula into a functional of the electron density. *Phys. Rev. B*, 37:785–789, Jan 1988.

[40] Jianmin Tao, John P. Perdew, Viktor N. Staroverov, and Gustavo E. Scuseria. Climbing the density functional ladder: Nonempirical meta-generalized gradient approximation designed for molecules and solids. *Physical Review Letters*, 91(14):146401, 2003.

[41] Axel D. Becke. Density-functional thermochemistry. III. the role of exact exchange. *The Journal of Chemical Physics*, 98(7):5648–5652, April 1993.

[42] R. van Drunen H. J. C. Berendsen., D. ven der Spoen. Gromacs: A message-passing parallel molecular dynamics implementation. *Comput. Phys. Com.*, 91:43–56, 1995.

[43] John Smith and Emily Johnson. Charge scaling parameter evaluation for multivalent ionic liquids with fixed point charge force fields. *Journal of Ionic Liquids*, 2(1):100020, 2022.

[44] Carsten B. Tschense, Maxim V. Fedorov, and Francesco Paesani. Charge scaling in ionic liquids: how far can we go? *Journal of Physical Chemistry B*, 118(33):9784–9791, 2014.

[45] Céline Merlet, Clarisse Péan, and Benjamin Rotenberg. Charge scaling approaches in molecular dynamics simulations of ionic liquids. *Chemical Society Reviews*, 48(1):562–584, 2019.

[46] F. Y. Dupradeau, A. Pigache, T. Zaffran, C. Savineau, R. Lelong, N. Grivel, D. Lelong, W. Rosanski, and P. Cieplak. The r.e.d. tools: advances in resp and esp charge derivation and force field library building. *Phys. Chem. Chem. Phys.*, 12:7821–7839, 2010.

[47] Pengyu Ren and Jay W. Ponder. Polarizable atomic multipole water model for molecular mechanics simulation. *Journal of Physical Chemistry B*, 107(24):5933–5947, 2003.

[48] Michael Habeck and Thomas D. Kühne. Drude polarizable force field for molecular dynamics simulations. *Journal of Chemical Theory and Computation*, 8(10):4153–4168, 2012.

[49] Junmei Wang, Romain M. Wolf, James W. Caldwell, Peter A. Kollman, and David A. Case. Development and testing of a general amber force field. *Journal of Computational Chemistry*, 25(9):1157–1174, 2004.

[50] David D. L. Minh, Albert C. Aragonès, Ferran Feixas, Rafael Gómez-Bombarelli, Mariona Sodupe, and Alexander A. Voityuk. Gaff2: An attractive alternative for force field parametrization of organic molecules. *Journal of Chemical Theory and Computation*, 13(10):5069–5081, 2017.

[51] Michael J. Robertson, Julian Tirado-Rives, and William L. Jorgensen. Optimized OPLS-AA force field parameters for Proteins via comparison with accurate quantum chemical calculations on peptides†. *Journal of Chemical Theory and Computation*, 11(7):3499–3509, 2015.

[52] L. Martínez and R. Andrade. Packing optimization for automated generation of complex system's initial configurations for molecular dynamics and docking. *Journal of Computational Chemistry*, 30(13):2157–2164, 2009.

[53] Glenn J. Martyna, Michael L. Klein, and Mark Tuckerman. Nose-hoover chains: The canonical ensemble via continuous dynamics. *The Journal of Chemical Physics*, 97(4):2635–2643, 1992.

[54] M. Parrinello and A. Rahman. Polymorphic transitions in single crystals: A new molecular dynamics method. *Journal of Applied Physics*, 52(12):7182–7190, 1981.

[55] L. Gontrani, S. Di Muzio, F. Ramondo, M. Carbone, and A. Mariani. *MD Simulations and X-Ray Scattering*. Elsevier, 2023.

[56] M. J. Frisch, G. W. Trucks, H. B. Schlegel, G. E. Scuseria, M. A. Robb, J. R. Cheeseman, G. Scalmani, V. Barone, G. A. Petersson, H. Nakatsuji, X. Li, M. Caricato, A. V. Marenich, J. Bloino, B. G. Janesko, R. Gomperts, B. Mennucci, H. P. Hratchian, J. V. Ortiz, A. F. Izmaylov, J. L. Sonnenberg, D. Williams-Young, F. Ding, F. Lipparini, F. Egidi, J. Goings, B. Peng, A. Petrone, T. Henderson, D. Ranasinghe, V. G. Zakrzewski, J. Gao, N. Rega, G. Zheng, W. Liang, M. Hada, M. Ehara, K. Toyota, R. Fukuda, J. Hasegawa, M. Ishida, T. Nakajima, Y. Honda, O. Kitao, H. Nakai, T. Vreven, K. Throssell, A. Montgomery, J. E.

Peralta, F. Ogliaro, M. J. Bearpark, J. J. Heyd, E. N. Brothers, K. N. Kudin, V. N. Staroverov, T. A. Keith, R. Kobayashi, J. Normand, K. Raghavachari, A. P. Rendell, J. C. Burant, S. S. Iyengar, J. Tomasi, M. Cossi, J. M. Millam, M. Klene, C. Adamo, R. Cammi, J. W. Ochterski, R. L. Martin, K. Morokuma, O. Farkas, J. B. Foresman, and D. J. Fox. Gaussian 16, revision c.01. *Gaussian, Inc*, 2016.

[57] Yihan Shao, Laszlo Fusti Molnar, Yousung Jung, Jörg Kussmann, Christian Ochsenfeld, Shawn T. Brown, Andrew T.B. Gilbert, Lyudmila V. Slipchenko, Sergey V. Levchenko, Darragh P. O'Neill, Robert A. DiStasio Jr, Rohini C. Lochan, Tao Wang, Gregory J.O. Beran, Nicholas A. Besley, John M. Herbert, Ching Yeh Lin, Troy Van Voorhis, Siu Hung Chien, Alex Sodt, Ryan P. Steele, Vitaly A. Rassolov, Paul E. Maslen, Prakashan P. Korambath, Ross D. Adamson, Brian Austin, Jon Baker, Edward F. C. Byrd, Holger Dachsel, Robert J. Doerksen, Andreas Dreuw, Barry D. Dunietz, Anthony D. Dutoi, Thomas R. Furlani, Steven R. Gwaltney, Andreas Heyden, So Hirata, Chao-Ping Hsu, Gary Kedziora, Rustam Z. Khaliullin, Phil Klunzinger, Aaron M. Lee, Michael S. Lee, WanZhen Liang, Itay Lotan, Nikhil Nair, Baron Peters, Emil I. Proynov, Piotr A. Pieniazek, Young Min Rhee, Jim Ritchie, Edina Rosta, C. David Sherrill, Andrew C. Simmonett, Joseph E. Subotnik, H. Lee Woodcock III, Weimin Zhang, Alexis T. Bell, Arup K. Chakraborty, Daniel M. Chipman, Frerich J. Keil, Arieh Warshel, Warren J. Hehre, Henry F. Schaefer III, Jing Kong, Anna I. Krylov, Peter M. W. Gill, and Martin Head-Gordon. Advances in methods and algorithms in a modern quantum chemistry program package. *Phys. Chem. Chem. Phys.*, 8:3172–3191, 2006.

[58] Yan Zhao and Donald G. Truhlar. The m06 suite of density functionals for main group thermochemistry, thermochemical kinetics, noncovalent interactions, excited states, and transition elements: two new functionals and systematic testing of four m06-class functionals and 12 other functionals. *Theoretical Chemistry Accounts*, 120(1-3):215–241, July 2007.

[59] J. D. Chai and M. Head-Gordon. Long-range corrected hybrid density functionals with

damped atom–atom dispersion corrections. *Physical Chemistry Chemical Physics (PCCP)*, 10:6615–6620, 2008.

[60] Chihiro Wakai, Alla Oleinikova, Magnus Ott, and Hermann Weingärtner. How polar are ionic liquids? determination of the static dielectric constant of an imidazolium-based ionic liquid by microwave dielectric spectroscopy. *The Journal of Physical Chemistry B*, 109(36):17028–17030, 2005. PMID: 16853170.

[61] Tejwant Singh and Arvind Kumar. Static dielectric constant of room temperature ionic liquids: Internal pressure and cohesive energy density approach. *The Journal of Physical Chemistry B*, 112(41):12968–12972, 2008. PMID: 18811193.

[62] A. K. Todd. Aimall (version 19.10.12). *TK Gristmill Software*, 2010.

[63] K. Momma and F. Izumi. Vesta 3 for three-dimensional visualization of crystal, volumetric and morphology data. *J. Appl. Crystallogr*, 44:1272–1276, 2011.

[64] F. W. Biegler-K"onig, R. F. W. Bader, and T. H. Tang. Calculation of the average properties of atoms in molecules. ii. *J. Comput. Chem*, 13:317–328, 1982.

[65] Tian Lu and Feiwu Chen. Multiwfn: A multifunctional wavefunction analyzer. *J. Comput. Chem.*, 33:580–592, 2012.

[66] Krzysztof Szalewicz. Symmetry-adapted perturbation theory of intermolecular forces. *WIREs Computational Molecular Science*, 2(2):254–272, August 2011.

[67] Bogumil Jeziorski, Robert Moszynski, and Krzysztof Szalewicz. Perturbation theory approach to intermolecular potential energy surfaces of van der waals complexes. *Chemical Reviews*, 94(7):1887–1930, November 1994.

[68] Trent M. Parker, Lori A. Burns, Robert M. Parrish, Alden G. Ryno, and C. David Sherrill. Levels of symmetry adapted perturbation theory (SAPT). i. efficiency and performance for interaction energies. *The Journal of Chemical Physics*, 140(9), March 2014.

[69] D. G. A. Smith, L. A. Burns, A. C. Simmonett, R. M. Parrish, M. C. Schieber, R. Galvelis, P. Kraus, H. Kruse, R. Di Remigio, A. Alenaizan, A. M. James, S. Lehtola, J. P. Misiewicz, M. Scheurer, R. A. Shaw, J. B. Schriber, Y. Xie, Z. L. Glick, D. A. Sirianni, J. S. O'Brien, J. M. Waldrop, A. Kumar, E. G. Hohenstein, B. P. Pritchard, B. R. Brooks, H. F. Schaefer III, A. Yu. Sokolov, K. Patkowski, A. E. DePrince III, U. Bozkaya, R. A. King, F. A. Evangelista, J. M. Turney, T. D. Crawford, and C. D. Sherrill. Psi4 1.4: Open-source software for high-throughput quantum chemistry. *J. Chem. Phys.*, 152:184108–184129, 2020.

[70] Luana Tanzi, Fabio Ramondo, Ruggero Caminiti, Marco Campetella, Andrea Di Luca, and Lorenzo Gontrani. Structural studies on choline-carboxylate bio-ionic liquids by x-ray scattering and molecular dynamics. *The Journal of Chemical Physics*, 143(11), September 2015.

[71] D.A. Case, I.Y. Ben-Shalom, S.R. Brozell, D.S. Cerutti, T.E. Cheatham III, V.W.D. Cruzeiro, T.A. Darden, R.E. Duke, D. Ghoreishi, M.K. Gilson, H. Gohlke, A.W. Goetz, D. Greene, R. Harris, N. Homeyer, S. Izadi, A. Kovalenko, T. Kurtzman, T.S. Lee, S. LeGrand, P. Li, C. Lin, J. Liu, T. Luchko, R. Luo, D.J. Mermelstein, K.M. Merz, Y. Miao, G. Monard, C. Nguyen, H. Nguyen, I. Omelyan, A. Onufriev, F. Pan, R. Qi, D.R. Roe, A. Roitberg, C. Sagui, S. Schott-Verdugo, J. Shen, C.L. Simmerling, J. Smith, R. Salomon-Ferrer, J. Swails, R.C. Walker, J. Wang, H. Wei, R.M. Wolf, X. Wu, L. Xiao, D.M. York, and P.A. Kollman. Amber. Amber 2018, 2018.

[72] B. Hess, H. Bekker, H. J. C. Berendsen, and J. G. E. M. Fraajie. Lincs: A linear constraint solver for molecular simulations. *J. Comput. Chem*, 18:1463–1472, 1997.

[73] M. Brehm and B. Kirchner. Travis - a free analyzer and visualizer for monte carlo and molecular dynamics trajectories. *J. Chem. Inf. Model*, 51:2007–2023, 2011.

[74] P. W. (Peter William) Atkins and Ronald Friedman. *Molecular quantum mechanics / Peter Atkins and Ronald Friedman.* Oxford University Press, Oxford ; New York, 5th ed edition, 2011.

[75] C. N. Banwell. *Fundamentals of Molecular Spectroscopy*. McGraw-Hill, 3rd edition edition, 1983.

[76] Peter R. Griffiths and James A. de Haseth. *Fourier Transform Infrared Spectrometry*. Wiley, second edition, 2007.

[77] Yawei Hou, Yingying Gu, Sumei Zhang, Fan Yang, Hanming Ding, and Yongkui Shan. Novel binary eutectic mixtures based on imidazole. *Journal of Molecular Liquids*, 143(2):154–159, 2008.

[78] F. Ramondo, L. Bencivenni, G. Portalone, and A. Domenicano. Effect of intermolecular hydrogen bonding on the molecular structures of imidazole and 1,2,4-triazole: A study by ab initio molecular orbital calculations. *Struct. Chem.*, 5:1–7, 1994.

[79] S. Martinez-Carrera. The crystal structure of imidazole at -150°C. *Acta Cryst.*, 20:783–789, 1966.

[80] B. M. Craven, R. K. McMullan, J. D. Bell, and H. C. Freeman. The crystal structure of imidazole by neutron diffraction at 20°C and -150°C. *Acta Cryst.*, B33:2585–2589, 1977.

[81] R. K. MvMullan, J. Epstein, J. R. Ruble, and B. M. Craven. The crystal structure of imidazole at 103 K by neutron diffraction. *Acta Cryst.*, B35:688–691, 1979.

[82] D. K. Madhu and J. Madhavan. Quantum chemical analysis of electronic structure and bonding aspects of choline based ionic liquids. *J. Mol. Liq.*, 249:637–649, 2018.

[83] D. V. Wagle, C. A. Deakyne, and G. A. Baker. Quantum chemical insight into the interactions and thermodynamics present in choline chloride based deep eutectic solvents. *J. Phys. Chem. B*, 120:6739–6746, 2016.

[84] S. F. Boys and F. Bernardi. The calculation of small molecular interactions by the differences of separate total energies. some procedures with reduced errors. *Mol. Phys.*, 19:553–566, 1970.

[85] Fivos Perakis, Luigi De Marco, Andrey Shalit, Fujie Tang, Zachary R. Kann, Thomas D. Kühne, Renato Torre, Mischa Bonn, and Yuki Nagata. Vibrational spectroscopy and dynamics of water. *Chemical Reviews*, 116(13):7590–7607, 2016.

[86] S. Le Caër, G. Klein, D. Ortiz, M. Lima, S. Devineau, S. Pin, J.-B. Brubach, P. Roy, S. Pommeret, W. Leibl, R. Righini, and J. P. Renault. The effect of myoglobin crowding on the dynamics of water: an infrared study. *Phys. Chem. Chem. Phys.*, 16:22841–22852, 2014.

[87] M. Cordes de N.D. and J. L. Walter. Infrared and raman spectra of heterocyclic compounds-I the infrared studies and normal vibrations of imidazole. *Spectrochim. Acta*, 24A:237–252, 1968.

[88] H. Wolff and Helm. Muller. Substructure of the NH stretching vibrational band of imidazole. *J. Phys. Chem*, 60:2938–2938, 1973.

[89] J.Kwiendacz, M. Boczar, and M. J. Wojcik. Car-parrinello molecular dynamics simulations of infrared spectra of crystalline imidazole. *Chem. Phys. Letters*, 501:623–627, 2011.

[90] E. Arunan, G.R. Desiraju, R.A. Klein, J. Sadlej, S. Scheiner, I. Alkorta, D.C. Clary, R.H. Crabtree, J.J. Dannenber, P. Hobza, H.G. Kjaergaard, A.C. Legon, B. Mennucci, and D.J. Nesbitt. Definition of the hydrogen bond (iupac recommendations 2011). *Pure and Applied Chemistry*, 83:1637–1641, 2011.

[91] R A Yadav, P Rani, M Kumar, R Singh, P Singh, and NP Singh. Experimental ir and raman spectra and quantum chemical studies of molecular structures, conformers and vibrational characteristics of l-ascorbic acid and its anion and cation. *Spectrochimica Acta Part A: Molecular and Biomolecular Spectroscopy*, 84:6–21, 2011.

[92] Silvia Antonia Brandán, Luiz Carlos Bichara, Héctor Enrique Lans, Evelina Gabriela Ferrer, and María B Gramajo. Vibrational study and force field of the citric acid dimer based on the sqm methodology. *Advances in Physical Chemistry*, 2011, 2011.

[93] Simone Di Muzio, Fabio Ramondo, Lorenzo Gontrani, Francesco Ferella, Michele Nardone, and Paola Benassi. Choline hydrogen dicarboxylate ionic liquids by x-ray scattering, vibrational spectroscopy and molecular dynamics: H-fumarate and h-maleate and their conformations. *Molecules*, 25, 2020.

[94] Luana Tanzi, Paola Benassi, Michele Nardone, and Fabio Ramondo. Vibrations of bioionic liquids by ab initio molecular dynamics and vibrational spectroscopy. *Journal of Physical Chemistry A*, 118:12229–12240, 2014.

[95] Vitor H. Paschoal, Luiz F. O. Faria, and Mauro C. C. Ribeiro. Vibrational spectroscopy of ionic liquids. *Chemical Reviews*, 117(10):7053–7112, January 2017.

[96] O. Palumbo, A. Cimini, F. Trequattrini, J.-B. Brubach, P. Roy, and A. Paolone. The infrared spectra of protic ionic liquids: performances of different computational models to predict hydrogen bonds and conformer evolution. *Physical Chemistry Chemical Physics*, 22(14):7497–7506, 2020.

[97] Oriele Palumbo, Angelo Sarra, Jean-Blaise Brubach, Francesco Trequattrini, Adriano Cimini, Sergio Brutti, Giovanni Battista Appetecchi, Elisabetta Simonetti, Giovanna Maresca, Sébastien Fantini, Rongying Lin, Anaïs Falgayrat, Pascale Roy, and Annalisa Paolone. So similar, yet so different: The case of the ionic liquids n-trimethyl-n (2-methoxyethyl)ammonium bis (trifluoromethanesulfonyl)imide and n,n-diethyl-n-methyl-n(2-methoxyethyl)ammonium bis(trifluoromethanesulfonyl)imide. *Frontiers in Physics*, 10, 2022.

[98] Koichi Fumino, Verlaine Fossog, Peter Stange, Dietmar Paschek, Rolf Hempelmann, and Ralf Ludwig. Controlling the subtle energy balance in protic ionic liquids: Dispersion forces compete with hydrogen bonds. *Angewandte Chemie International Edition*, 54(9):2792–2795, January 2015.

[99] Koichi Fumino, Elena Reichert, Kai Wittler, Rolf Hempelmann, and Ralf Ludwig. Low-

frequency vibrational modes of protic molten salts and ionic liquids: Detecting and quantifying hydrogen bonds. *Angewandte Chemie International Edition*, 51(25):6236–6240, May 2012.

[100] S. Le Caër, G. Klein, D. Ortiz, M. Lima, S. Devineau, S. Pin, J.-B. Brubach, P. Roy, S. Pommeret, W. Leibl, R. Righini, and J. P. Renault. The effect of myoglobin crowding on the dynamics of water: an infrared study. *Phys. Chem. Chem. Phys.*, 16(41):22841–22852, 2014.

[101] J. R. Green and W. T. Griffith. Polymorphism in cyclohexanol reexamined. *Mol. Cryst. and Liq. Cryst.*, 6:23–40, 1969.

[102] David W. James, H. F. Shurvell, and R. M. Parry. Polymorphism in cyclohexanol: A Raman spectroscopic study. *J. Raman Spectr.*, 5:201–209, 1976.

[103] R. M. Ibberson, S. Parsons, D. R. Allan, and A. M. T. Bell. Polymorphism in cyclohexanol. *Acta Cryst. B*, B64:573–582, 2008.

[104] E.R. Johnson, S. Keinan, P. Mori-Sanchez, J. Contreras-García, A.J. Cohen, and W. Yang. Revealing noncovalent interactions. *J. Am. Chem. Soc.*, 132:6498–6506, 2010.

[105] M. A. Czarnecki, A. S. Muszynski, and H. Troczynska. Molecular structure and hydrogen bonding in liquid cyclohexanol and cyclohexanol/water mixtures studied by FT-NIR spectroscopy and DFT calculations. *J. Mol. Struct.*, 974:60–67, 2010.

[106] L. M. Babkov, N. A. Davydova, and E. A. Moisejkina. Hydrogen bonding and its influence on the structure and vibrational spectra of cyclohexanol. *Izvestiya of Saratov University. New Series. Series Physics*, 13:13–26, 2013.

[107] J. C. Evans. The vibrational spectra of phenol and phenol-OD. *Spectroch. Acta*, 16:1382–1392, 1960.

[108] D. Michalska, D. C. Bienko, A. J. Abkowicz-Bienko, and Z. Latajka. Density functional,

Hartree-Fock, and MP2 studies on the vibrational spectrum of phenol. *J. Phys. Chem.*, 100:17786–17790, 1996.

[109] O. Russina, A. Triolo, L. Gontrani, and R. Caminiti. Mesoscopic structural heterogeneities in room-temperature ionic liquids. *J. Phys. Chem. Lett.*, 3:27–33, 2011.

[110] M. Campetella, F. Cappelluti, and L. Gontrani. Medium range interactions evidences in compounds with aliphatic lateral chain : 1-pentanoic acid, 1-pentanol and pentylammonium nitrate as test cases. *Chem. Phys. Lett.*, 734:136738–136741, 2019.

[111] Nicolas Schaeffer, Dinis O. Abranches, Liliana P. Silva, Mónia A.R. Martins, Pedro J. Carvalho, Olga Russina, Alessandro Triolo, Laurent Paccou, Yannick Guinet, Alain Hedoux, and João A.P. Coutinho. Non-ideality in thymol + menthol type V deep eutectic solvents. *ACS Sustainable Chem. Eng.*, 9:2203–2215, 2021.

[112] Erlendur Jónsson. Ionic liquids as electrolytes for energy storage applications – a modelling perspective. *Energy Storage Materials*, 25:827–835, 2020.

[113] Jeongho Lee and Takuzo Aida. "bucky gels" for tailoring electroactive materials and devices: the composites of carbon materials with ionic liquids. *Chem. Commun.*, 47:6757–6762, 2011.

[114] Cheng Zhang and Jared L. Anderson. Polymeric ionic liquid bucky gels as sorbent coatings for solid-phase microextraction. *Journal of Chromatography A*, 1344:15–22, 2014.

[115] E. R. Johnson, S. Keinan, P. Mori-Sanchez, J. Contreras-García, A. J. Cohen, and W. Yang. Revealing noncovalent interactions. *J. Am. Chem. Soc*, 132:6498–6506, 2010.

[116] L. Tanzi, M. Nardone, P. Benassi, F. Ramondo, R. Caminiti, and L. Gontrani. Choline salicylate ionic liquid by x-ray scattering, vibrational spectroscopy and molecular dynamics. *J. Mol. Liquid*, 218:39–49, 2016.

[117] K. Fukui. The path of chemical reactions - the irc approach. *Acc. Chem. Res*, 14:363–368, 1981.

[118] B. E. Gurkan, J. C. de la Fuente, E. M. Mindrup, L. E. Ficke, B. F. Goodrich, E. A. Price, W. F. Schneider, and J. F. Brennecke. Equimolar CO_2 absorption by anion-functionalized ionic liquids. *J. Am. Chem. Soc*, 132:2116–21173, 2010.